INFORMATION TO USERS

This material was produced from a microfilm copy of the original document. While the most advanced technological means to photograph and reproduce this document have been used, the quality is heavily dependent upon the quality of the original submitted.

The following explanation of techniques is provided to help you understand markings or patterns which may appear on this reproduction.

1. The sign or "target" for pages apparently lacking from the document photographed is "Missing Page(s)". If it was possible to obtain the missing page(s) or section, they are spliced into the film along with adjacent pages. This may have necessitated cutting thru an image and duplicating adjacent pages to insure you complete continuity.

2. When an image on the film is obliterated with a large round black mark, it is an indication that the photographer suspected that the copy may have moved during exposure and thus cause a blurred image. You will find a good image of the page in the adjacent frame.

3. When a map, drawing or chart, etc., was part of the material being photographed the photographer followed a definite method in "sectioning" the material. It is customary to begin photoing at the upper left hand corner of a large sheet and to continue photoing from left to right in equal sections with a small overlap. If necessary, sectioning is continued again — beginning below the first row and continuing on until complete.

4. The majority of users indicate that the textual content is of greatest value, however, a somewhat higher quality reproduction could be made from "photographs" if essential to the understanding of the dissertation. Silver prints of "photographs" may be ordered at additional charge by writing the Order Department, giving the catalog number, title, author and specific pages you wish reproduced.

5. PLEASE NOTE: Some pages may have indistinct print. Filmed as received.

University Microfilms International
300 North Zeeb Road
Ann Arbor, Michigan 48106 USA
St. John's Road, Tyler's Green
High Wycombe, Bucks, England HP10 8HR

INTERNAL BREMSSTRAHLUNG ACCOMPANYING K-CAPTURE, AND INTERNAL BREMSSTRAHLUNG ACCOMPANYING AUTOIONIZATION IN BETA DECAY, IN THE DECAY OF ^{204}Tl

by

ARNOLD ZIDE

A dissertation submitted to the Graduate Faculty in Physics in partial fulfillment of the requirements for the degree of Doctor of Philosophy, The City University of New York

1977

This manuscript has been read and accepted for the Graduate Faculty in Physics in satisfaction of the dissertation requirements for the degree of Doctor of Philosophy.

June 13, 1977
Date

Chairman of Examining Committee

June 15, 1977
Date

Executive Officer

Supervisory Committee

The City University of New York

ABSTRACT

INTERNAL BREMSSTRAHLUNG ACCOMPANYING K-CAPTURE, AND INTERNAL BREMSSTRAHLUNG ACCOMPANYING AUTO-IONIZATION IN BETA DECAY, IN THE DECAY OF ^{204}Tl

by

ARNOLD ZIDE

ADVISOR: PROFESSOR HENRYK LANCMAN

By measuring coincidences between bremsstrahlung photons and x-ray photons emitted during the filling of vacancies produced by the capture of K-shell electrons in ^{204}Tl, we have measured the partial 1s internal bremsstrahlung spectrum. A 3" by 3" naI(Tl) detector and a low energy, high-resolution Ge(Li) detector were used to obtain the coincidence spectra in a slow-fast coincidence system ($T_{\frac{1}{2}} = 13$ nsec). Data was acquired in a two-parameter analysis mode, and a biased amplifier was included in the Ge(Li) branch in order to define more accurately the distribution of pulses within the Hg K x-ray range. This allowed for better determination of the background in the coincidence spectra, and resulted in the identification of x rays in addition to the Hg K x rays in coincidence with the bremsstrahlung photons. These x rays are higher in energy and weaker in intensity than the mercury K x rays. Data obtained with beryllium, aluminum, and copper absorbers proved these x rays to be autoionization Pb K x rays accompanying internal bremsstrahlung photons in the beta decay of ^{204}Tl, an effect which has not been previously reported.

The experimental IB spectrum (accompanying K-capture) is compared to various theoretically predicted spectra with a chi-square fitting routine, which is used to predict the Q-value of the capture transition.

ACKNOWLEDGEMENTS

I would like to thank my thesis advisor, Dr. Henryk Lancman, for his help and guidance.

I am grateful to Dr. Louis Celenza and Dr. Robert Intemann for help on the theoretical aspects of the thesis.

I am especially indebted to my wife and family for their support and encouragement.

And finally, I thank Sue Drill for tying a difficult manuscript.

"The future belongs to those who prepare for it."

(Ralph Waldo Emerson)

INTERNAL BREMSSTRAHLUNG ACCOMPANYING K-CAPTURE, AND INTERNAL BREMSSTRAHLUNG ACCOMPANYING AUTOIONIZATION IN BETA DECAY, IN THE DECAY OF ^{204}Tl

TABLE OF CONTENTS

LIST OF TABLES

LIST OF FIGURES

I. INTRODUCTION

The purpose of this investigation was to measure the internal bremsstrahlung (IB) accompanying K-capture in ^{204}Tl, which is a first-forbidden unique transition, and compare it to a theory suitable for this degree of forbiddeness. Recently, Zon and Rapoport,[1,2] have developed a theory of IB in electron capture valid to any degree of forbiddeness, but a reliable test of this theory for first-forbidden unique decays has not been made.

It is of particular interest to measure the K-capture IB spectrum from ^{204}Tl, since a previous measurement[3] resulted in considerable disagreement between the experimental and theoretical intensity predicted by the Martin and Glauber theory,[4,5] which has generally been a successful treatment of the phenomenon[6-12] for allowed decays. Other measurements of the IB from this nuclide[6,13,14] have been made in order to determine the energy of the electron capture transition. These investigations did not yield the intensity of the IB spectrum, and assumed the Martin and Glauber theory in order to obtain the end-point energy of the spectrum. There have been indications that the results of these measurements have been unreliable.[15,16]

The Zon and Rapoport theory has been compared to experiments in a few cases for allowed transitions, and has been shown to give slightly better agreement with the experimental intensity than the Martin and Glauber theory.[2] In the one case where the theory has been compared to the first-forbidden unique transition in ^{41}Ca, the results are uncertain due

to experimental complications.

In order to obtain the IB data, a system was developed for taking coincidence measurements with a NaI(Tl) detector and a high resolution Ge(Li) spectrometer. The Ge(Li) detector allowed accurate analysis of the bremsstrahlung associated with the components of various x rays. The system apparatus was designed to maximize the coincidence counting rate to compensate for the low counting efficiency of the x-ray detector, and to minimize scattering between the two detectors. Data was stored in multichannel analyzers in 2-parameter analysis mode, which allowed measuring the number of coincident photons versus their energies.

In the course of measuring the IB spectrum, we have observed an effect which we have shown to be associated with the beta decay branch in ^{204}Tl, and which has previously been unreported. It is also to be noted that in the Lancman and Bond investigation of the 1s IB spectrum in ^{204}Tl, a large and unavoidable background due to the double internal bremsstrahlung (DIB) produced in the beta decay of ^{204}Tl contributed to the IB coincidence data. Although it was impossible to eliminate this contribution to the present experimental data, it has been possible to reduce this background and accurately account for it with the high resolution Ge(Li) spectrometer in the x-ray branch of the system. This detector was used with a biased amplifier in order to distribute the narrow band of pulses in the range of the mercury K x rays along 64 channels of the spectrum, which permitted

careful examination of the background in the region between the Hg K_{α} and Hg K_{β} x rays. The examination of this region revealed structures more complicated than the DIB alone could account for. A careful analysis proved these structures to be the autoionization Pb K x rays accompanying bremsstrahlung photons in the beta decay of ^{204}Tl.

A full discussion of this effect, in which internal bremsstrahlung is observed in autoionization, is included in the analysis, and presented in the discussion of the coincidence data (see Analysis of Coincidence Data--Part III 2.2).

REFERENCES --INTRODUCTION

1. B. A. Zon and L. P. Rapoport, Sov. J. Nucl. Phys. 7, 330 (1968).
2. B. A. Zon, Sov. J. Nucl. Phys. 13, 554 (1971).
3. H. Lancman and A. Bond, Phys. Rev. C7, 2600 (1973).
4. P. C. Martin and R. J. Glauber, Phys. Rev. 109, 1307 (1958).
5. R. J. Glauber and P. C. Martin, Phys. Rev. 104, 18 (1956).
6. M. H. Biavati, S. J. Nassif and C. S. Wu, Phys. Rev. 125, 1364 (1962).
7. T. Lindqvist and C. S. Wu, Phys. Rev. 100, 145 (1955).
8. R. W. Hayward and D. D. Hoppes, Phys. Rev. 104, 183 (1956).
9. J. L. Olsen, L. G. Mann and M. Linder, Phys. Rev. 106, 985 (1957).
10. H. Lancman and J. M. Lebowitz, Phys. Rev. 188, 1683, (1969).
11. H. Lancman and J. M. Lebowitz, Phys. Rev. C3, 188 (1971).
12. H. Lancman and J. M. Lebowitz, Phys. Rev. C3, 465 (1971).
13. E. der Mateosian and A. Smith, Phys. Rev. 88, 1186 (1962).
14. R. G. Jung and M. L. Pool, Bull Am. Phys. Soc. 1, 172, (1956).
15. W. McLatchie, et al., Can J. Phys. 42, 926 (1964).
16. P. F. A. Goudsmith, J. F. W. Jansen, B. J. Mijheer, and A. H. Wapstra, Physica (Utr.) 32, 2161 (1966).
17. B. Myslek, Z. Sukjowski and J. Zylicz, Nucl. Phys., A215, 79, (1973).

II. THEORY OF IB ACCOMPANYING K-CAPTURE

Radiative orbital electron capture is a process in which continuous in energy electromagnetic radiation accompanies the capture of an orbital electron by the nucleus. This radiation, called internal bremsstrahlung, is of low intensity and is therefore masked usually by the discrete gamma rays of nuclear and (or) atomic origin associated with the capture process. In ^{204}Tl, for example, the IB is obscured by the electron capture x rays, and by the internal and external bremsstrahlung accompanying the beta decay.

Morrison and Schiff determined the spectral distribution and total intensity of IB photons for allowed nuclear transitions. Their calculations were based on the highly simplified assumptions that nuclear coulomb effects may be neglected and that capture occurs only from the K shell. They obtained the expression

$$\frac{W_{IS}}{W_K}\,dk = \frac{\alpha k}{\pi k_m^2}(k_m - k)^2\,dk$$

where k is photon energy in MC^2, α is the fine structure constant $\approx \frac{1}{137}$, $W_{IS}\,dk$ represents the number of photons in the energy interval k to $k+dk$, and W_K is the probability for non-radiative capture. k_m is the upper energy limit of the bremsstrahlung spectrum. This quantity is related to the Q-value for the electron capture transition by

$$k_m = Q - E_{nl}$$

where Q represents the mass difference between parent and daughter atoms, and E_{nl} is the binding energy (positive) of an electron in the nl orbit. Therefore by measuring the bremsstrahlung spectrum one can determine the Q-value of the transition.

Experiments performed on a number of elements did not agree with the calculations of Morrison and Schiff.[6,7,8] In particular, the observed intensities were far higher than those predicted. The spectra of ^{55}Fe, ^{131}Cs, and ^{71}Ge showed an unexplained rapid rise in intensity at energies bordering on the characteristic x-ray region.

Considerable improvement of the theory for allowed capture processes was made by Martin and Glauber.[2,3] They took into account the nuclear coulomb field and considered capture from all atomic shells. They showed that the steep rise in intensity in the experimental data was due to IB photons accompanying capture from the L shell, specifically from the $2p$ electron states.

The results of Martin and Glauber generated an interest in the partial bremsstrahlung spectra, i.e., the spectra corresponding to 1s, 2s, 2p..., etc. capture separately. These were measured in a few cases for 1s capture by observing the bremsstrahlung spectra in coincidence with characteristic K x rays resulting from filling the vacancy in the K shell produced by the capture.[9,10] Biavati et al carried out such measurements on ^{55}Fe and ^{131}Cs, obtaining good agreement with the Martin and Glauber theory.

Further progress in the theory was made by Zon and Rapoport,[4,5] who developed formulae for the IB accompanying capture from an arbitrary shell, valid to any degree of forbiddeness, including allowed decays as well. They obtained the following expression for the spectral distribution of IB per K-capture for a first-forbidden unique transition:

$$\frac{W_{1S}(k)}{W_K}\,dk = \frac{\alpha}{\pi}\left[\left(1-\frac{k}{k_m}\right)^2 R^{(1)}_{1S}(k) + \left(\frac{k}{k_m}\right)^2 \tilde{R}^{(2)}_{1S}(k)\right]\left(1-\frac{k}{k_m}\right)^2 k\,dk$$

where

$$R^{(1)}_{1S}(k) = \tfrac{1}{2}\left(|A^{11}_{1S}|^2 + |B^{11}_{1S}|^2\right)$$

$$\tilde{R}^{(2)}_{1S}(k) = (2R\mu)^{2(\lambda_2-\lambda_1-1)}\, R^{(2)}_{1S}(k)$$

$$R^{(2)}_{1S}(k) = \frac{1}{8}\left[|A^{21}_{1S}|^2 + |B^{21}_{1S}|^2 + 3\left(|A^{22}_{1S}|^2 + |B^{22}_{1S}|^2\right)\right]$$

R = Nuclear Radius

$$\mu = \sqrt{M^2C^2 - (E_{1S}-k)^2}$$

$$\lambda_1 = \sqrt{1-(\alpha Z)^2}\,, \quad \lambda_2 = \sqrt{4-(\alpha Z)^2}$$

Here E_{1S} is the full energy of the electron on the K shell. The terms A and B are complicated functions of the energy of the bremsstrahlung photons, and depend on the integrals of products of spherical Bessel functions and Whittaker function (see equation 15 of Zon and Rapoport).

In the following we outline the steps leading to these expressions. For a detailed account of the theory, the reader is referred to the original papers.

Zon and Rapoport determined the amplitude for radiative capture of an electron from a state with energy $E_{n\ell}$, total angular momentum j_e, projection angular momentum m_e and remaining quantum numbers n for the nuclear transition $i \to f$ in terms of spherical tensor operators $T^{\lambda}_{\Lambda L \xi}$, where

$$T^{\lambda}_{\Lambda L \xi}(\vec{r}) = \sum i^L [L\xi M m | \Lambda \lambda] (\sigma_m \gamma_5)^{\xi} Y_{LM}(\vec{r}), \quad \xi = 0,1$$

These are tensors of rank Λ, and are eigenfuctions of the total lepton angular momentum. Here the total orbital angular momentum of the lepton pair, $\vec{L}$, with projection M, is coupled to the total spin of the leptons $\vec{\xi}$ which can be either in a triplet state, $\vec{\xi} = 1$, or a singlet state, $\vec{\xi} = 0$. The resulting total lepton momentum is $\vec{\Lambda}$ with projection quantum number λ. The quantities $[L\xi M m | \Lambda \lambda]$ are Clebsch-Gordon coefficients, and are matrix elements of the unitary transformation between the coupled and uncoupled representation.

The Feynman diagram corresponding to radiative capture can be represented as

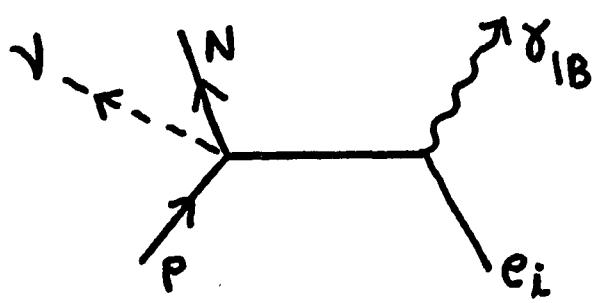

The amplitude for this diagram in terms of the spherical tensors $T^{\lambda}_{\Lambda L \xi}$ is

$$M = e \sum_{\Lambda L \xi \lambda} (-1)^{\Lambda+\lambda} \int dr_1 r_1^2 \int dr_2 \Big\{ d\Omega' \big[\psi_f^+(r') T^{\lambda}_{\Lambda L \xi}(r') (C_V + C_A \gamma_5) \psi_i(r') \big\}_{r'=r_1} \Big\{ d\Omega'' \big[\phi_\nu^+(r'') T^{-\lambda}_{\Lambda L \xi}(r'') (1+\gamma_5) G_E(r'', r_2) \tilde{A}(r_2) \phi_e(r_2) \big] \Big\}_{r_2=r_1}$$

Here C_V and C_A are the vector and axial vector coupling coefficients, ϕ is the total lepton wave functions, ψ the nuclear wave functions, G_E the Green's function of an electron in a Coulomb field, and $E = \epsilon - k$, where ϵ is the energy of the electron in the orbit from which capture occurs.

This expression can be further reduced by expressing $G_E(r_1, r_2)$ in terms of $\mathcal{G}_E(r_1, r_2)$, which is the solution to the second order Green's equation (see appendix I of Zon and Rapoport[4]), and by expanding the wave functions of the photon and neutrino in eigenfunctions of the angular momentum operator. These wave functions are assumed to be plane wave states with momenta $\vec{k}$ and $\vec{q}$ and respective polarizations $\vec{e}_s$ and $\vec{e}_\sigma$ $(s = \pm 1, \sigma = \pm \frac{1}{2})$. The function $\mathcal{G}_E$ was determined and investigated by Martin and Glauber[2,3]. Zon and Rapoport exclude the region of the nucleus in the integration over the volume of the atom and assume the validity of the approximation, i.e.,

$$Z\alpha \gg R(E_i - E_f)$$

where R is the nuclear radius.

Substituting $\mathcal{G}_E(r_1, r_2)$ into the probability amplitude M,

the following expression is obtained for the probability of emission of a photon with energy k and polarization S, where the nuclear and electronic parts of the amplitude are factored out

$$W_{j_e}(k,S) = \frac{4\alpha}{\pi} \sum_{\Lambda N j_\nu j_\gamma} \frac{2j_\gamma - N + 1}{2N} \left[\frac{2^{N-1}(N-1)!}{(2j_\nu)!!(2N-1)!} \right]^2$$

$$(2\mu R)^{2(\lambda_N - N)} q^{2j_\nu - 1} k^{2N-2} \left| \eta^{\wedge}_{N j_\nu} \right|^2 \left| \Phi^{N j_\nu}_{j_e(S)} \right|^2 k q^2$$

The quantity $\eta^{\wedge}_{N j_\nu}$ contains the nuclear part of the amplitude, while $\Phi^{N j_\nu}_{j_e}(S)$ contains the electronic part of the amplitude. $\eta^{\wedge}_{N j_\nu}$ is determined by the nuclear matrix elements. For the first-forbidden unique capture transition in ^{204}Tl, $\eta^{\wedge}_{N j_\nu}$ becomes:

$$\Delta J = 2, \Lambda = 2, N = 2, j_\nu = \tfrac{1}{2}, \text{ or } \eta^2_{2,\frac{1}{2}} = i C_A \int r T_{211} \gamma_5$$

$$\Delta J = 2, \Lambda = 2, N = 1, j_\nu = \tfrac{3}{2}, \text{ or } \eta^2_{1,\frac{3}{2}} = -i C_A \int r T_{211} \gamma_5$$

And so

$$\left| \eta^2_{2,\frac{1}{2}} \right|^2 = \left| \eta^2_{1,\frac{3}{2}} \right|^2 = C_A^2 \left(\int r T_{211} \gamma_5 \right)^2$$

The quantity $\Phi^{N j_\nu}_{j_e}$ can be expressed in terms of the photon polarization as follows:

$$\Phi^{N j_\nu}_{j_e(S)} = \frac{\langle \Phi \rangle}{M \sqrt{2(2\mu R)^{\lambda_1 - 1}}} \left(S A^{N j_\nu}_{1S} - B^{N j_\nu}_{1S} \right)$$

where M is the electron rest mass,

$$\langle\Phi\rangle = \sqrt{\frac{1-\lambda_1}{\pi a^3 \Gamma(1+2\lambda_1)}}\left(\frac{2R}{a}\right)^{\lambda_1-1}$$

is the mean value of the wave function of the K electron on the surface of the nucleus, a is the Bohr radius, and $A_{1s}^{Nj_\nu}$ and $B_{1s}^{Nj_\nu}$ are complicated functions of the energy of the bremsstrahlung photons, and are expressed in terms of $Z\alpha$ and radial integrals. For the sake of brevity, these quantities have not been included here. The reader is referred to equation 15 of Zon and Rapoport for these expressions.[4]

Zon and Rapoport evaluate $A_{1s}^{Nj_\nu}$ and $B_{1s}^{Nj_\nu}$, and hence the electronic part of the amplitude, $\Phi_{je}^{Nj_\nu}$, to different orders of the expansion in αZ. In their first paper, they obtain the first two terms of the expansion. In the zeroth order in αZ, the quantities $A_{1s}^{Nj_\nu}$ and $B_{1s}^{Nj_\nu}$ equal unity. For first order in αZ they obtain the simple expression

$$A_{1s}^{Nj_\nu}\left(B_{1s}^{Nj_\nu}\right) = 1-(\alpha Z)\sum_{m=0}\left(a_m\frac{u}{k}+b_m \operatorname{arctg}\frac{k}{\mu}\right)\left(\frac{M}{k}\right)^m$$

The coefficients a_m and b_m are tabulated[4]. Thus for an accuracy to αZ, the A_{1s} and B_{1s} terms depend only on the energy of the bremsstrahlung photons. In the case of the heavy nucleus ^{204}Tl, however, this expression is not valid, since $\alpha Z = 0.59$.

Because of the complexity of higher terms in the expansion of A_{1s} and B_{1s}, Zon uses computer calculations, and in a second paper obtains an accuracy to all orders in αZ. In table I we list these values of $R_{1s}^{(1)}$ and $\tilde{R}_{1s}^{(2)}$. These

values have been used to obtain W_{IS}/W_K for various values of k_m, the end-point energies of the IB spectra, and are included in Table I. The values chosen for k_m were based on an examination of the experimental spectrum, and correspond to the energies of the channels in the vicinity of the endpoint. These spectra are plotted in Figure 1. Note that these spectra give the IB intensity per sec per keV, and that a scale factor of $(511)^{-1} \times 10^{-4}$ is used. The figures show the IB spectra for energies greater than 100 keV, since this was the region of investigation in the experimental data.

In order to convert the theoretical spectra into a form suitable for comparison with the experimental spectrum, the IB spectra must be expressed in intensity per second per channel, i.e., as

$$\frac{W_{IS}(k)}{W_K} \times \Delta k$$

where Δk is the channel width (=9.26 keV), and k is the energy corresponding to the center of the channel. These values were obtained by interpolation from the data in Table I, and are presented in Table II. These differential spectra can now be multiplied by the Response Matrix (see section on Detector Response Matrix) in order to obtain the theoretically predicted IB pulse height spectra (see Analysis and Conclusions).

An early analysis of the Zon and Rapoport theory resulted in an IB intensity which was several times higher than experimental estimates and the Morrison and Schiff theory.

Previous investigations of IB have shown that in medium to heavy nuclei, the total IB intensity depends on Z, as a result of Coulomb and relativistic effects. For allowed transitions, the Martin and Glauber theory has successfully accounted for these effects by a correction factor R_{IS} which multiplies the Morrison and Schiff expression. This factor has only a small influence on the shape of the spectrum. Since these studies have shown the importance of Coulomb effects on the intensities of the theoretical spectra, it was of interest here to consider the effect of Z in the Zon and Rapoport theory, and compare the experimental spectrum to a Coulomb-free version of this theory. This is obtained from the relation for W_{IS}/W_K by setting $Z=0$. One finds $R_{IS}^{(1)} \to 1$, $\tilde{R}_{IS}^{(2)} \to 1$, and thus

$$\frac{W_{IS}(k)}{W_K}\,dk = \frac{\alpha}{\pi}\left(1-\frac{k}{k_m}\right)^2\left[\left(1-\frac{k}{k_m}\right)^2+\left(\frac{k}{k_m}\right)^2\right]k\,dk.$$

This expression is identical to that obtained by application of the Cutkosky rule.[11]

According to this rule the expression for first-forbidden unique transitions in the $Z=0$ approximation can be obtained from the allowed expression of Morrison and Schiff by multiplication by the factor (k^2+q^2), where q is the neutrino momentum.

This expression gives a lower intensity for the IB photon spectrum than the full Zon expression, and as will be shown in the Analysis and Conclusions, gives better agreement with

the intensity of the experimental spectrum. The Coulomb-free differential spectra are listed in Table III, and plotted in Figure 2. The comparison of the experimental data and the Coulomb-free theory gives a lower end-point energy for the IB spectrum than a similar comparison made with the full Zon and Rapoport theory. For this reason the differential spectra listed in Table III are computed at lower end-point energies.

It can be seen from a comparison of the theoretical spectra that the intensities of the Coulomb-free spectra have a stronger dependance on k_m than the intensities of the spectra based on the full theory.

REFERENCES - THEORY

1. P. Morrison and L. Schiff, Phys. Rev. 58, 24 (1940).
2. R. J. Glauber and P. C. Martin, Phys. Rev. 104, 18 (1956).
3. P. C. Martin and R. J. Glauber, Phys. Rev. 109, 1307 (1958).
4. B. A. Zon and L. P. Rapoport, Sov. J. Nucl. Phys. 7, 330 (1968).
5. B. A. Zon, Sov. J. Nucl. Phys. 13, 554 (1971).
6. L. Madansky and F. Rasetti, Phys. Rev. 94, 407 (1954).
7. B. Saraf, Phys. Rev. 94, 642 (1954).
8. B. Saraf, Phys. Rev. 95, 97 (1954).
9. M. H. Biavati, S. J. Nassif and C. S. Wu, Phys. Rev. 125, 1364 (1962).
10. A, Michaelowicz, Compt. Rend. 242, 108 (1956).
11. R. E. Cutkosky, Phys. Rev. C5, 1222 (1954).

CALCULATED VALUES OF W_{IS}/W_K

$(W_{IS}/W_K) \times 10^4$ For various values of k_m

k (mc^2)	k keV	$R^{(1)}_{IS}$	$\tilde{R}^{(2)}_{IS}$	$k_m \rightarrow$	260	279	297	316	334	353
.200	102.2	.323	23.820		6.50	6.21	5.91	5.62	5.33	5.07
.225	115.0	.317	17.750		5.81	5.65	5.46	5.25	5.03	4.82
.250	127.8	.312	13.590		5.05	5.02	4.93	4.81	4.67	4.51
.275	140.5	.307	10.640		4.28	4.37	4.38	4.33	4.26	4.16
.300	153.3	.302	8.487		3.52	3.71	3.81	3.84	3.83	3.79
.325	166.1	.297	6.861		2.80	3.06	3.23	3.33	3.38	3.39
.350	178.9	.293	5.634		2.16	2.49	2.69	2.85	2.95	3.00
.375	191.6	.289	4.676		1.54	1.90	2.18	2.38	2.52	2.62
.400	204.4	.285	3.928		1.04	1.41	1.71	1.94	2.12	2.25
.425	217.2	.281	3.324		.62	.98	1.28	1.54	1.74	1.90
.450	230.0	.278	2.836		.31	.62	.91	1.18	1.39	1.57
.475	242.7	.274	2.438		.10	.34	.60	.86	1.08	1.27
.500	255.5	.270	2.110		.007	.14	.36	.59	.80	.99
.525	268.3	.267	1.838		.00	.03	.17	.37	.57	.75
.550	281.1	.264	1.610			.00	.05	.20	.37	.54
.575	293.8	.261	1.415				.002	.08	.21	.37
.600	306.6	.258	1.253					.013	.10	.23
.625	319.4	.255	1.150						.03	.12
.650	332.1	.252	1.100						.0	.05

TABLE II

IB INTENSITY $\times 10^{-7}$ PER SECOND PER CHANNEL PER K-CAPTURE FROM ZON AND RAPOPORT

CHANNEL NUMBER	CHANNEL ENERGY	SPECTRA k_m VALUES (keV)					
		260	279	297	316	334	353
10	98.0	121.04	114.87	108.71	103.28	97.48	92.77
11	107.3	113.06	109.08	103.64	99.29	94.58	90.23
12	116.5	103.64	101.47	97.84	93.86	90.60	86.79
13	123.8	93.49	92.77	91.32	88.06	85.52	83.35
14	136.1	83.35	84.25	83.35	81.90	80.45	77.73
15	144.3	73.93	75.38	76.10	75.38	75.01	73.20
16	153.6	63.78	66.68	68.49	68.85	69.21	67.77
17	162.8	55.08	57.98	60.88	62.15	63.24	63.42
18	172.1	46.75	50.19	53.63	55.99	57.62	58.16
19	181.4	38.05	42.76	47.11	49.28	51.82	52.91
20	190.6	29.72	35.51	40.22	43.49	43.49	47.83
21	200.0	21.02	28.45	33.70	37.69	40.77	42.94
22	209.1	15.22	20.66	28.27	32.43	35.88	38.23
23	218.4	10.15	17.21	22.83	27.18	30.80	33.70
24	227.7	5.80	12.68	18.12	22.83	26.45	29.17
25	236.9	3.26	8.15	13.05	18.12	22.29	25.37
26	246.2	1.45	5.25	9.42	13.77	18.12	21.92
27	255.4	0.36	2.72	6.16	10.51	14.50	18.12
28	264.7	0.0	1.09	3.62	7.61	12.23	14.86
29	273.9		0.36	1.99	5.07	8.52	11.96
30	283.2		0.0	0.73	3.08	5.97	9.42
31	292.5			0.36	1.45	4.35	7.07
32	301.7			0.0	0.73	2.17	5.25
33	311.0				0.36	1.45	3.62
34	320.2				0.0	0.73	2.36
35	329.5					0.36	1.45
36	338.8					0.0	0.73
37	348.0						0.36

TABLE III

IB INTENSITY X 10^{-7} PER SECOND PER CHANNEL PER K-CAPTURE FROM ZON AND RAPOPORT COULOMB-FREE THEORY

CHANNEL NUMBER	CHANNEL ENERGY	SPECTRA k_m VALUES (keV)					
		223	242	260	279	297	316
10	98.0	12.88	14.76	16.63	18.45	20.23	21.95
11	107.3	11.92	13.82	15.72	17.59	19.43	21.23
12	116.5	10.97	12.88	14.79	16.68	18.56	20.41
13	123.8	10.22	12.13	13.83	15.73	17.63	19.51
14	136.1	8.93	10.86	12.87	14.78	16.68	18.58
15	144.3	8.05	10.00	11.92	13.83	15.73	17.64
16	153.6	7.01	9.01	10.96	12.87	14.78	16.68
17	162.8	5.93	7.99	9.98	11.91	13.83	15.74
18	172.1	4.79	6.92	8.96	10.93	12.86	14.78
19	181.4	3.63	5.80	7.91	9.97	11.89	13.81
20	190.6	2.49	4.66	6.82	8.89	10.90	12.85
21	200.0	1.43	3.49	5.68	7.81	9.87	11.86
22	209.1	0.59	2.39	4.54	6.70	8.81	10.85
23	218.4	0.07	1.37	3.38	5.55	7.71	9.79
24	227.7	0.0	0.55	2.28	4.39	6.58	8.71
25	236.9		0.07	1.30	3.26	5.42	7.59
26	246.2		0.0	0.52	2.18	4.26	6.44
27	255.4			0.07	1.23	3.14	5.29
28	264.7			0.0	0.49	2.09	4.14
29	273.9				0.06	1.18	3.04
30	283.2				0.0	0.46	2.01
31	292.5					0.06	1.12
32	301.7					0.0	0.44
33	311.0						0.05
34	320.2						0.0
35	329.5						
36	338.8						
37	348.0						

SPECTRAL DISTRIBUTION OF IB PER K-CAPTURE FROM ZON AND RAPOPORT

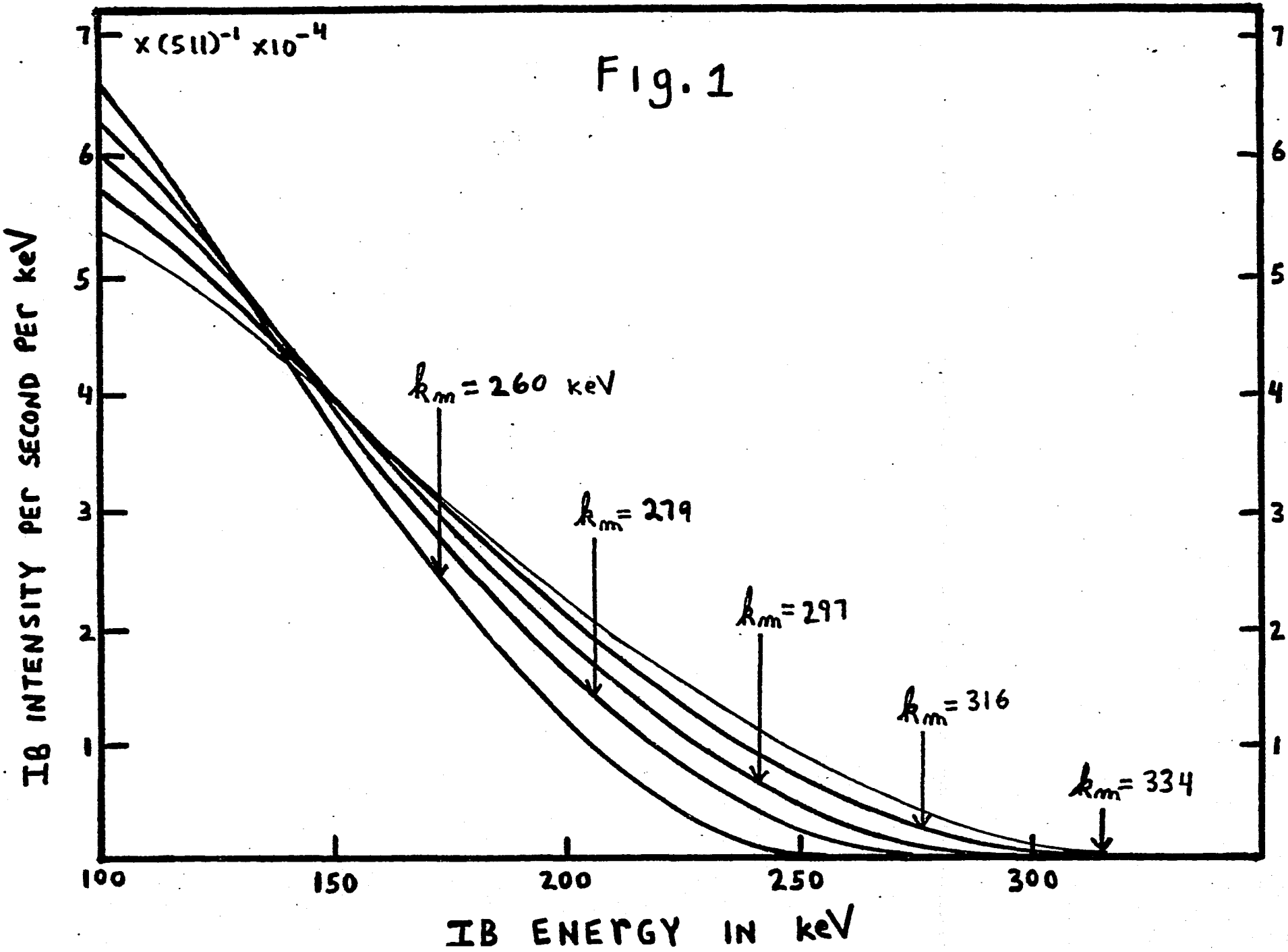

SPECTRAL DISTRIBUTION OF IB PER K-CAPTURE
ZON AND RAPOPORT COULOMB-FREE

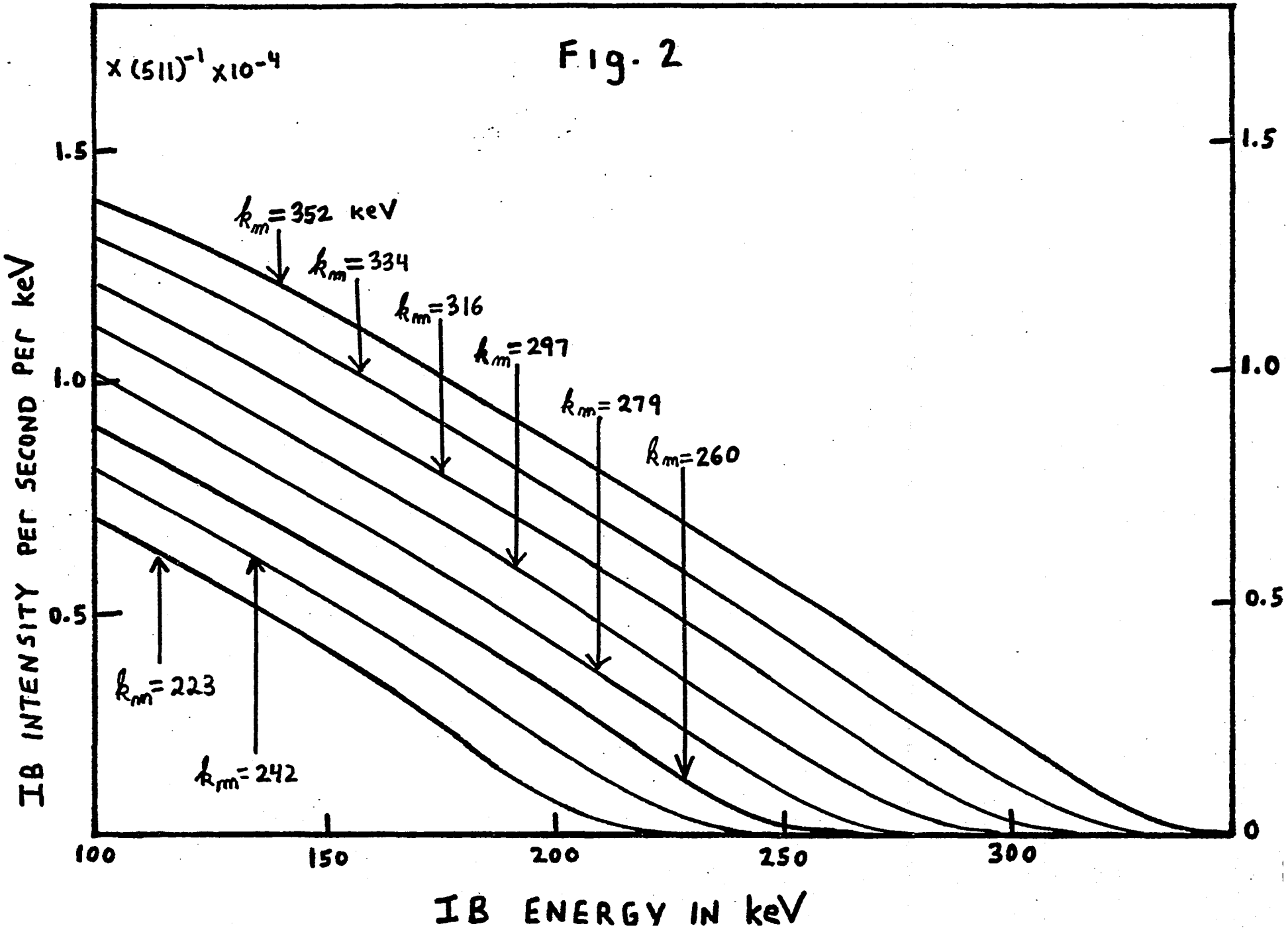

III. COINCIDENCE DATA

III.1 DATA COLLECTION

The coincidence data was taken in both "trues" and randoms on multichannel analyzers operating in two-parameter analysis mode for a total of 329.5 hours. A slow-fast coincidence system was used to select the coincident photons of interest and to separate the random coincidence data from the "true," i.e., total coincidence data. The data was stored in the memories of two 4096 channel analyzers, and arranged in a 64- X 64-channel matrix array. The axes of the matrix represented the energies of the coincident photon species, and the two-parameter format allowed measuring the number of photon coincidences versus their energies.

This arrangement of data enabled viewing it on the isometric display modes of the analyzers, which was especially convenient for visualizing the various coincident effects, and for identifying erroneous data introduced by power transients. An example of the isometric display of data is shown in Fig. 3 in the section on System Coincidence Efficiency. The reader is referred to the section on Experimental Geometry and Electronics for additional information on the coincidence technqiue.

It is convenient to define the symbol N(i.j) as the number of counts stored at a point on the matrix with coordinates (i.j). This number is proportional to the number of coincident photons emitted by the source with energies corresponding to pulse heights, i,j. The j parameter was

used for the bremsstrahlung radiation, while the i parameter was reserved for the x-rays. A Harshaw 3-in. x 3-in. NaI(Tl) detector was used to measure the bremsstrahlung radiation over the energy range 15-598 keV, and the x-ray data was collected with a low temperature Ortec LEPS (Low Energy Photon System) Ge(Li) spectrometer over the energy range 65-87 keV. Additional information on the detectors are included in the sections on Experimental Geometry and Detector Calibrations.

In order to perform daily checks on the detector calibrations, and adjust the system for changes in gain and drift of the zero level, the axes of the matrix were reserved for the storage of "singles" spectra, which were obtained by releasing the coincidence requirements on the system.

The coincidence data are presented in Figs. 2-17. These spectra correspond to the rows of the two-parameter, 64 X 64 matrix of coincident events, in which each row represents the complete spectrum of Ge(Li) detector pulses along one of the channels of the NaI(Tl) detector spectrum. Thus the coincidence spectrum in row 12 represents x-ray photons which all have common coincidences with bremsstrahlung photons belonging to channel 12 of the NaI(Tl) detector spectrum. The matrix may be viewed as rows of spectra, where each row has width ΔE which spans an energy interval from $(E-\frac{\Delta E}{2})$ to $(E+\frac{\Delta E}{2})$ of the bremsstrahlung spectrum, and where E equals the energy at the center of the interval in keV. The width ΔE of the bremsstrahlung channel was maintained constant throughout the experiment at 9.26 keV per channel. The energy

corresponding to row j may be determined using the formula developed in the calibration of the NaI(Tl) detector, i.e.,

$$E(keV) = 9.26j + 5.43 \quad .$$

Although the data was acquired in a 64 X 64 matrix, in order to reduce calculation times necessary to determine certain processes and improve counting statistics, adjoining rows of the matrix were combined pairwise to produce a reduced 32 X 64 matrix, with the shorter dimension specifying the channels of the NaI(Tl) detector spectra. The data presented in Figures 2-17 represent this condensed version of the original matrix.

In general, the true coincidence data was collected on the Nuclear data 3300 multichannel analyzer, and the random coincidence data collected on the Northern Scientific NS-636 memory coupled to the NS-623 ADC (analog-to-digital converter). When it was feasible, the analyzers were run simultaneously in order to minimize the total time spect collecting data. Trhough various modes of operation, both analyzers allowed continuous monitoring of the data. The ND 3300 was hard-wired with various programs to handle the data. The NS-636 was soft-wired and interfaced to a PDP-11 computer; a program was written on paper tape to allow close observation of the data stored in this analyzer.

III.2 ANALYSIS OF COINCIDENCE DATA

III.2.1 INTERNAL BREMSSTRAHLUNG IN THE CAPTURE OF K ELECTRONS

The coincidence spectra (Figs. 2-17) reveal the internal bremmstrahlung connected with the electron capture decay in ^{204}Tl. However, there are other higher order effects in the data which are associated with the beta decay branch. These additional phenomena will be discussed in the next section (III.2.2).

Each spectrum contains the "trues" data, that is, the total coincidence data with the random coincidences subtracted. Although the randoms data are not presented, on the average they accounted for about one-half of the total coincidence data, as can be seen from an examination of the time spectrum (refer to section on Experimental Geometry and Electronics, Fig. 5). There the ratio of the total area under the peak to the background under the peak is two-to-one. It is also possible to know the true-to-random ratio for each spectrum by referring to the tabular summary of the coincidence data included in this section (see Table 1). This table is constructed so that the number of trues, randoms, and background counts are presented for all the coincidence spectra.

In order to facilitate interpretation of the coincidence data, it will be useful to refer to the decay scheme of ^{204}Tl (Figure 1).[1] This source decays primarily by beta decay to the ground state of ^{204}Pb and by electron capture to the ground state of ^{204}Hg. It is through the latter

mode of decay that the characteristic x rays of Hg are produced.

As is well known, in electron capture a vacancy is produced in an atomic shell, which is quickly filled by an electron from a higher shell. As a result of this transition, energy is released, which may be in the form of characteristic x-rays. By detecting the photons that occur in coincidence with these x rays, it is possible to determine the spectrum of internal bremsstrahlung photons associated with capture from these shells.

The original purpose of this investigation was to measure the IB spectrum resulting from K-shell capture in ^{204}Tl. This effect is recognized by the presence of the Hg K x-ray peaks in the coincidence data. The resolution of the Ge(Li) spectrometer was sufficient to resolve the components of the Hg K x rays. These x rays are as follows:[3]

K_α	K_β
$K_{\alpha_1} = 70.82$ keV	$K_{\bar{\beta}_1} = 80.20$ keV
$K_{\alpha_2} = 68.89$	$K_{\bar{\beta}_2} = 82.50$

The K_{α_1}, and the K_{α_2} x rays represent discrete transitions between the $K\text{-}L_{III}$ and the $K\text{-}L_{II}$ shells respectively, whereas the complex lines $K_{\bar{\beta}_1}$ and $K_{\bar{\beta}_2}$ are the weighted averages of the transitions between the K-M and K-N shells, respectively. These lines are separated only by instruments of high resolving power. The nomenclature $K_\alpha = K_{\alpha_1} + K_{\alpha_2}$

and $K_{\beta} = K_{\bar{\beta}_1} + K_{\bar{\beta}_2}$, is also often used.

The principal features of the coincident spectra are the K_{α} and K_{β} x-ray peaks. The partial components $K_{\alpha_1}, K_{\alpha_2}$, and $K_{\bar{\beta}_1}, K_{\bar{\beta}_2}$ are not easily distinguished from each other because of their low counting rates and small energy differences, whereas the K_{α} and K_{β} lines which appear at the lower and upper halves of the spectra are rather well distinguished. In order to demonstrate the presence of all the K x-ray compenents in the coincidence data, the individual spectra corresponding to bremsstrahlung channels 11-40 were combined, and the result is shown in Fig. 2. This summed spectrum can be compared to the Ge(Li) singles spectrum, in which all the K x-ray components are clearly defined. The two spectra were in good agreement with respect to the positions of the x-ray peaks.

It was also of interest to compare the ratios of the Hg $K_{\bar{\beta}}$ to- K_{α} x-ray intensities obtained from these spectra to the value obtained from A. Salam's[4] careful measurements on radiative transition probabilities. Although the values obtained from the present measurements were in good agreement ($K_{\bar{\beta}}$ -to- K_{α} ratio of 0.232 from the sum coincidence spectrum and 0.236 for singles spectrum), they were in disagreement with Salam's value of 0.277.

A careful analysis showed the discrepancy between Salam's work and the present work to be due to the difference in detection efficiencies between the Hg K_{α} and Hg $K_{\bar{\beta}}$ x-rays in the Ge(Li) detector, and the escape of germanium x rays from the face of the detector. The intrinsic efficiency of

the Ge(Li) spectrometer varies uniformly over the energy range of the mercury K x rays, and is about 8% higher for the K_{α} x rays than the K_{β} x rays. The detection efficiency for these x rays is also complicated by the presence of the Ge K x-ray escape effect, which occurs as follows: In the interaction of an Hg K_{β} x-ray photon with the Ge(Li) detector, it is possible that a germanium K x ray ($\approx$ 10 keV) will be excited in the crystal's surface. If this x ray escapes absorption in the crystal, then the energy taken up by the detector is equal to the difference in energy between the Hg K_{β} x ray and the Ge K x ray. This energy corresponds to a channel which is lower than the channels occupied by the Hg K_{β} x-ray pulses, but which is in the range of channels intercepted by the Hg K_{α} x-ray pulses. Thus those events in which a Hg K_{β} photon is partially absorbed in the Ge(Li) detector by this mechanism will be incorrectly counted as an Hg K_{α} photon, and there will consequently be an overcounting of Hg K_{α} x rays. Simiarily, the escape effect can be induced by the Hg K_{α} x rays, and this will result in a reduction in intensity of the Hg K_{α} peak.

In order to determine the magnitude of this effect, the biased amplifier was disconnected from the Ge(Li) branch of the system, and a singles spectrum of pulses below the range of the Hg K x rays was taken. In this way it was possible to observe the escape peak corresponding to the excitation of Ge K x rays by the Hg K_{α} x rays. The intensity of this peak was about 3% of the Hg K_{α} peak intensity.

After including corrections for the variation in detector efficiency and the escape effect in the measured value of the K_β-to-K_α ratio, the value 0.252 was obtained, which is in satisfactory agreement with Salam's value.

The intensities of the IB in the separate coincidence spectra were determined by summing over the channels in the x-ray peaks, and subtracting the background contribution to these channels. This gave the IB intensities belonging separately to the K_α and the K_β x rays of each coincidence spectrum. The start and stop channels used in these summations were the same for all the spectra, and were obtained from the singles Ge(Li) spectrum, where the channel boundaries of the x-ray peaks could be determined very accurately. The background in the spectra were determined by a weighted least squares computer fitting program; an interpolation procedure was used to obtain the background in the x-ray channels. The details of these calculations are presented in Section III.3 — Reduction of Data.

The intensity of IB in each spectrum is plotted against spectrum number in Fig. 18. Also shown in this plot is the IB energy equivalent for each spectrum. As was mentioned previously, spectra have been paired up, and the energy shown is the average energy of the paired spectra. The error bars shown are based on counting statistics, and include random and background effects. This plot is the pulse-height distribution of the IB photon spectrum, and was compared to the theoretically predicted spectra after the effects of the

detectors were folded into the theoretical spectra. This procedure involves converting the theoretical spectrum into a pulse-height distribution, and is described in Section VI—Response Matrix of the NaI(Tl) Detector.

An examination of the experimental IB spectrum shows a generally decreasing photon intensity in the direction of increasing photon energy, with almost vanishing of the photon spectrum at energies corresponding to channels 29 and 30.

A detailed analysis and χ^2 calculation of the theoretical spectrum which best fits the experimental data was used to determine the total intensity and end-point energy of the IB spectrum, and to compare it with the various theoretical spectra. This is included in the section—Analysis and Conclusions.

REFERENCES

INTERNAL BREMSSTRAHLUNG IN THE CAPTURE OF K ELECTRONS

1. C.M. Lederer, J.M. Hollander, and I. Perman, "Table of Isotopes" (John Wiley and Sons, Inc., New York, 1967), 6th edition.

2. R. J. Glauber and P. C. Martin, Phys. Rev., 104, 158 1956).

3. J. A. Bearden and A. F. Burr, in Handbook of Chemistry and Physics (CRC Press, Inc., Cleveland, Ohio). 54th edition, 1973-1974, pp. E. 181- E 192.

4. S.I. Salam, in Handbook of Chemistry and Physics (CRC Press, Inc., Cleveland, Ohio), 54th edition, 1973-1974, p. E 194.

5. H. Lancman and A. Bond, Phys. Rev. C7, 2600 (1973).

III.2 ANALYSIS OF COINCIDENCE DATA

III.2.2 INTERNAL BREMSSTRAHLUNG ACCOMPANYING AUTOIONIZATION IN ^{204}Pb

In addition to the x rays associated with the IB, the coincidence spectra contain several components originating in other higher order radiative processes accompanying the decay of ^{204}Tl. To discuss these contributions we consider three regions of the x-ray spectra (Fig. 2).

The first region (I) corresponds to two sections of the spectrum. The spectrum in channels one through six appears approximately equal in intensity to that in channels 36 through 42. In addition, these sections are lower in intensity than the rest of the spectrum. The second region (II) corresponds to channels 22 through 34. The lower border of this range is contiguous to the high energy tail of the mercury $K\alpha_1$ x-ray peak. Two peaks occupy this range; their shapes and widths are so similar to the Hg K x-ray peaks that one is tempted to consider them another set of x rays. The third region (III) corresponds to the right edge of the spectrum, in channels 58 to 63. This region is clearly lower than region II, and a poorly defined peak is discernible on a background level approximating region I. This general appearance is exhibited in all the coincidence spectra. In the following pages we discuss the various physical effects which produce these shapes.

A comparison of the data shows that the background to foreground (here "foreground" is meant to denote x rays) ratio is considerably higher in the coincidence spectra than in the

singles (x ray) spectra. In the former it is about 2:1, while in the latter it is approximately 2:17. This difference is not surprising and is primarily due to a physical effect which greatly enhances the background in the coincidence spectra, but is not present in the singles spectrum. This effect is called double internal bremsstrahlung (DIB),[1,2,3] and is most clearly seen in region I described above, where it is not obscured by other effects. This effect, which occurs over the whole spectrum, is the greatest contribution to the background, and is responsible for the high background to foreground ratio.

DIB is the simultaneous emission of two photons accompanying beta decay, as opposed to the more probable single photon emission. This latter process is known as single internal bremsstrahlung (IB).[4-8] The origin of these processes is the interaction between the beta particle and the emitting nucleus. In IB the electron interacts with the radiation field once, while in DIB it interacts twice. These processes are to be distinguished from the corresponding external bremsstrahlung processes, DEB and SEB, which occur when external bremsstrahlung is emitted when an electron interacts with a nucleus other than its parent nucleus.[9-10] The transition probability for IB is of the order of the fine structure constant α ,[4] where α = 1/137, whereas the transition probability for DIB is of the order of α^2.[2]

The IB in beta decay has been extensively studied,[8] but the DIB has been investigated in only three cases,[1-3] and

observed in two of them.[1,2] The energy distributions of the DIB photons are continuous, and the energy available for the process is the same as in IB, which is the beta decay transition energy. This was demonstrated experimentally by showing that the end-point of the photon-sum coincidence spectrum occurs at the beta spectrum endpoint.[1,2]

Although the ratio of the probability of DIB compared to the probability of beta decay is much lower than the ratio of the probability of radiative K-capture to the probability of non-radiative capture, the observation of DIB in the present data is greatly enhanced in comparison to IB (from K-capture) as a result of the high beta decay-to-electron capture branching ratio in ^{204}Tl. This ratio is 98:2; thus, the high percentage of decays through the beta branch compensates for the low probability of the DIB process. This explains why the much weaker DIB competes with the IB (in K-capture) in the coincidence data.

The IB (in beta decay) does not contribute to the coincidence data, since the beta particles are absorbed by the 320 mg/cm^2 thick beryllium sheets surrounding the source, thus preventing the possibility of beta-gamma coincidence pulses. However, in the case of a DIB event, it is possible that both photons will be detected to produce a coincidence pulse. This can occur if the photons detected in both branches of the system satisfy the energy restrictions assigned to those branches. As noted previously, the Ge(Li) x-ray branch passed photons with energies only in the range

of 65-87 keV, while the bremsstrahlung branch passed virtually all energies of photons.

Although the DIB constitute a large component of the coincidence spectra, its evaluation did not present too much difficulty. Since it is known from the previously mentioned studies that the DIB is continuous in both photon branches, and since the range of the DIB spectrum in ^{204}Tl is approximately 765 keV, it does not vary appreciably over an energy interval of $\approx$ 22 keV, the range of the Ge(Li) spectra. In addition, the use of a biased amplifier in conjunction with a high resolution Ge(Li) spectrometer allowed the K_α and K_β x-ray peaks to be separated by a margin wide enough to confidently measure the DIB and other phenomena between them.

As previously discussed, region I of the spectrum consists of sections located both to the left and right of the K_α x-ray peak which do not vary significantly in intensity; thus region I is composed predominantly of DIB. In view of these observations, region I was used to estimate the background to the K_α x-ray peak. The calculations are presented in the next section (III.3).

Another contribution to the coincidence spectra can arise from photons scattered from one detector into the other. This can occur when a primary (source) photon interacts with one detector by a Compton collision, and the scattered photon interacts with the second detector. These events will occur in true time coincidence, and if the energies left

in both detectors satisfy the energy requirements on the system, then a coincidence pulse will result. In the experimental set-up, the detectors were arranged face-to-face and in close proximity, which resulted in substantial scattering between them. In order to reduce this to an acceptable level, a specially designed tin filter was positioned between the detectors. The details of this filter are described elsewhere (see section on "Experimental Geometry").

An examination of the various scattering possibilities will show that with the filter in place, the dominant scattering contribution to the coincidence data is from the following mechanism: Assume a source photon enters the Ge(Li) detector, where it is Compton scattered 180^{o} into the NaI(Tl) detector. From the Compton scattering formula, one can show that the energy of the backscattered photon E_{γ} in terms of the energy of the Compton recoil electon E_c is:

$$E_{\gamma} = \frac{E_c \pm \sqrt{E_c^2 + 1022 E_c}}{2},$$

where E_{γ} and E_c are in keV.

Thus for a range in Compton electron energies of 65-87 keV, which is the pre-selected energy range in the Ge(Li) branch, the corresponding energy range for the backscattered photons is 100-113 keV. This can occur for primary photon energies 165-200 keV, and can be derived both from external and internal bremsstrahlung.

Although the energy of the backscattered radiation is

essentially monochromatic and will be centered on channel 11 of the NaI(Tl) branch, the finite resolution of the detector will spread this line over several channels, and it will be strongest in channels 11 and 12. The background in coincidence spectra 11 and 12 combined (Fig. 3) is indeed high and uniform. The two-parameter analysis allowed the scattering peak to be separated from the IB data; however, the large background resulted in an increase in the statistical uncertainty of the IB in these channels.

Region II of the spectrum includes channels 23 to 34. This region was distinguished by the presence of two peaks. These peaks appear in all coincidence spectra; their presence is clearly seen in the sum coincidence spectrum. In order to attempt an explanation of their origin, we must first refer to the singles spectra (Fig. 19) of ^{204}Tl taken on the Ge(Li) spectrometer.

The region between the Hg K_{α} and Hg K_{β} x rays appears flat in this spectrum; however, under closer scrutiny a more complicated structure is revealed. When the channels in this region are plotted on a more sensitive scale, two peaks are observed (Fig. 20). A prominent peak appears centered between channels 30 and 31, and a less prominent peak is discernible on the high energy tail of the Hg K_{α_1} x-ray peak. The average energy of channels 30 and 31 is 74.94 keV; this corresponds to the energy of the Pb K_{α_1} x rays, which is listed as 74.97 keV by Bearden and Burr.[12] The less prominent peak appears approximately six channels lower in channel 24, at

an energy of 72.81 keV, which matches the energy of the Pb $K\alpha_2$ x-ray line.

The presence of lead x rays in the singles data after background was subtracted could be caused by excitation in the bricks from the source emissions. This possibility was carefully checked: spectra were taken both with and without the presence of 0.25-inch-thick cadmium and copper selective absorbers lining the inside of the brick house. No change was found in the intensity of the Pb x-ray peaks.

Another possibility was the scattering of mercury K x rays from the tin filter or cadmium ring. The cadmium ring was positioned on the side of the source nearest the Ge(Li) detector, in order to reduce the possibility that photons backscattered from the Ge(Li) detector would pass through the hole in the tin filter. Since the cadmium ring was closer to the source than the tin filter, it presented the greater opportunity for scattering. It is difficult to calculate the energy of these scattered photons, since the angle between the source, ring, and detector could not be determined with certainty because of the finite size of the source. Assuming 90° scattering of the incident $K\bar{\beta}_1$ x-ray photons from the cadmium ring would put the energy of the scattered photons at 69.3 keV, while scattering of the $K\bar{\beta}_2$ photons through the same angle would give 71.0 keV scattered photons. Thus although these scattered photons would not appear in region II of the background, they would add to the $K\alpha$ x-ray peaks. For scattering angles less than 90°, which is more likely to occur

since the source is not included in the plane of the ring, the scattered photons would carry off greater energies, and would contribute to the pulses in region II.

In order to determine the effect of Hg K_{β} - photon scattering on these regions of the spectra, the cadmium ring was removed, and several spectra were taken. These spectra showed no change in the peaks of region II when compared to spectra taken with the ring in place. Also, the total number of pulses in the spectrum below the K_{β} peak were counted and compared in both geometries. With the ring-in geometry there was a less than 1% increase in this region compared to the ring-out geometry; however, the increase was uniform over the region, and the small contribution from scattering did not affect the shape of the background. Thus the presence of the cadmium ring could not account for the appearance of the background.

An additional check on these measurements was made with a ^{207}Bi source used in place of the ^{204}Tl source: Although the peaks observed in region II of the thallium spectra were not present in the bismuth spectra, the differences obtained from comparing ring-in and ring-out geometries were consistent with the thallium source measurements.

These various tests virtually exhausted the possibilities that the peaks in region II were caused by experimental artifacts. Since the peaks were present in the ^{204}Tl spectra, but not in the ^{207}Bi spectra, and since ^{207}Bi decays by electron capture only, the possibility of a physical process

arising out of the beta decay mode in ^{204}Tl was explored.

Of the various higher order processes in beta decay, auto-ionization could account for the observed phenomena. This process is sometimes referred to as "internal ionization," and is the ejection of an atomic shell electron during nuclear beta decay, resulting in the emission of x rays characteristic of the daughter element. On the basis of recent experimental studies, it has been shown that the internal ionization accompanying beta decay can be attributed to the sudden change in nuclear charge during the decay, which causes simultaneous emission of a beta particle, a neutrino, and an orbital electron. This mechanism is often referred to as "electron shake-off."[13-16,18]

There is another possible mechanism by which nuclear beta decay can give rise to the ejection of bround orbital electrons: the direct collision of beta particles with orbital electrons. However, the present available data indicate that this mechanism plays a negligible role except for decays having an extremely low endpoint energy.[13,14,17,18]

In the past few years a number of measurements have been made on the K-shell auto-ionization in the beta decay of ^{204}Tl.[17,19,20] In the present experiment, the value of P_K, the K shell autoionization probability, could not be determined in a straightforward way since the Pb $K\alpha_2$ x-ray peak (Fig. 20) contained a large background contribution from the steeply sloped, high energy tail of the Hg $K\alpha_1$ x-ray peak. It was

observed, however, that channels 29 to 32 of the Pb K_{α_1} peak were not affected by this background, nor by the low energy tail of the Hg K_{β_1} x-ray peak. This can be seen from a comparison of Fig. 20 to Fig. 2 of the System Coincidence Efficiency section, where it is clear that the shapes of those protions of the Pb K_{α_1} x-ray peaks appearing in channels 29 to 32 are the same in both spectra. Thus by normalizing the true shapes of the Pb K_{α} x rays obtained from the electron capture decay of ^{207}Bi (Fig. 2) to the intensities of these channels in Fig. 20, it was possible to separate the Pb K_{α} x rays in Fig. 20 from background, and determine the partial Pb K_{α_1}, Pb K_{α_2} x-ray components. This decomposition is shown in Fig. 21.

The counting rate for these x rays is given by

$$R_{Pb\,K_{\alpha}} = P_k N^0_{\beta^-} \omega_K \frac{\alpha_{K_{\alpha}}}{\alpha_K} \epsilon^{GeLi}_{Pb\,K_{\alpha}}$$

where ω_K is the K-shell fluorescence yield in lead, $\alpha_{K_{\alpha}}/\alpha_K$ is the ratio for transition probabilities of the Pb K_{α} to Pb K x rays, and $\epsilon^{GeLi}_{Pb K_{\alpha}}$ is the Ge(Li) detector efficiency for Pb K_{α} x rays. The quantity $N^0_{\beta^-}$ is the beta decay rate of the source, and is related to the Hg K x-ray emission rate, $I_{Hg K_x}$, of the daughter atom by

$$N^0_{\beta^-} = I_{Hg K_x} (\epsilon_K/\beta^-)^{-1} (\omega_K)^{-1}$$

where ε_K / β^- is the K-catpure-to-β^- branching ratio, and ω_K is the K shell fluorescence yield in mercury. There have been several measurements of this ratio, and they differ by about 5%, which is about the same as the variation in the measured values of P_K. The value 0.01525 ± 0.0002 from Leutz and Ziegler [21] was considered to be most suitable for the present calculations, since the Q-value of the electron capture transition that they deduce from their measurements was in best agreement with the present measured value. In addition, their error in ε_K / β^- was the lowest of those measured. Using this value the result

$$P_K = (1.0 \pm .08) \times 10^{-4}$$

was obtained. It is interesting to note that using the value 0.0159 ± 0.00036 from P. Christmas,[22] which is the highest, we obtain

$$P_K = (1.04 \pm .09) \times 10^{-4} .$$

The measured values of P_K in ^{204}Tl obtained from the present work is in good agreement with the experimental values of $(1.0 \pm .1) \times 10^{-4}$ reported by Howard, Seykora, and Waltner,[17] and $(1.06 \pm .03) \times 10^{-4}$ obtained by B.P. Pathak.[19]

As a result of this analysis, it is clear that the peaks observed in region II are the Pb $K\alpha$ x rays resulting from auto-ionization in the beta decay of ^{204}Tl.

The appearance of these peaks in the coincidence spectra were somewhat surprising, since one would expect suppression

of the auto-ionization effect in the coincidence data. Alternatively, their presence in the coincidence data could not be explained on the basis of any previously observed phenomena. These peaks appear along with the Hg K x rays in coincidence with the bremsstrahlung photons, but are somewhat weaker in intensity than the Hg K x rays. Since a fairly complicated geometry was used in the experiment, various changes were tried on the geometry to study their effects on the coincidence data. It became apparent that the only change which significantly affected the peaks in region II was a change in beta absorber. Further tests showed that the intensity of these peaks was proportional to the atomic number of the absorber used.

At the suggestion of Prof. H. Lancman, a mechanism was proposed for these observations, which to the knowledge of these authors have never been previously reported. One can imagine beta decay accompanied by both auto-ionization and internal bremsstrahlung. These processes separately have been extensively studied in beta decay; however, the simultaneous occurence of these higher order effects has not been observed. On purely simplisitic grounds, one would expect this "new" process to be higher in order than either auto-ionization or internal bremsstrahlung, and hence too weak to observe in the data. However, the effect is seen in the data, and is moderately strong in comparison to the IB in electron capture data, for the same reason that the DIB has such a high relative intensity; i.e., the branching ratio in ^{204}Tl

strongly favors decay through the beta branch.

In order to check the accuracy of these predictions, it was necessary to separate out of the data that portion of the effect which was due to the production of external bremsstrahlung. This occurs when the beta particle or the ionized electron in the autoionization process interacts with the nucleus of an atom other than its own, and an external bremsstrahlung photon is produced. The system apparatus could not distinguish between the external bremsstrahlung (EB) and internal bremsstrahlung (IB) which occur in coincidence with the auto-ionization Pb K x rays, and thus the data will include (EB + IB)—Pb K x-ray photon coincidences. Since it was necessary to sandwich the source between plates of beryllium to prevent the betas from reaching the detectors, the part of the data which was due to external bremsstrahlung could not be eliminated; however, its contribution to the spectrum was accounted for by placing filters of materials having different atomic numbers between the detectors and source. Since the intensity of the external bremsstrahlung produced by electrons irradiating a thick target is proportional to the atomic number of the target, the fraction of the data which was due to external bremsstrahlung should be proportional to the atomic number of the filter. Thus by extrapolating the data obtained with filters of different atomic numbers to a filter of atomic number zero, one obtains the data which contain no contribution from EB—Pb K x-ray photon coincidences. The filters used were 320 mg/cm^2 thick foils of bery-

llium (Z=4), aluminum (Z=13), and copper (Z=29).

The coincidence measurements taken with the aluminum and copper absorbers were obtained in 70.55 hour runs, and were repeated with the time spectrum window shifted off the time peak to obtain the random coincidence data. These runs were made with the absorbers positioned on either side of the source in order to reproduce the actual experimental geometry containing the beryllium absorbers. The experimental data (329.6 hrs) obtained to study IB in electron capture was normalized to 70.55 hours, so that data obtained with a beryllium absorber could be included in the analysis.

For each absorber, the coincidence data was taken in the usual 2-parameter format, and the intensities of the Pb $K\alpha$ peaks were determined in the coincidence spectra corresponding to bremsstrahlung channels 9-20. Because the intensities of the Pb $K\alpha$ peaks in the random coincidence spectra were low, and less than 5% of the peak intensities in the corresponding total coincidence spectra, it was possible to include spectra 9 and 10 in the present analysis; this could not be done in the case of the IB accompanying electron capture, due to the high rate of random coincidences of Hg K x rays in spectra 9 and 10.

The background in the Pb $K\alpha$ peaks was determined by the same procedure used to evaluate the background for the Hg $K\alpha$ peaks, i.e., a weighted least-squares routine gave the background in the Pb $K\alpha$ peak channels by fitting a straight line to the background channels in the regions adjacent to

the Hg $K\alpha_2$ and Pb $K\alpha_1$ peaks.

The coincidence spectra were corrected for absorption of the x ray and bremsstrahlung photons in the filters; these corrections were greatest for the absorption of the x rays in the copper filter. The sums of these spectra obtained with the various filters is shown in Figures 22-24. These spectra do not include corrections for the efficiency of the NaI(Tl) detector. The spectrum obtained with the beryllium filter was obtained by adding coincidence spectra 9 and 10 and subtracting spectra 21 to 40 from the spectrum in Fig. 2, and normalizing the resulting spectrum to 70.55 hours.

In order to determine the probability of K-shell autoionization accompanying IB in the energy range 88.8 to 190.6 keV (IB channels 9-20), the coincidence spectra were corrected for the efficiency of the NaI(Tl) detector. The intensities of the Pb $K\alpha_1$ peaks in these spectra were summed, and the totals obtained with the various absorbers are shown as a function of atomic number in Figure 25. It can be seen that the relative error in total intensity obtained with the beryllium absorber is significantly lower than that obtained with either the aluminum or copper absorbers; this was due to the greater data collection time and lower background obtained with the beryllium absorber.

The three points give an excellent fit to a straight line, which was obtained by a weighted least-squares fit to the experimental points. Each point was weighted by $1/\sigma^2$ where σ is the standard deviation. The experimental errors for

the points are indicated. The line has a slope of 70.1 $\pm$ 18.6, and the intensity corresponding to an absorber of atomic number zero is 246.8 $\pm$ 118.3, where the errors are given in one standard deviation. Thus this data suggests the presence of an internal effect whose magnitude is approximately 50% of the total intensity obtained with the beryllium absorber. However, the size of the errors are such that one cannot rule out the possibility that the effect is entirely due to the production of external bremsstrahlung, although this is unlikely.

In determining the corrections applied to the data for photon attenuation in the absorbers, overestimates were made of these quantities. It is difficult to know the size of these corrections forthe absorbers positioned between the source and NaI(Tl) detector, since the external bremsstrahlung could be created at any point within these absorbers. The thickness of filter used in these calculations was the total filter thickness, 320 mg/cm^2, which is the thickness necessary to stop the most energetic beta particles. The beta spectrum of ^{204}Tl is continuous, and only a small fraction of betas is emitted with the maximum energy available for the decay (765 keV). Thus only a small fraction of the betas will require the full filter thickness to be stopped in--this suggests that most of the external bremsstrahlung is produced in the layers of absorber nearest the source, and hence will suffer attenuation by almost the full absorber thickness before reaching the face of the NaI(Tl) detector. As a result, the values of the total intensities obtained with the aluminum

and copper filters are probably somewhat higher than expected, since they are more sensitive to absorber thickness than the beryllium value. Lowering these values would result in raising the intersection of the least-squares line on the intensity axis in Figure 25; hence the value stated for the intercept of the line should be viewed as a lower limit on the experimental value. In any case the uncertainties in corrections due to filter absorption were estimated to have a small effect (less than 7%) on the magnitude of the results.

The corrections for the absorption of photons in the filters on the side of the Ge(Li) detector were not subject to the same uncertainties as above, since the Pb $K\alpha$ x rays detected in the Ge(Li) detector originated in the source and thus traversed the full thickness of absorber. These correction factors were obtained experimentally from singles spectra taken on the Ge(Li) detector.

The intensity of the IB-Autoionization effect was determined from calculations on the Pb $K\alpha_1$ x rays which included channels 28-33. It was decided not to include the lower energy Pb $K\alpha_2$ x rays in the calculations for the following reasons: The excitation of thallium x rays in the source material could contribute to the spectrum in the region bounded by the Hg $K\alpha_1$ and Pb $K\alpha_2$ x rays. In order to reduce the possiblity of producing thallium x rays, a thin source was used, and an examination of the Ge(Li) singles spectrum did not reveal the presence of these peaks. However, the possibility that they contributed to the coincidence spectra could not

unambiguously rejected. Thus by excluding the Pb K_{α_2} peaks from the analysis, this possibility was avoided. The second reason was based on an analysis of the background in the Pb K_{α} x-ray range. Both the upper and lower ranges of region I were used to determine the background contribution to the x-ray channels. The background calculations on the Pb K_{α_1} x rays depended less on the lower range, and hence were a more accurate estimate of background, than the background calculations on the Pb K_{α_2} x rays.

In order to determine the intensity of the IB-Autoionization effect, it is convenient to express it as a fraction of the probability of K-shell autoionization, since the equations for the two quantities are related, and their ratio does not depend on the source strength or the efficiency of the Ge(Li) detector. If $R_{IB\text{-}PbK\alpha_1}$ is the coincidence counting rate between the Pb $K\alpha_1$ x ray and IB photons in the energy range 90-191 keV, and $P_{IB\text{-}K}$ is the probability per beta decay for IB to accompany K-shell autoionization, then

$$R_{IB\text{-}PbK\alpha_1} = P_{IB\text{-}K}\, N^0_{\beta^-}\, W_K\, (\alpha_{K\alpha_1}/\alpha_K)\, \epsilon^{GeLi}_{PbK\alpha}$$

where $N^0_{\beta^-}$ is the beta decay rate of the source; W_K is the K shell fluorescence yield for lead;[23] $\alpha_{K\alpha_1}/\alpha_K$ (24) is the ratio of transition probabilities for the Pb $K\alpha_1$-to- Pb K x-ray transitions; and $\epsilon^{GeLi}_{PbK\alpha}$ is the efficiency of the Ge(Li) detector for Pb $K\alpha$ x rays, corrected for analyzer dead-time and absorption of the x rays in the copper

foil covering the window of the detector. Note that the quantity $R_{IB-Pb\,K\alpha_1}$, corresponding to the value of the least-squares line at $Z=0$, already carries corrections for the efficiency of the NaI(Tl) detector.

Similarly, the singles Pb $K\alpha_1$ x-ray counting rate, $R_{Pb K\alpha_1}$ resulting from K-shell autoionization is given by the expression

$$R_{Pb K\alpha_1} = P_K N^0_{\beta^-} \omega_K \left(\alpha_{K\alpha_1}/\alpha_K\right) \epsilon^{GeLi}_{Pb K\alpha}$$

where P_K is the probability per beta decay for autoionization of a K-shell electron. From these two expressions we obtain:

$$\frac{P_{IB-K}}{P_K} = \frac{R_{IB-Pb K\alpha_1}}{R_{Pb K\alpha_1}} = (5.6 \pm 2.7) \times 10^{-7} \quad .$$

The probability per beta decay, P_{IB-K}, may be obtained using the experimental value of $P_K = (1.04 \pm .09) \times 10^{-4}$. This gives

$$P_{IB-K} = (5.8 \pm 2.8) \times 10^{-8} \quad .$$

Similar calculations were performed to measure the effect in the IB energy intervals 190.6 - 292.4 keV and 292.4 -394.2 keV, corresponding to spectra 21-32 and 33-44, respectively. The sums of these spectra obtained with the various absorbers are shown in Figures 26 and 28, and the intensities of the Pb $K\alpha_1$, peaks extrapolated to an absorber of atomic number zero are shown in Figure 27. It is clear from these results that the magnitude of the effect falls rapidly with increas-

ing energy. Although the data obtained with the copper absorber was not used to estimate the effect in the higher energy range due to large errors in this data, the data obtained with the Be and Al absorbers was sufficient to confirm the conclusion reached.

For the energy interval 190.6 - 292.4 keV, the intercept 89.5 ± 38.7 results in the value

$$\frac{P_{IB-K}}{P_K} = (2.1 \pm 0.9) \times 10^{-4} ,$$

while for the interval 292.4 - 394.2 keV an intercept 12.2 ± 38.3 was obtained, giving the value

$$\frac{P_{IB-K}}{P_K} = (0.3 \pm 0.9) \times 10^{-4} .$$

As a check on experimental consistency, the intensities of the Hg K_α peaks obtained from summing the coincidence spectra were compared in the runs made with the different absorbers. The comparisons were performed over the sums of spectra 11-20. Although the intense background in the data obtained with the aluminum and copper absorbers introduced large errors in determining the difference between foreground and background in the Hg K_α x-ray channels, the results obtained for the three absorbers were consistent.

Finally, region III of the spectra will be considered. As was previously mentioned, region III is characterized by the presence of a weakly defined peak. The center of this peak (channel 60.5) corresponds to the energy of the Pb K_{β_1}

xrays (84.8 keV), and thus the peak in this region is suggestive of the Pb K_{β} x-ray complement to the Pb K_{α} x rays of region II. The intensity of this peak is too low to be determined with confidence; however, its identification as the Pb K_{β_1} x-ray line is important since it demonstrates the presence of the complete K x-ray series of lead in the coincidence data, in support of our argument for the IB-Autoionization effect.

Another possible reason for a peak in this region is the result of a pulse pile-up effect, which can occur in the following manner: It is possible that an Hg L x ray which is in cascade to an Hg K x ray may be simultaneously detected with the K x ray in the Ge(Li) detector. The resulting pulse which is analyzed will appear as the sum of the K and L x-ray pulses. The sum pulses corresponding to the sum of Hg K_{α} and L x-ray pulses will appear as a broad peak in channels $\approx$ 58-63, i.e., region III.

In order to determine which of the above processes was responsible for the peak in region III, a copper foil 80 mg/cm^2 thick was positioned over the beryllium window of the Ge(Li) detector. The attenuation of Hg L x rays in this foil was greater than 99%, whereas the attenuation of the K x rays was only 7%. With the foil in position the intensity of the pile-up peak was reduced by not more than 50%, thus suggesting the presence of the Pb K_{β_1} x-ray line. The elimination of the pile-up effect also prevented the erroneous determination of the Hg K_{α_1} peak intensity resulting from routing Hg K_{α_1} x-ray pulses to the pile-up peak.

REFERENCES - PART III.2.2

1. P. S. Jastram and J. C. Vanderleeden, Phys. Rev. C 1, 1036 (1970).

2. A. Bond and H. Lancman, Phys. Rev. C 6, 2231 (1972).

3. J. E. Thun, W. D. Hamilton, K. Siegbahn, and K. E. Eriksson, Arkiv Fysik 22, 565 (1962).

4. J. K. Knipp and G. E. Uhlenbeck, Physica 3, 415 (1936).

5. F. Bloch, Phys. Rev. 50, 272 (1936).

6. C. S. W. Chang and D. L. Falkoff, Phys. Rev. 76, 365 (1949).

7. B. Persson, Nucl. Phys. 67, 121 (1965).

8. A recent survey of the filed and presented by B. Persson, in "Proceedings of the International Conference on Electron Capture and Higher-Order Processes in Nuclear Decay," Debrecen, Hungary, 15-18 July, 1968, Vol. 2, pp. 142-158.

9. W. Heitler, in "The Quantum Theory of Radiation" (Oxford University Press, London, 1954), 3rd ed., p. 242.

10. R. D. Evans, in "The Atomic Nucleus" (McGraw-Hill Book Co., New York, 1955), Chap. 21.

11. B. Mulligan and R. G. Seyler, Phys. Rev. C 1, 1041 (1970).

12. J. A. Bearden and A. F. Burr, in Handbook of Chemisty and Physics (CRC Press Inc., Cleveland, Ohio), 54th edition, 1973-1974, pp E181-E192.

13. P. Stephas and B. Crasemann, Phys. Rev. 164, 1509 (1967).

14. P. Erman, B. Sigfridsson, T. A. Carlson, and K. Fransson, Nucl. Phys. A112, 117 (1968).

15. H. J. Fishbeck, F. Wagner, F. T. Porter, and M. S. Freedman, Phys. Rev. C 3, 265 (1971).

16. Y. Isozumi and S. Shimizu, Phys. Rev. C 4, 522 (1971).

17. J. M. Howard, E. J. Seykora, and A. W. Waltner, Phys. Rev. A 4, 1740 (1971).

18. A. Bond, O. P. Gupta, and A. Zide, Phys. Rev. C 9, 1529 (1974).

19. B. P. Pathak, Phys. Rev. C 10, 1599 (1974).

20. J. L. Campbell, L. A. McCelles, and J. Law, Can. J. Phys. 49, 3142 (1971).

21. H. Leutz and K. Kiegler, Nucl. Phys. 55, 648 (1964).

22. P. Christmas, Nucl. Phys. 55, 577 (1964).

23. C. M. Lederer, J. M. Hollander, and I. Perlman, in Table of Isotopes (John Wiley and Sons, Inc., New York, 1967), 6th edition.

24. S. I. Salam, in Handbook of Chemistry and Physics (CRC Press, Inc., Cleveland, Ohio), 54th edition, 1973-1974, p. E194.

25. E. L. Feinberg, J. Phys. USSR 4, 423 (1941).

26. E. L. Feinberg, Yad. Fiz. 1, 612 (1965). trans: Sov. J. Nucl. Phys. 1, 438 (1965).

27. J. Law and J. L. Campbell, in Proceedings of the International Conference on Inner Shell Ionization Phenomena, Atlanta, 1972, p. 2110, edited by R. W. Fink, et al. (Georgia Institute of Technology, Atlanta; Emory Univ., Atlanta, Georgia, 1973).

III.3 REDUCTION OF DATA

A computer program was written to compile the data and calculate the IB intensity. The random coincidence spectra were subtracted from the total coincidence spectra--the resulting spectra are shown in Figures 3-17. The spectra were analyzed in bremsstrahlung channels 11-40, corresponding to an energy range 112.7 - 376 keV. The IB was not analyzed below channel 11 because of the very strong contribution of random Hg K x rays in these spectra. The sum of spectra in the energy range 112.7 - 376 keV is shown in Figure 2.

The IB intensity of each spectrum was determined by summing over channels 10-22, corresponding to the range of the Hg K α x rays, and subtracting the background contribution from these channels. The background was obtained by joining regions on either side of the Hg K α x rays with the line of best fit to these regions. Channels 5-9 and 35-39 were used for these regions. These two intervals consisted primarily of DIB, and a justification for their use in the present calculations is included in the discussion of region I of the background. The intensity of the Hg K β x rays could not be determined as accurately as the Hg K α x rays, because the presence of the peak in region III which has been shown to be due to pile-up and Pb K β x rays.

The results of the calculations are presented in Table 1. This gives the total trues (T), randoms (R), and background (B) intensities under the Hg K α x-ray peaks in the paired-up spectra. The resulting IB intensities of the spectra are

listed in the column headed (T-R-B). The statistical errors in these quantities, as well as the partial errors from the various terms, are also included in this table. A plot of the IB intensity vs. spectrum number (IB energy) is given in Figure 18.

In determining the least-squares fits to the background channels, the channels were weighted according to their standard deviations by $1/\sigma^2$. In some channels of the higher-numbered spectra, where $T_{ji} = R_{ji} = 0$ (j=row, i=channel), this resulted in an infinite weighting, since $\sigma_{ji} = \sqrt{T_{ji} + R_{ji}}$. In the evaluation of the parameters of these fits, quantities containing $1/\sigma_{ji}^2$ in summation appear. In order to render these quantities suitable for calculation, a subroutine was written into the program which converted the zero values of σ_{ji} into non-zero values by taking averages over neighboring values of σ_{ji}. This was done by scanning the matrix first along row i, then along column j, until a non-zero value could be generated for σ_{ji}.

In order to determine the effect of the choice of background channels on the results, the background regions used in determining the least-squre fits were varied by shifting these regions through two channels in either direction. The results showed that the change in IB intensity was negligible over this five channel variation in background. In general the slopes of the background lines were very small, as would be expected in view of the slight variation of the DIB in the energy region studied.

DECAY SCHEME OF ^{204}Tl

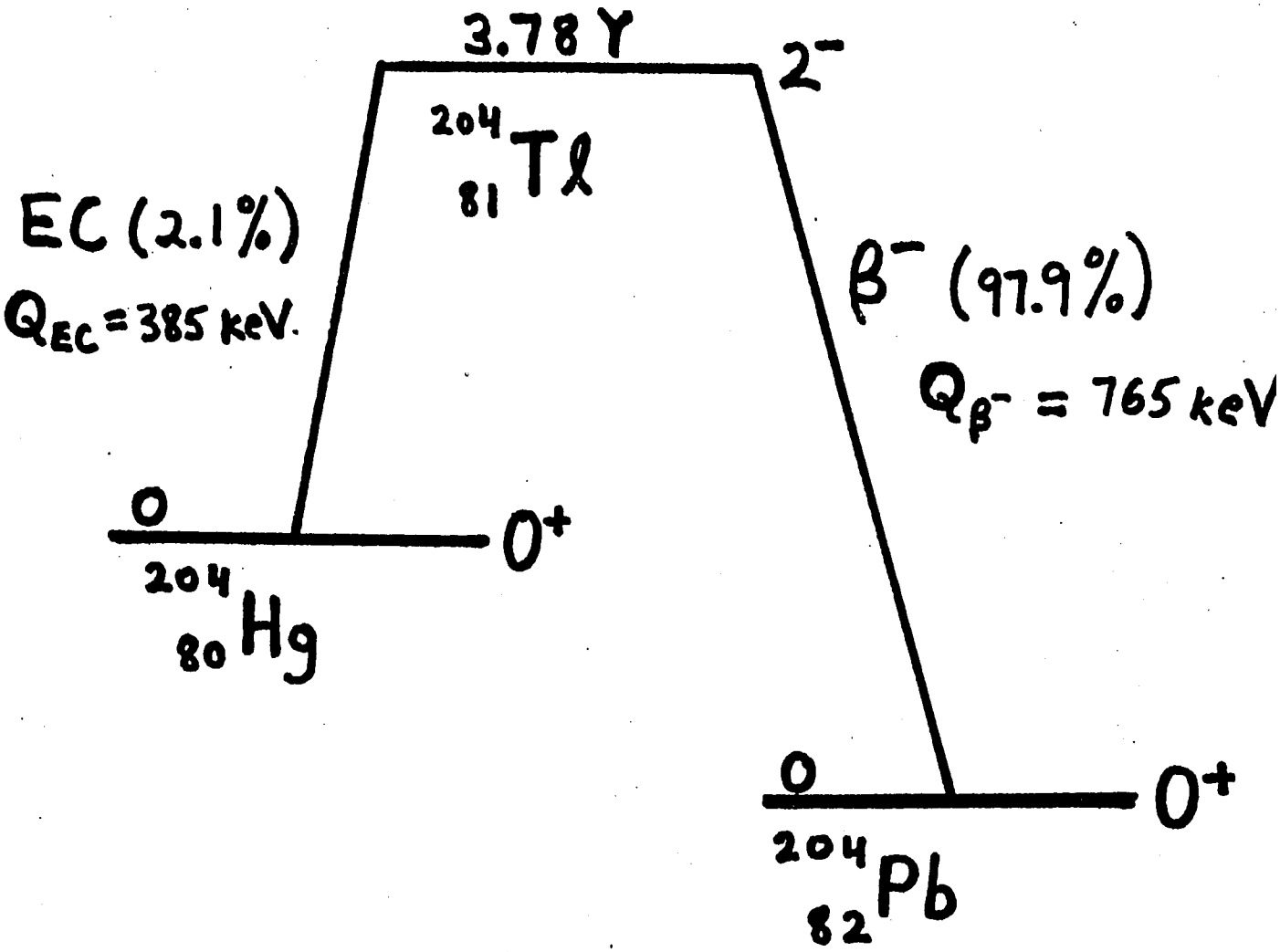

FIG 1

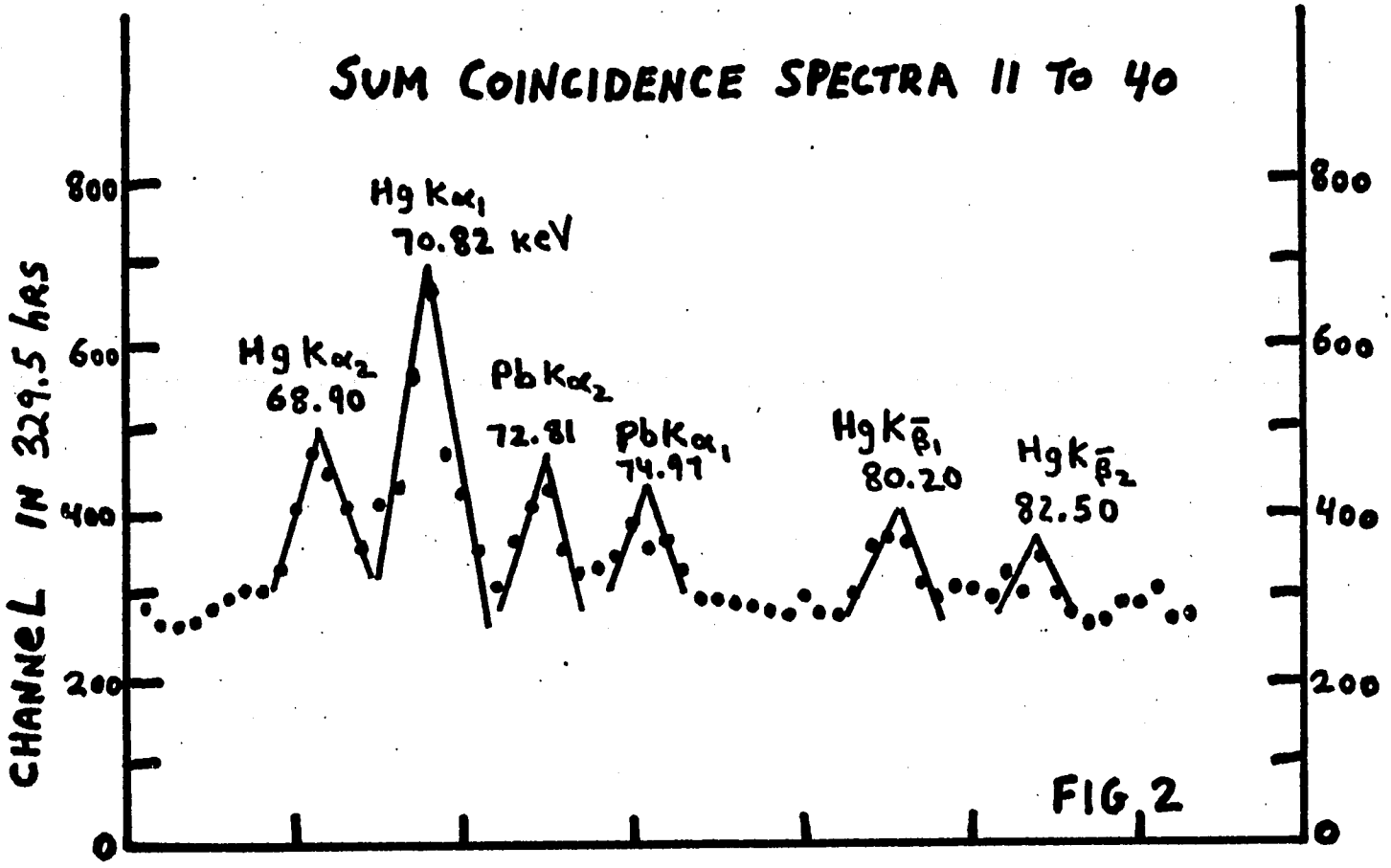
SUM COINCIDENCE SPECTRA 11 TO 40
CHANNEL IN 329.5 hrs
Hg Kα1
70.82 keV
Hg Kα2
68.90
Pb Kα2
72.81
Pb Kα1
74.97
Hg K β̄1
80.20
Hg K β̄2
82.50
800
600
400
200
0

FIG 2

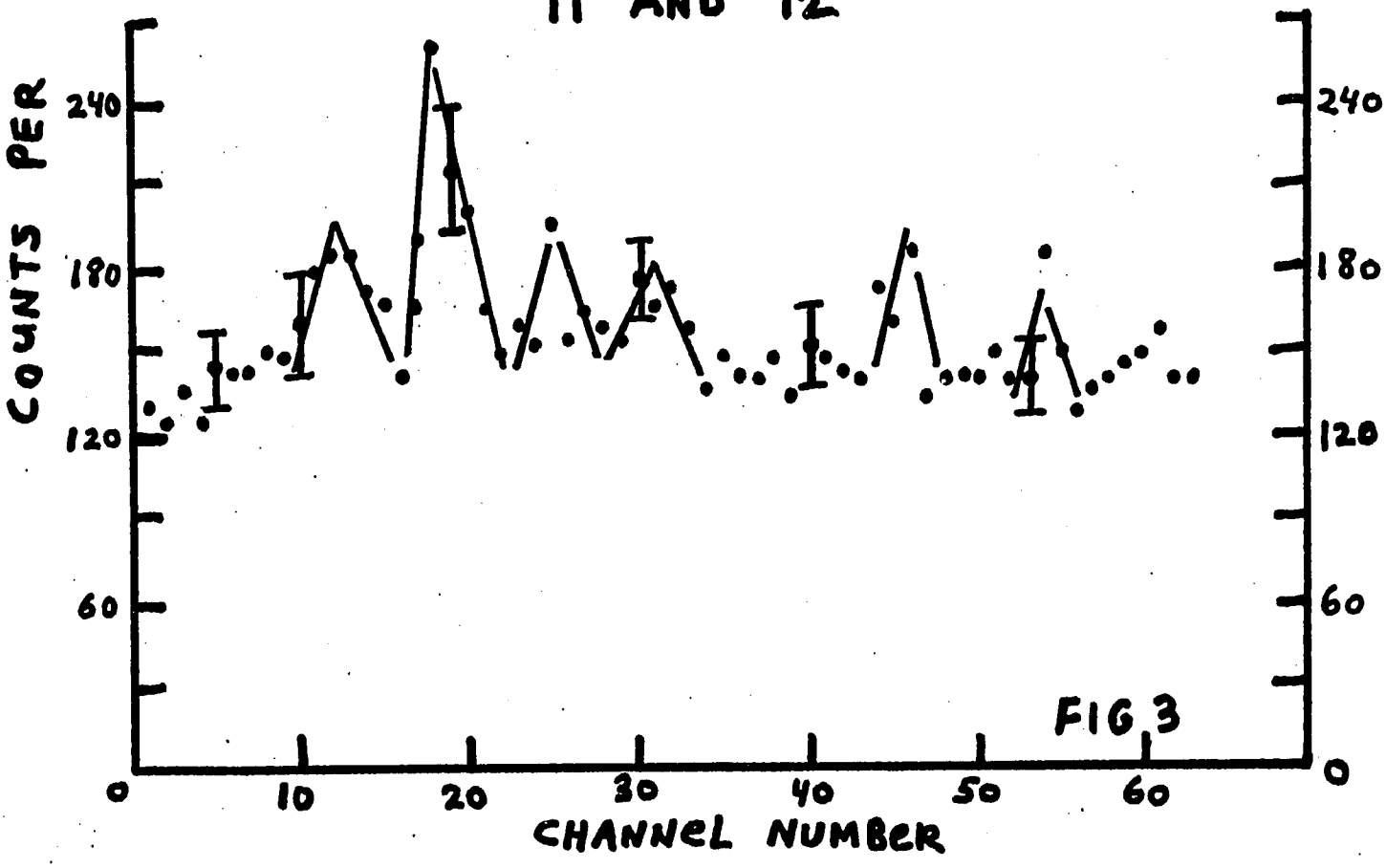
11 AND 12
COUNTS PER
240
180
120
60
0
10
20
30
40
50
60
CHANNEL NUMBER

FIG 3

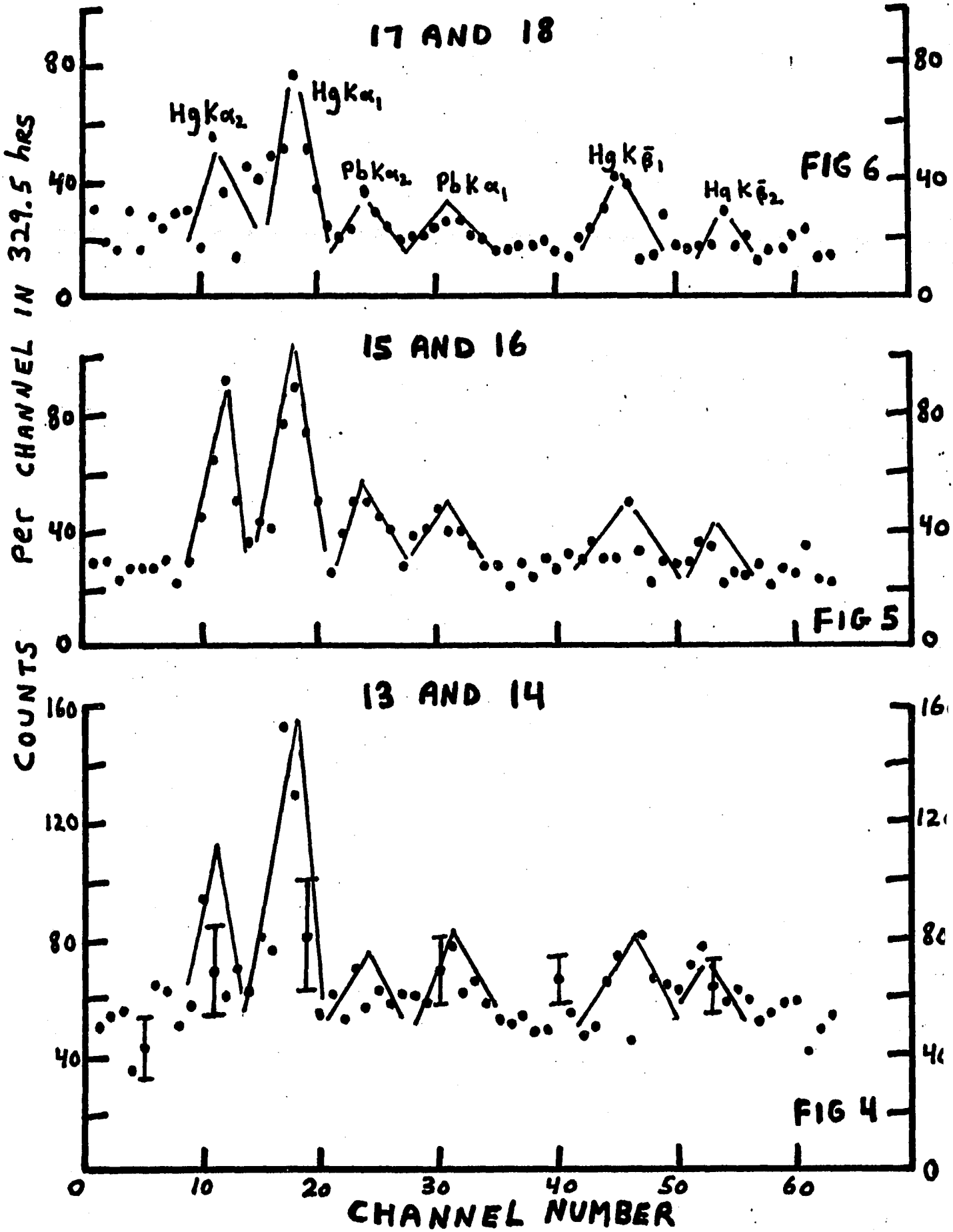
17 AND 18
Hg Kα2
Hg Kα1
Pb Kα2
Pb Kα1
Hg Kβ1
Hg Kβ2
FIG 6
15 AND 16
FIG 5
13 AND 14
FIG 4
COUNTS PER CHANNEL IN 329.5 hrs
CHANNEL NUMBER
0
10
20
30
40
50
60
40
80
120
160

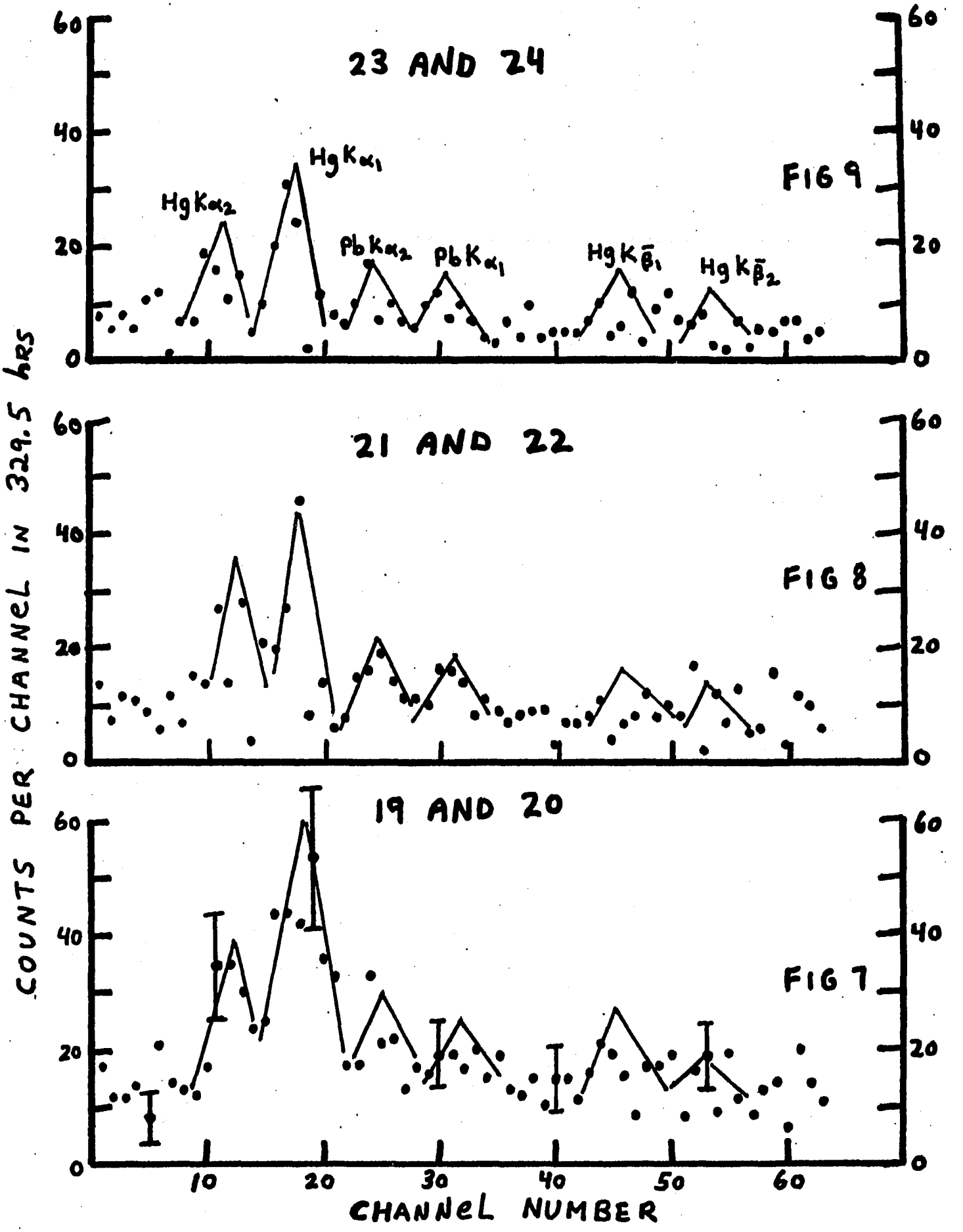
23 AND 24
Hg Kα2
Hg Kα1
Pb Kα2
Pb Kα1
Hg Kβ̄1
Hg Kβ̄2
FIG 9
21 AND 22
FIG 8
19 AND 20
FIG 7
COUNTS PER CHANNEL IN 329.5 HRS
CHANNEL NUMBER
0
20
40
60
10
30
50

29 AND 30

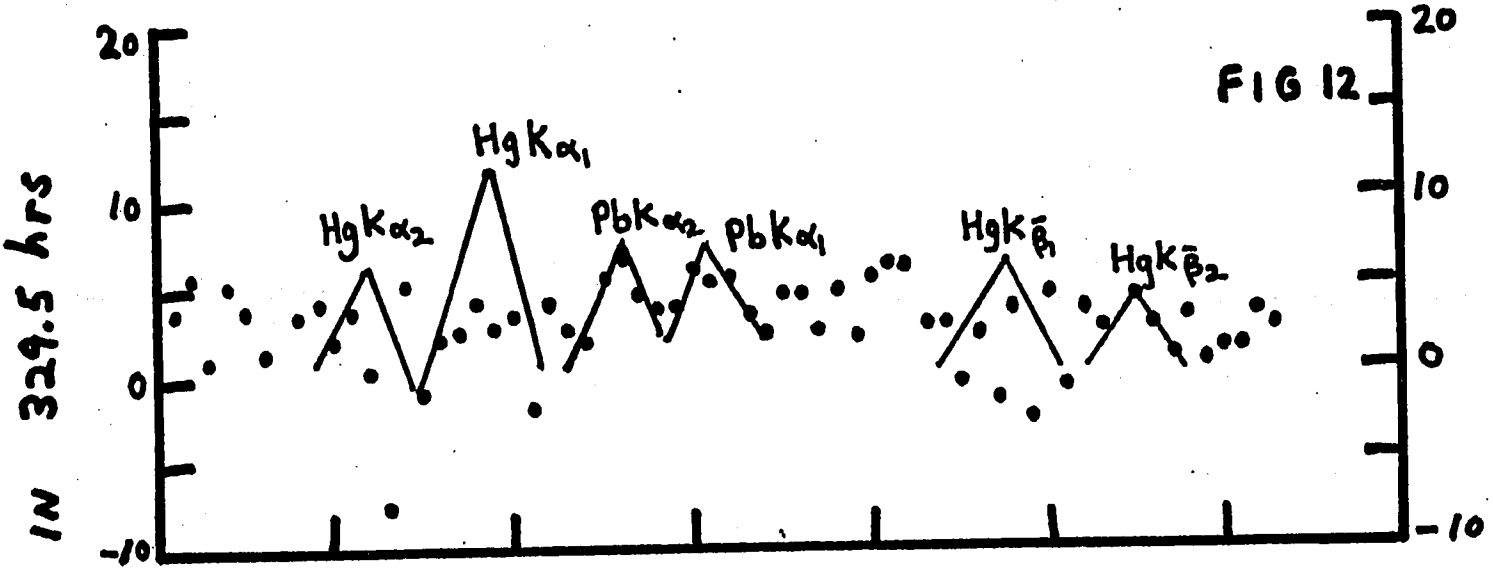

27 AND 28

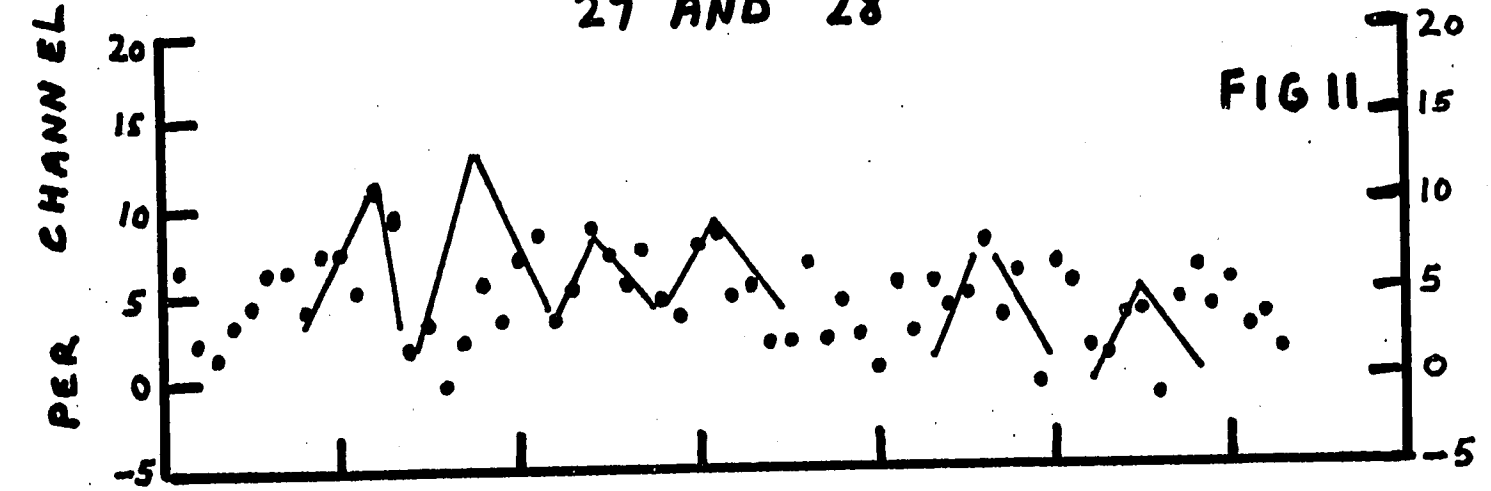

25 AND 26

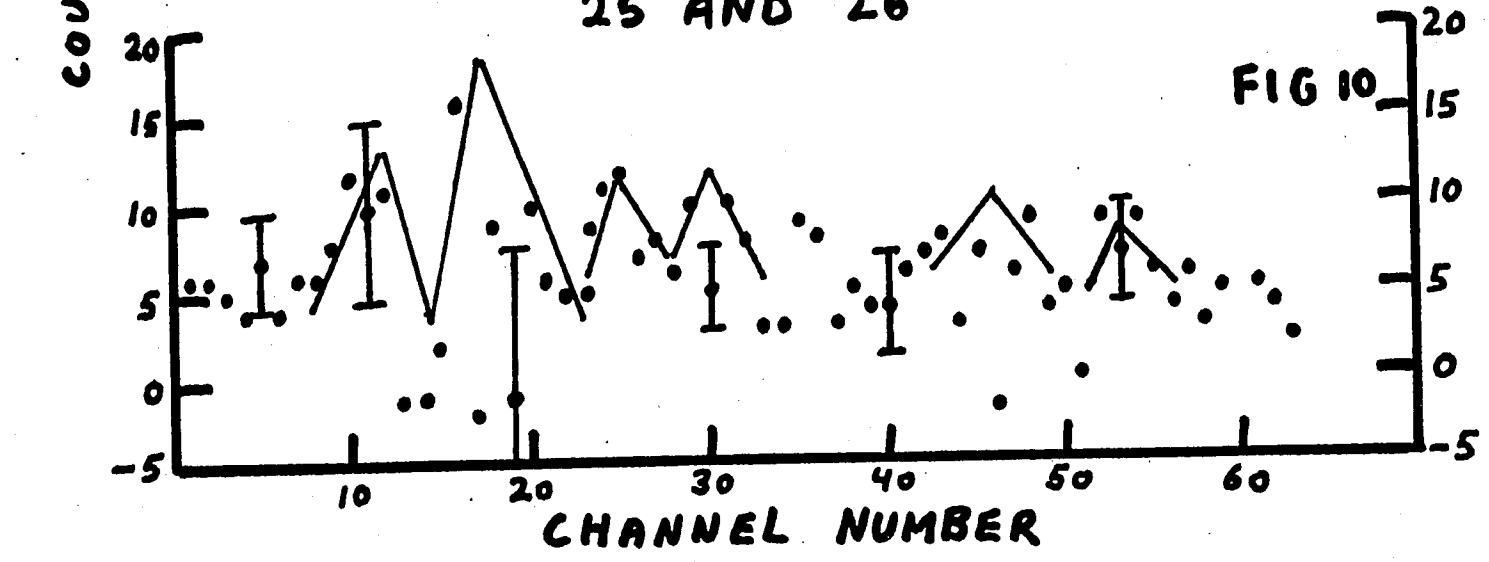

COUNTS PER CHANNEL IN 329.5 hrs

CHANNEL NUMBER

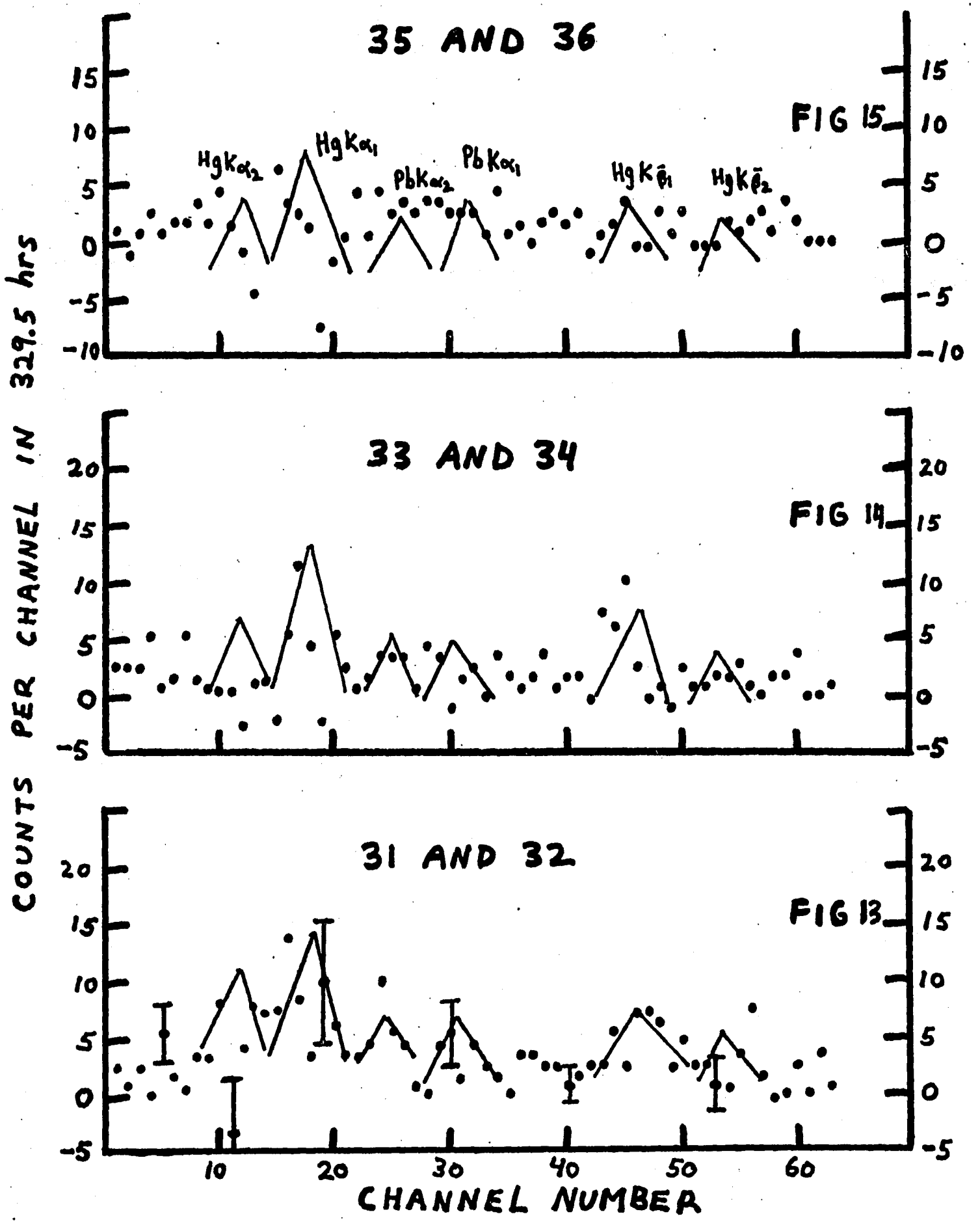
35 AND 36
FIG 15
Hg Kα2
Hg Kα1
Pb Kα2
Pb Kα1
Hg Kβ1
Hg Kβ2
33 AND 34
FIG 14
31 AND 32
FIG 13
COUNTS PER CHANNEL IN 329.5 hrs
CHANNEL NUMBER

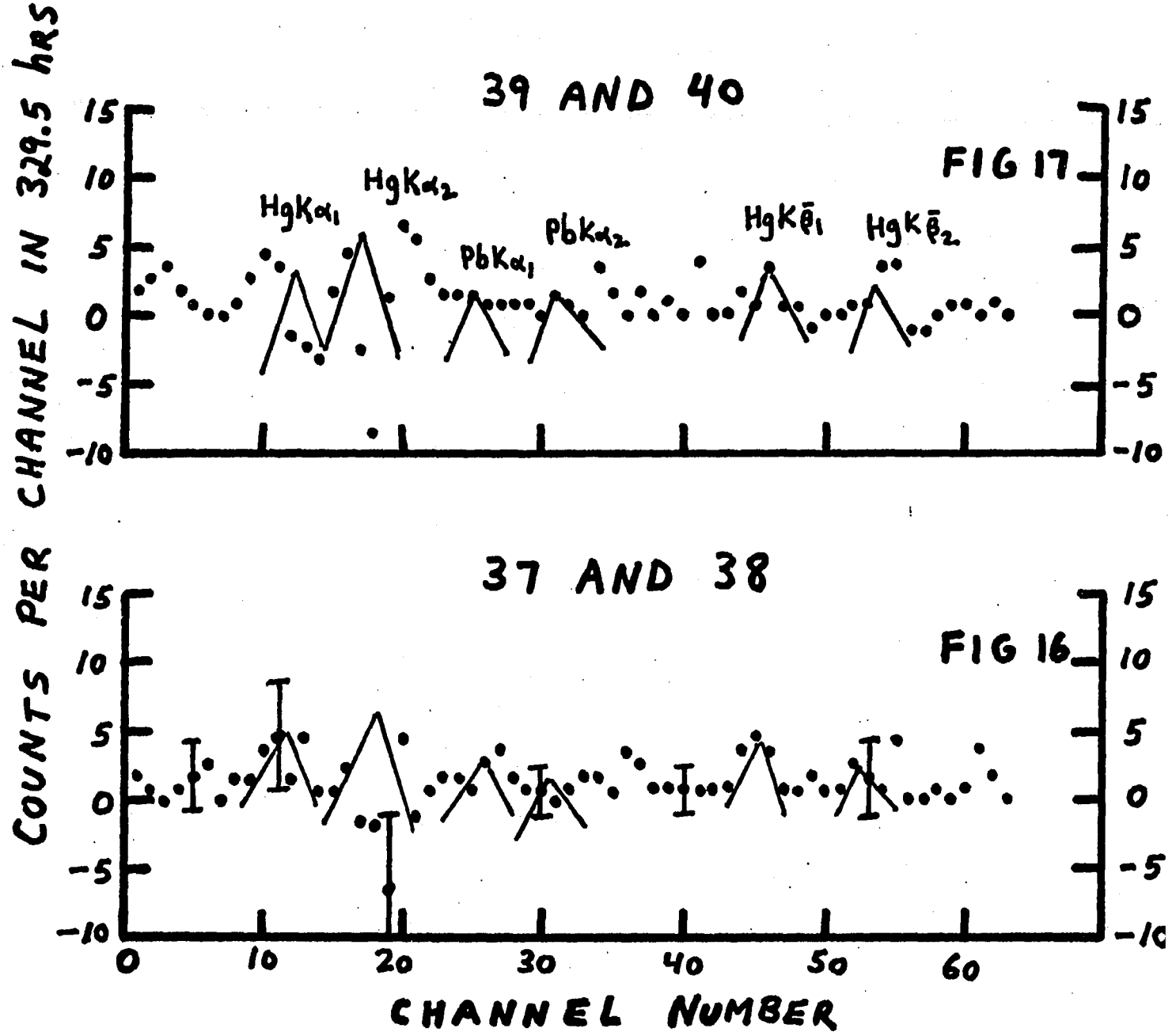
39 AND 40
FIG 17
HgKα1
HgKα2
PbKα1
PbKα2
HgKβ̄1
HgKβ̄2
37 AND 38
FIG 16
COUNTS PER CHANNEL IN 329.5 hrs
CHANNEL NUMBER
15
10
5
0
-5
-10
0
10
20
30
40
50
60

RESULTS OF CALCULATIONS ON $Hg\ K_\alpha$ PEAKS OF COINCIDENCE SPECTRA

CHANNEL NUMBER	T	R	B	T-R-B	σ_T	σ_R	σ_B	σ_{TOTAL}
11+12	3580	1164	1944	472	59.6	34.1	29	74.5
13+14	2159	1110	675	374	46.5	33.3	17.1	59.7
15+16	1654	933	365	356	40.7	30.5	12.5	52.4
17+18	1083	576	251	256	33	24	10.4	42.1
19+20	835	405	198	232	29	20	9.3	36.4
21+22	597	362	94	141	24.5	19	6.4	31.7
23+24	414	239	78	97	20.3	15.5	5.8	26.2
25+26	317	245	58	14	17.8	15.7	5.0	24.3
27+28	236	167	50	19	15.4	13	4.7	20.7
29+30	173	169	31	-27	13.2	13	3.7	18.9
31+32	159	98	27	34	12.6	10	3.4	16.4
33+34	121	97	30	-6	11	9.8	3.6	15.2
35+36	98	87	16	-5	10	9.3	2.6	13.9
37+38	80	68	13	-1	9	8.2	2.4	12.4
39+40	69	56	7	6	8.3	7.5	1.7	11.3
SUM	11575	5776	3837	1962				

TABLE 1

PULSE-HEIGHT DISTRIBUTION OF IB ACCOMPANYING Hg K_α CAPTURE IN ^{204}Tl

FIG 18

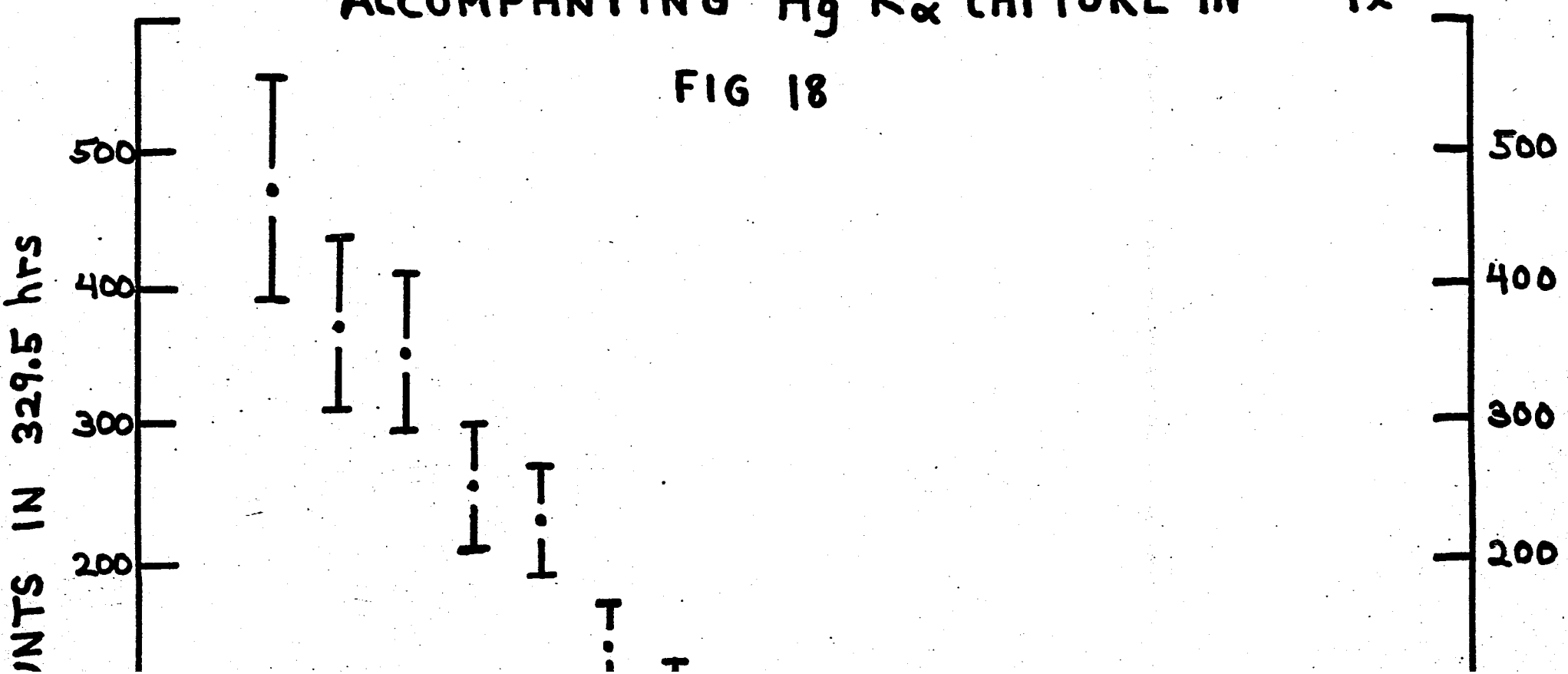

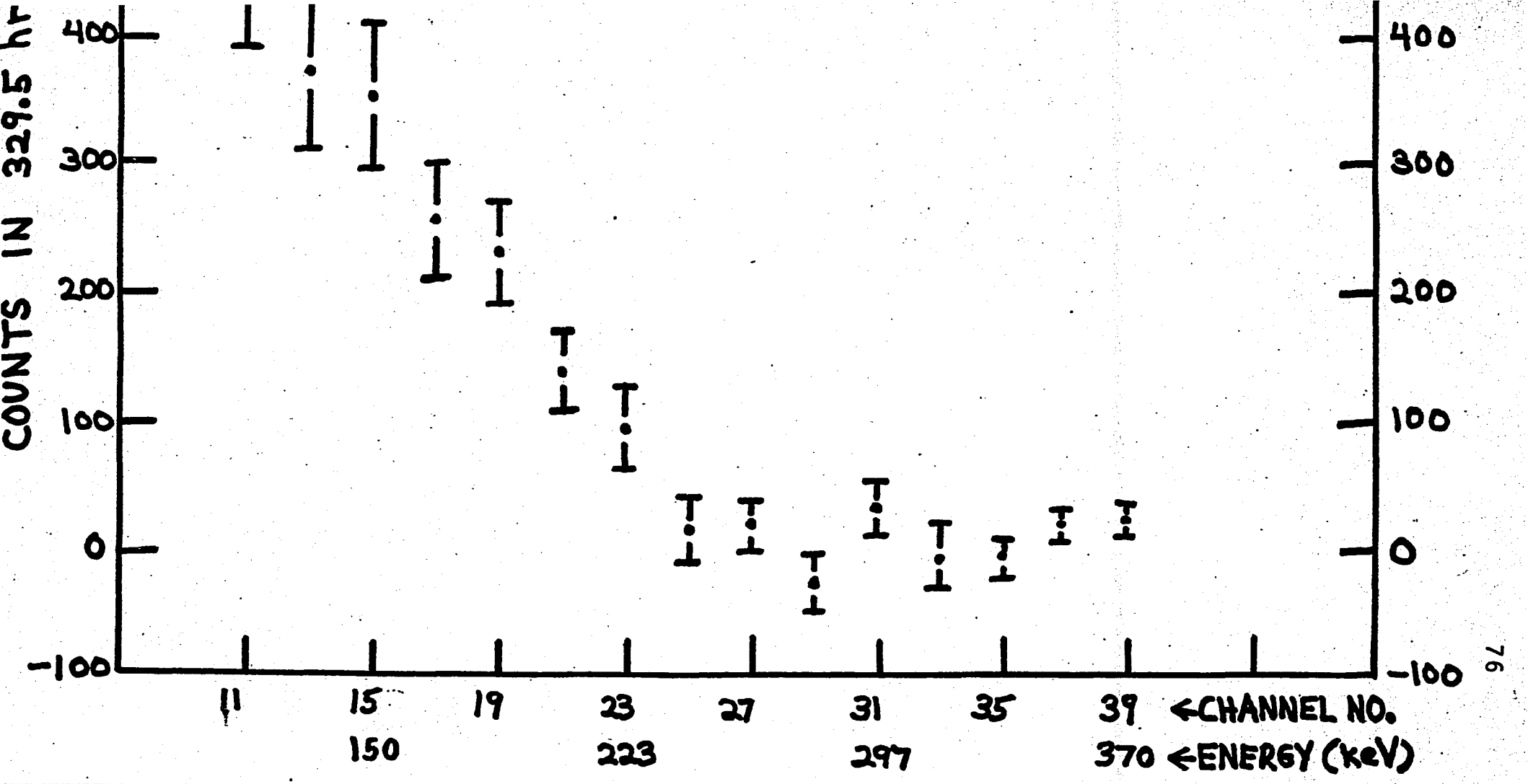
COUNTS IN 329.5 hr
400
300
200
100
0
-100
11
15
19
23
27
31
35
39
←CHANNEL NO.
150
223
297
370
←ENERGY (keV)

SINGLES SPECTRUM OF ^{204}Hg KX RAYS FROM ELECTRON CAPTURE IN ^{204}Tl ON Ge(Li) DETECTOR

FIG 19

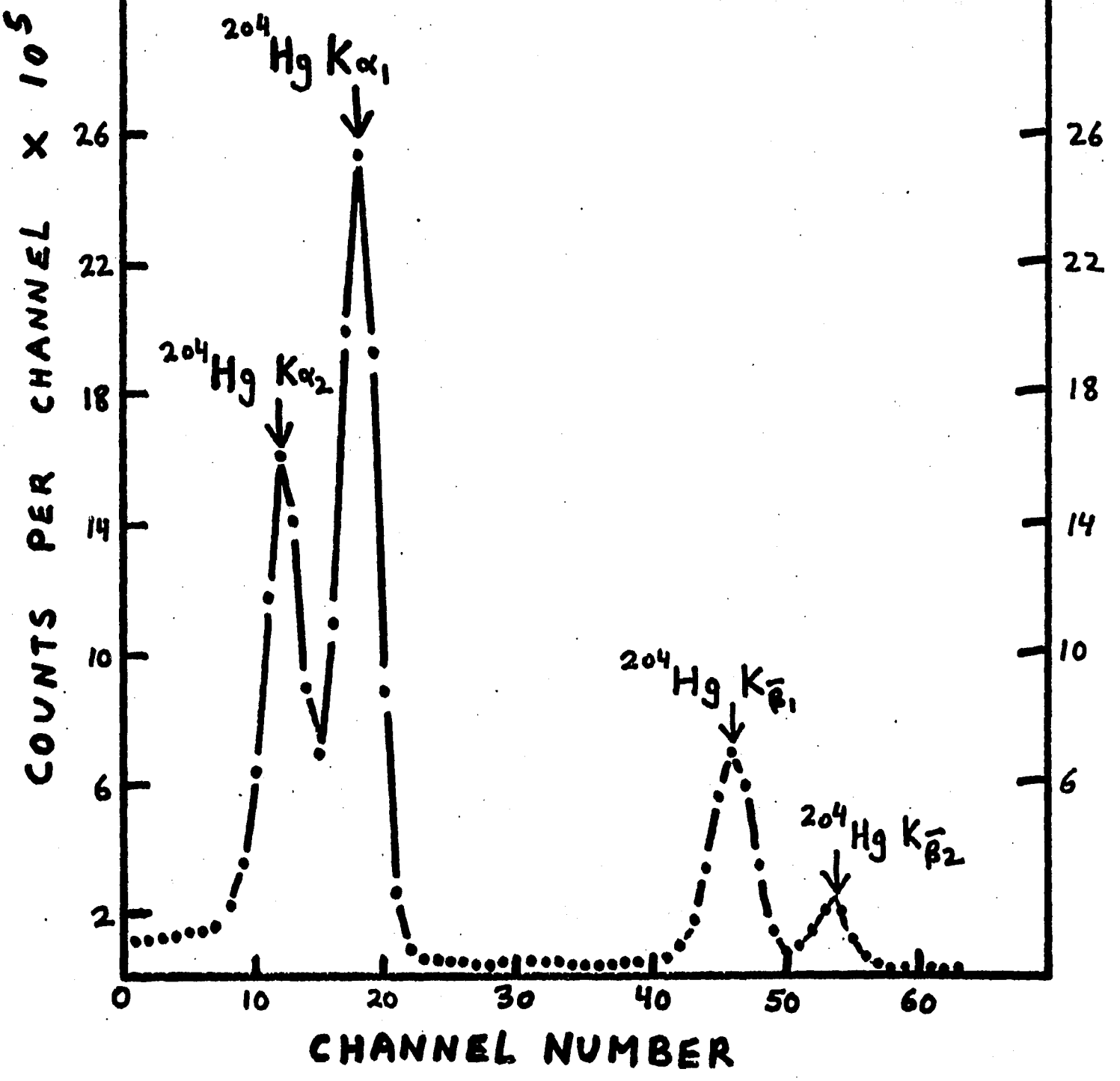

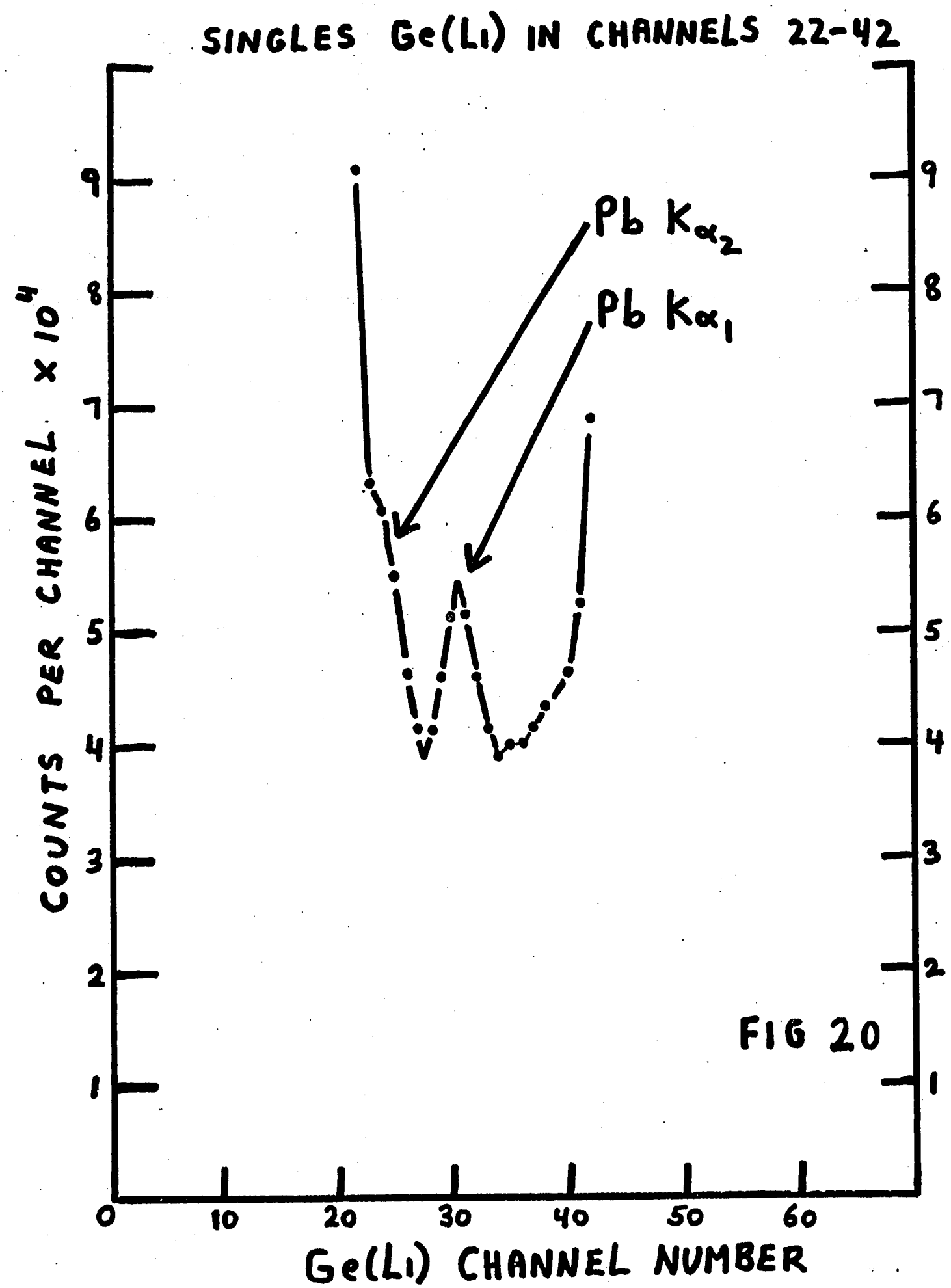
SINGLES Ge(Li) IN CHANNELS 22-42
Pb Kα2
Pb Kα1
COUNTS PER CHANNEL X 10^4
1
2
3
4
5
6
7
8
9
0
10
20
30
40
50
60
Ge(Li) CHANNEL NUMBER

FIG 20

DECOMPOSITION OF CHANNELS 22-32
IN FIGURE 20

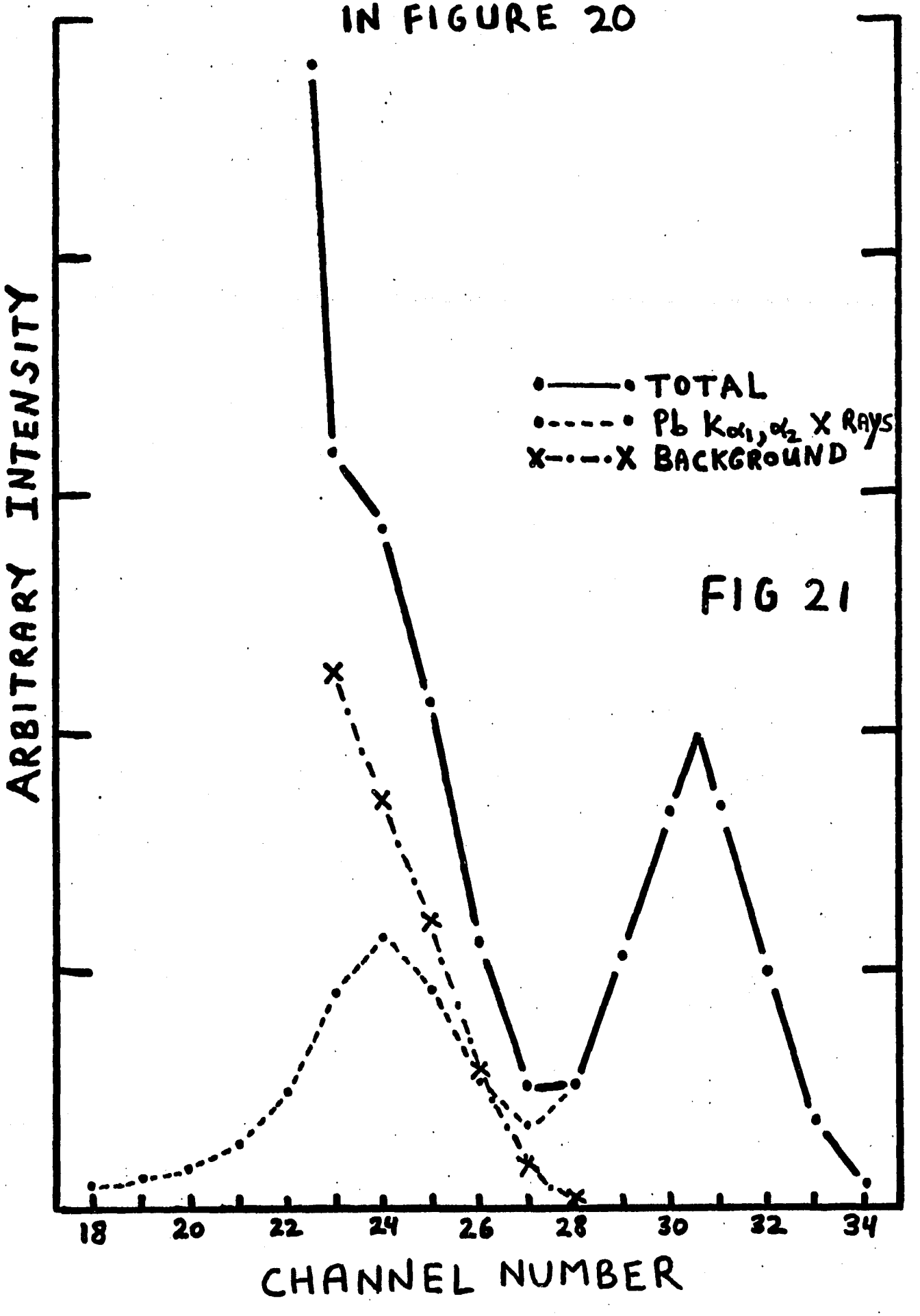

FIG 21

SUM COINCIDENCE SPECTRA FOR VARIOUS ABSORBERS IN CHANNELS 9-20

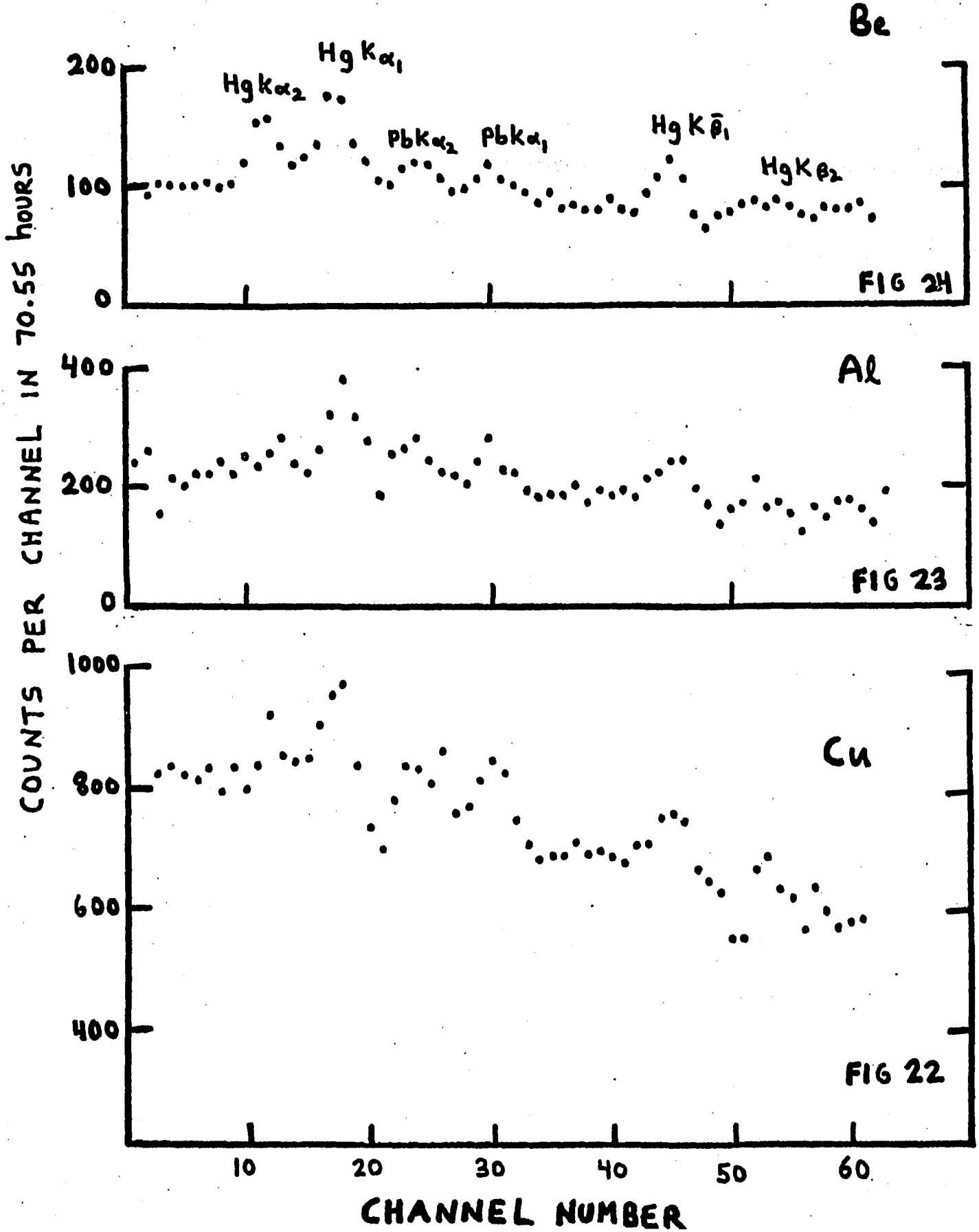

TOTAL INTENSITY OF PB
IB ENERGY RANGE 88.8-190.6
NUMBER OF ABSORBER

FIG 25

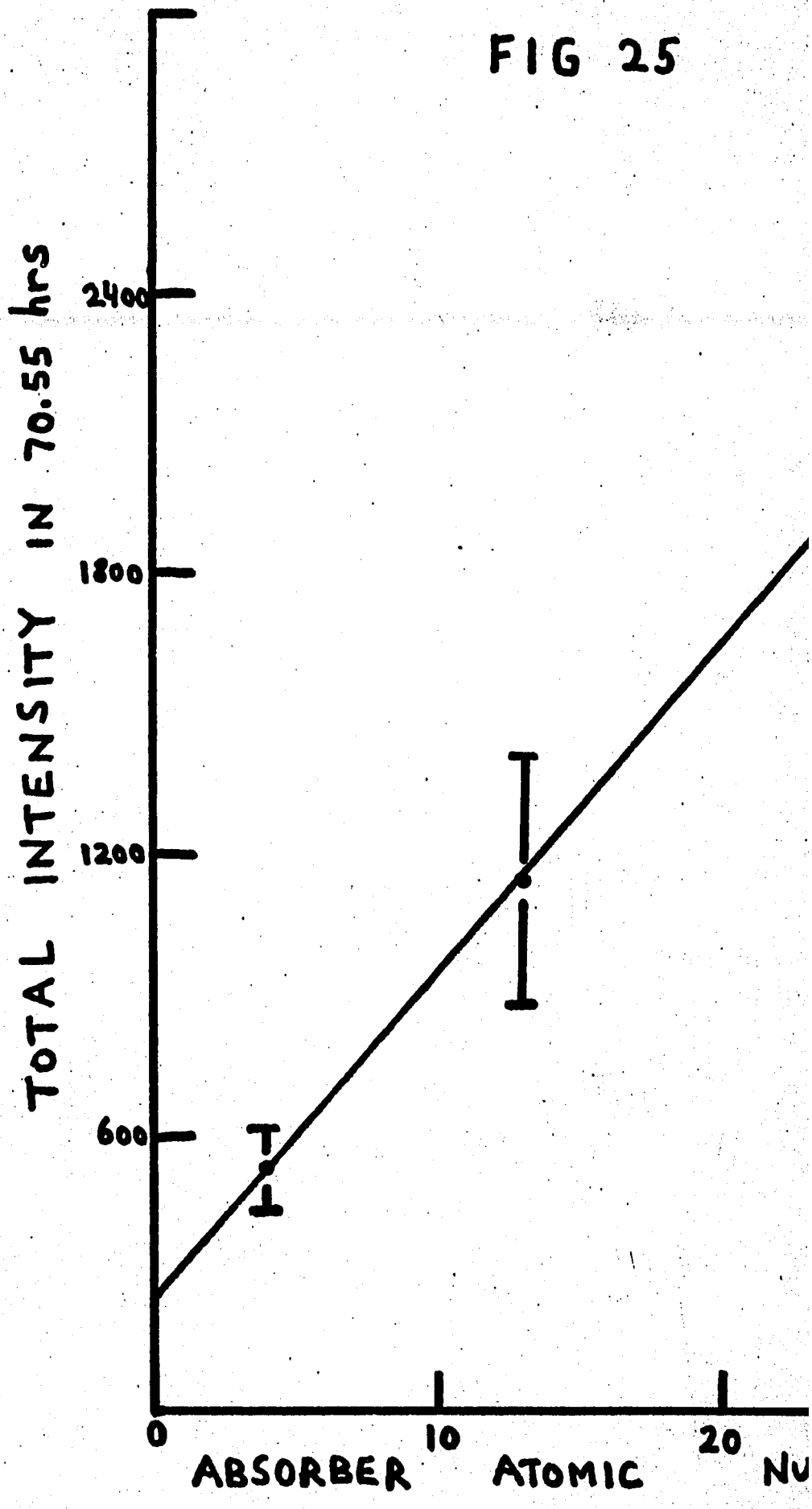

INTENSITY OF Pb $K\alpha_1$ X RAYS IN
ERGY RANGE 88.8-190.6 keV, Vs ATOMIC
ER OF ABSORBER

FIG 25

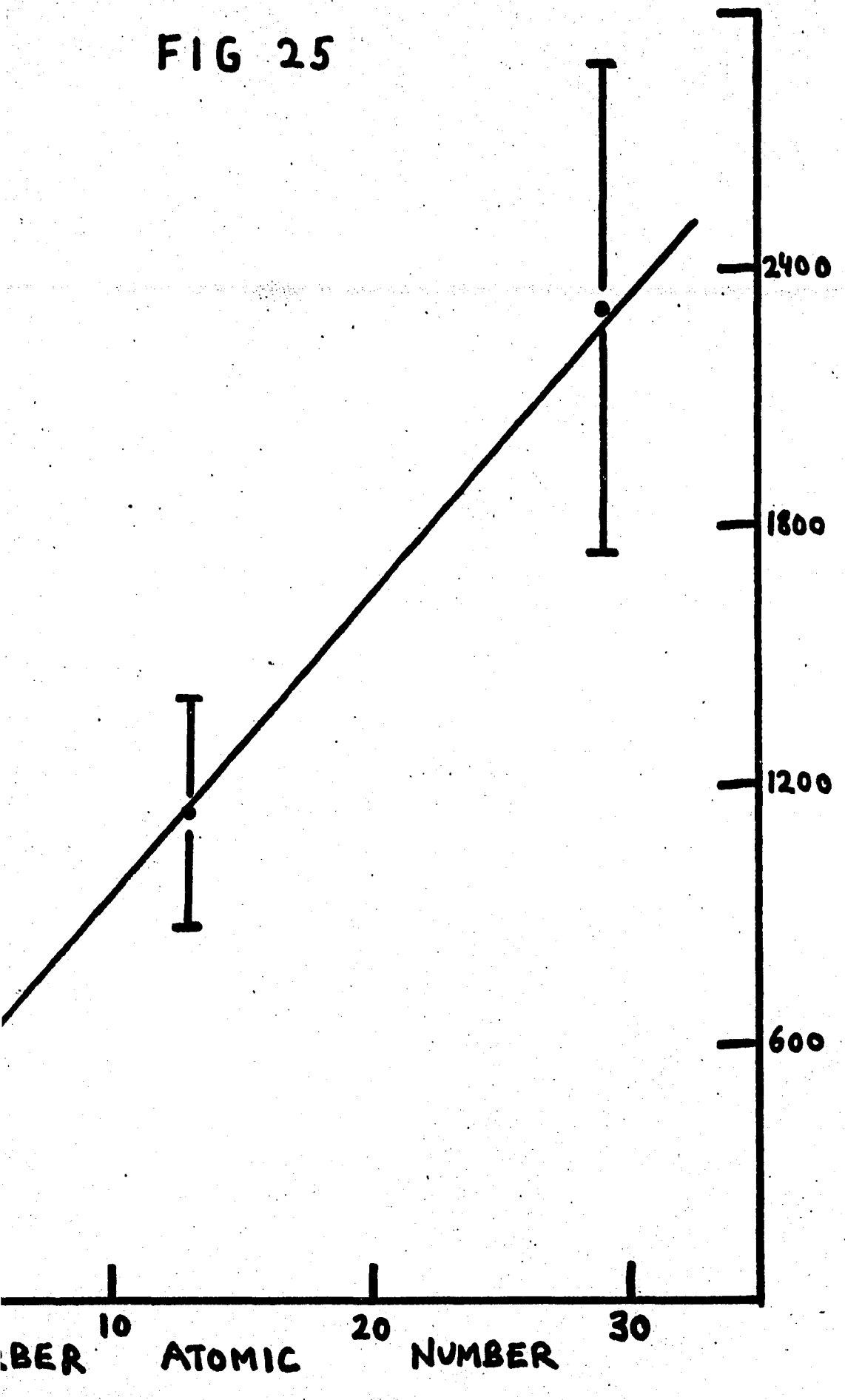

SUM COINCIDENCE SPECTRA FOR VARIOUS ABSORBERS IN CHANNELS 21-32

FIG 26

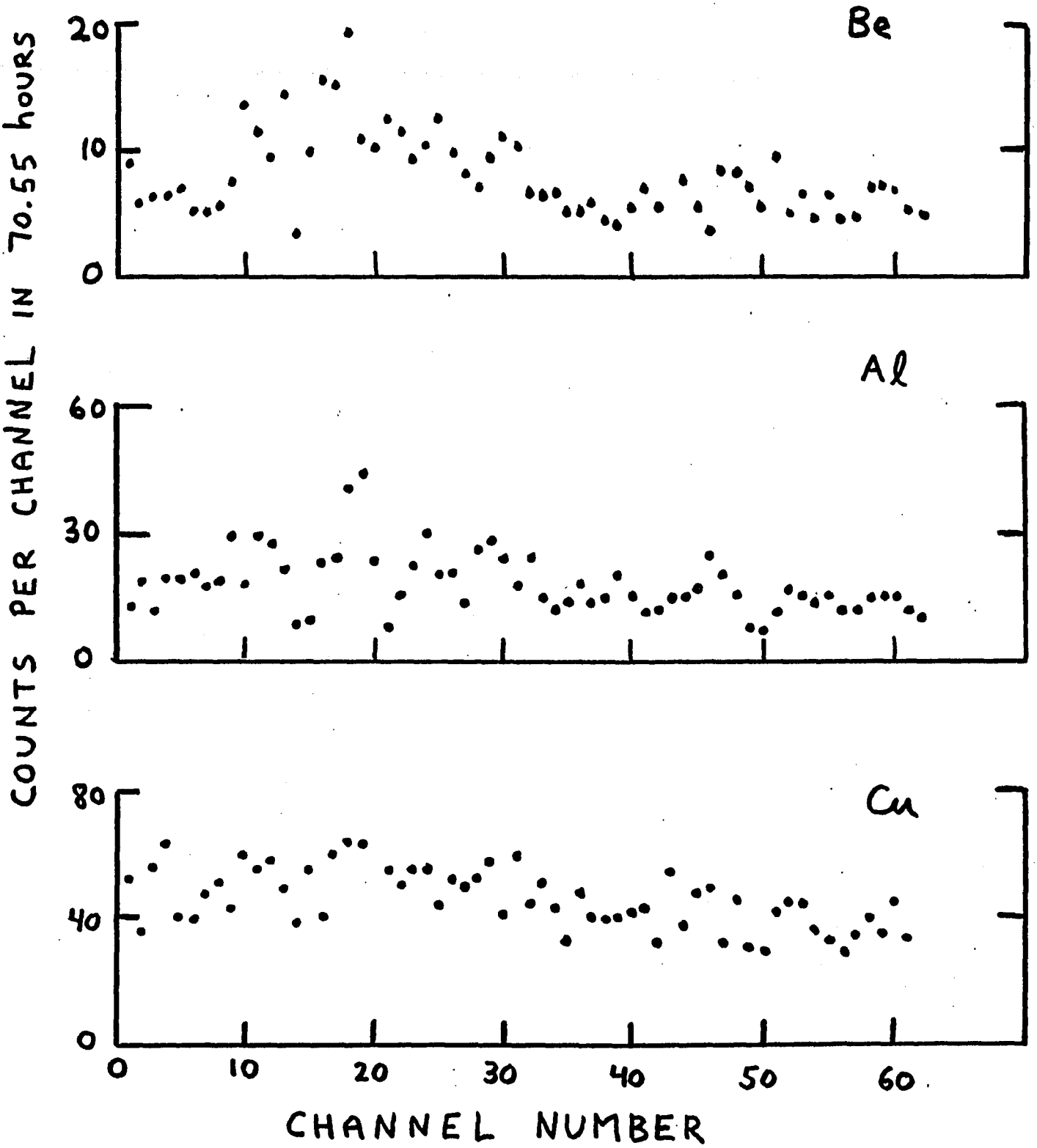

TOTAL INTENSITY OF Pb $K\alpha_1$ X RAYS IN IB ENERGY RANGE 190.6-292.4 keV, Vs ATOMIC NUMBER OF ABSORBER

FIG 27

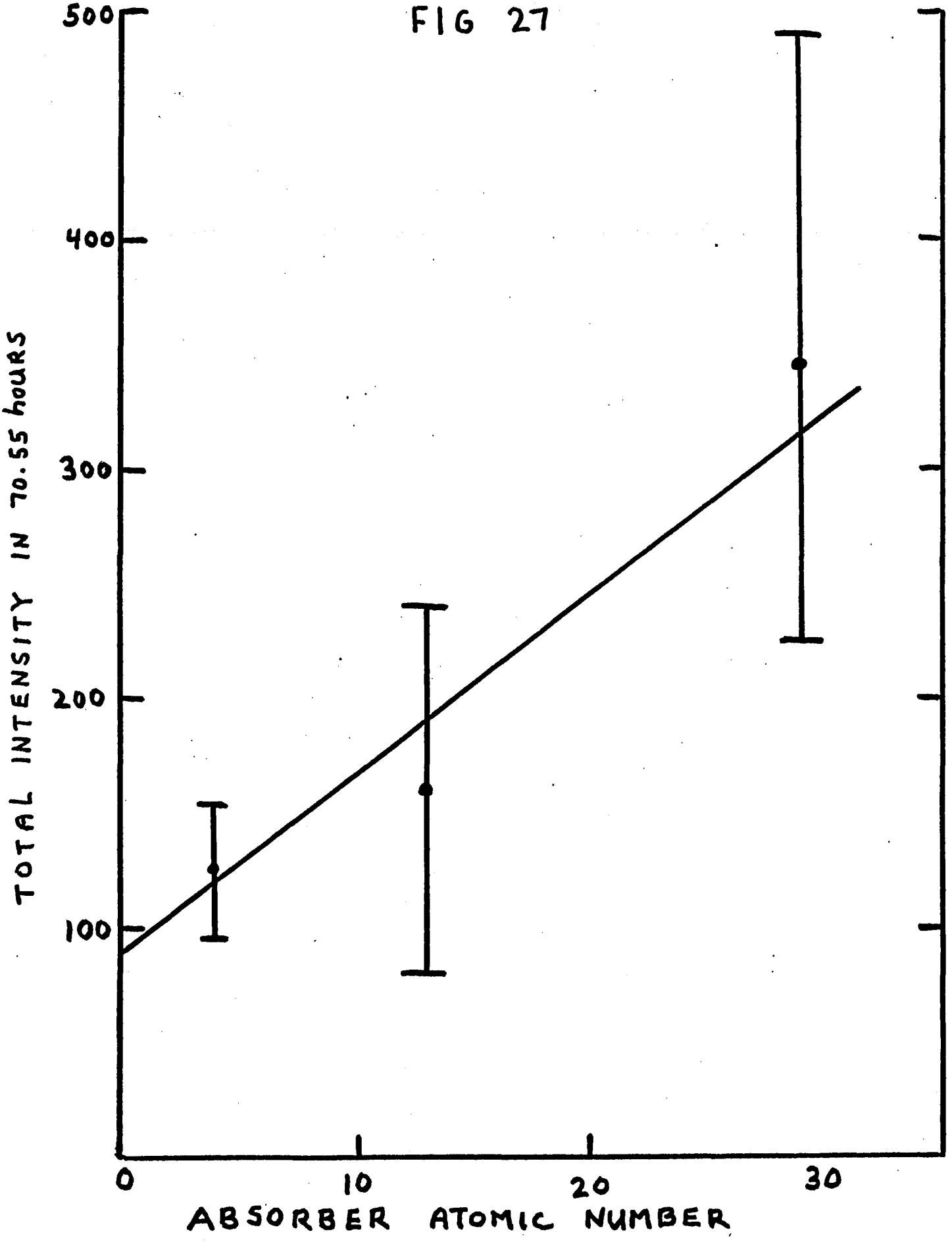

SUM COINCIDENCE SPECTRA FOR VARIOUS ABSORBERS IN CHANNELS 33-44

FIG 28

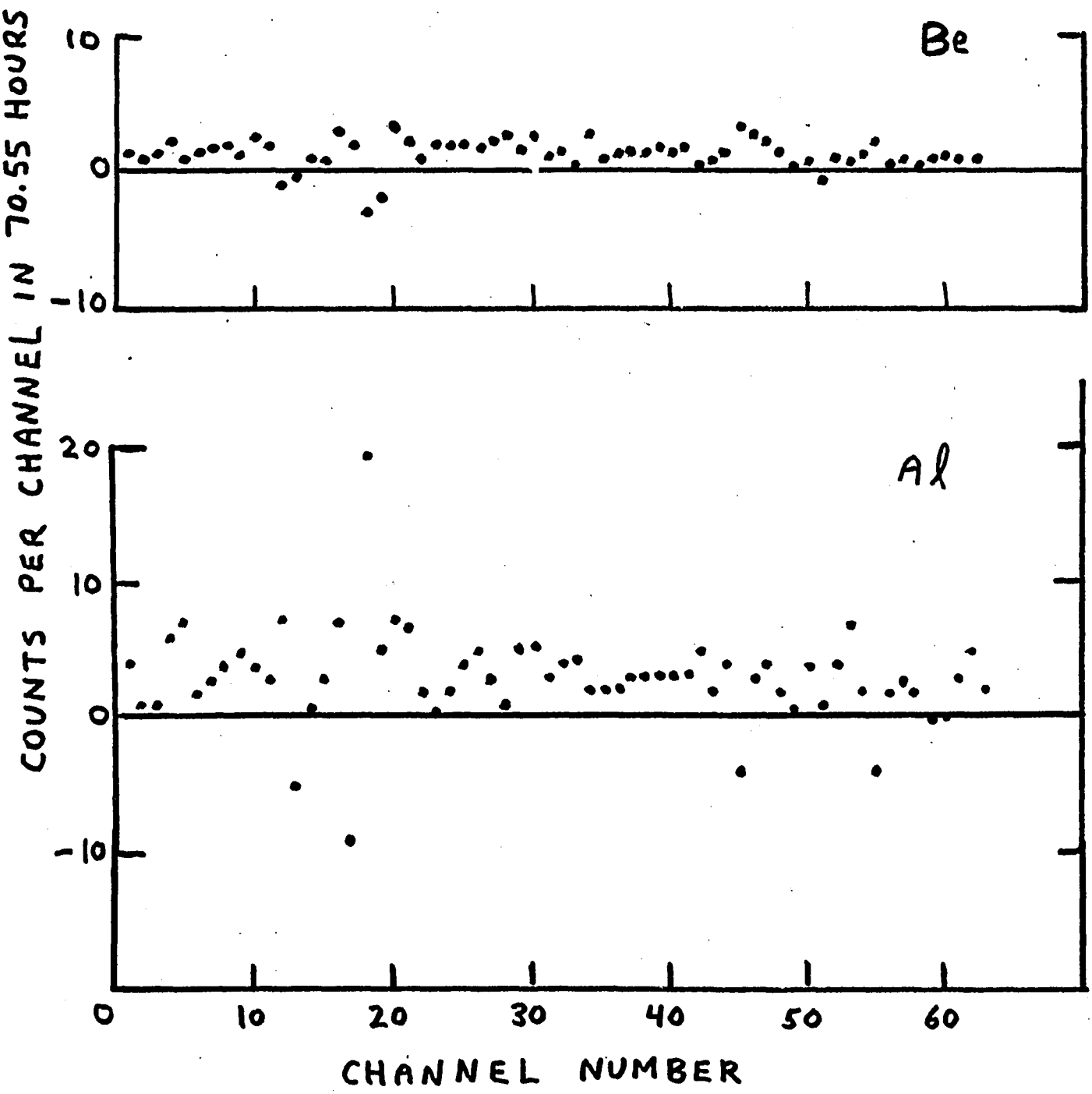

IV. EXPERIMENTAL GEOMETRY AND ELECTRONICS

I. DETECTORS

A 3 x 3-inch NaI(Tl) detector and an x-ray Ge(Li) spectrometer were used to measure the coincident quanta.

The NaI(Tl) detector was used to measure the IB quanta. It consisted of a 3 inch diameter by 3 inch deep thallium activated NaI crystal. The crystal was coupled to an RCA 8575 photomultiplier tube, which was powered by an RCA 1021 photomultiplier base. The optical coupling between crystal and PM cathode was Dow Corning DC 200 fluid. Fast pulses derived from the anode output of the PM tube were used for timing purposes, and slow pulses obtained from the 9^{th} dynode were used for energy information. A variable resistor which controlled tube focus was adjusted for maximum pulse definition.

The detector resolution measured 9.81 keV FWHM at an energy of 87.7 keV.

The detector response was linear over the range of photons studied (15-598 keV). The exact relationship between pulse height and incident photon energy is detailed in the section on Detector Calibrations. The total efficiency of the detector was measured using a calibrated ^{57}Co source, and gave excellent agreement with Heath's calculated value obtained from the total absorption coefficient of NaI. The details of this calculation are included in the section on System Coincidence Efficiency.

An Ortec Low Energy Photon System (LEPS) Ge(Li) detector was used to measure the x-ray photons. The system consisted

of dewar, cryostat, F.E.T. preamplifier, and crystal in the shape of a disc with intrinsic dimensions 16 mm in diameter by 5 mm thick. The preamplifier assembly was located adjacent to the crystal in order to minimize capacitance. The disc was situated approximately 7 mm $\pm$ 1 mm from the 5 mil beryllium window, and was centered with an accuracy of $\pm$ 1 mm on the central axis of the detector. The face of the detector was covered with a plastic endcap, which protected the fragile beryllium window from rupture. In order to improve the detector efficiency, the endcap was carefully removed and replaced with a 1-mm-thick sheet of beryllium. This modification permitted the experimental source to be positioned almost 4 mm closer to the crystal. This resulted in a 51% increase of the x-ray counting rate.

The detector was operated under a bias of -500 volts. This was found to be the optimum voltage setting with respect to pulse resolution and timing considerations. The pre-amp output of the detector was used both for timing and energy discrimination.

The use of the biased amplifier allowed the narrow band of pulses within the Hg K_α --Hg K_β x-ray range to fill the entire 64 channels of the x-ray axis. This instrument was an important part of the experiment since it allowed a careful examination of the spectra.

II. DETECTOR SUPPORTS

A Lucite saddle provided the common mounting for the

detectors. The design of this mount is given in Fig. 1. The saddle was of rigid construction, and assured collinearity of the detector axes.

The dewar of the Ge(Li) detector was supported on a wood base with sponge and spring insultation, which isolated the detector from mechanical vibrations. The saddle was designed to fit snugly to the contours of the cryostat. The NaI(Tl) detector and PM base were easily lowered into and removed from the saddle, and its axis was aligned with the Ge(Li) detector axis through four adjusting screws.

III. SOURCES

The ^{204}Tl and NaI(Tl) detector calibration sources were purchased from New England Nuclear in liquid form. A dryer was used to prepare the samples by simultaneously spreading and heating small amounts of the liquids on thin mylar foils. The samples were spun on a constant speed turntable into a thin evenly distributed layer. An infra-red heat lamp was used for controlled drying. The evaporated sources were sealed in place with a layer of cellophane tape. A special effort was made to use sources which showed a uniform distribution of source material and which were not more than 2 mm in diameter. A thallium source with a strength of $\approx$ 18,300 Hg K x rays—sec^{-1} was used for data collection. This source strength yielded a true-to-random ratio of 2:1, and required a total (trues plus randoms) running time of $\approx$ 600 hours. The calibration sources were roughly of the same intensity.

The thallium source was examined for impurities in the energy range from 65 to 600 keV. The photon spectrum from ^{204}Tl consists principally of mercury x rays superimposed on a continuous bremsstrahlung spectrum. In terms of the source activity an upper limit for the intensity of contaminant gamma rays of 2 X 10^{-7} per ^{204}Tl decay was obtained.

IV. SOURCE SUPPORTS

The sealed sources were centered and glued on 1-mm-thick Lucite washers. These were pressed into larger washers, which fitted the saddle. These source holders and mounts were easily inserted into the saddle between the detectors. A diagram of this assembly is shown in Fig. 2.

The use of light, low-Z material for the source mount and holder served to reduce scattering in the vicinity of the source which would have appeared as pulses on the low energy tail of the photopeak.

V. TIN FILTER AND CADMIUM RING

Because of the design of the Ge(Li) detector, the only position of the detectors which gave a reasonable coincidence counting rate was face to face. This arrangement, along with the modification made on the Ge(Li) detector to reduce the source--Ge(Li) crystal distance (the crystal was approximately 14 mm from the source) resulted in a serious backscattering problem.

The backscattering was primarily due to photons which enter the Ge(Li) detector where they are Compton scattered

through 180 degrees into the NaI(Tl) detector. These events result in pulses which are in true time coincidence, and thus cannot be discriminated against through analysis of the time data. In addition, one can show from the Compton scattering formula that for a primary photon energy of 200 keV, the back-scattered photon carries off 110 keV and the Compton electron is left with 75 keV. Thus these events will appear in the energy regions of interest.

The backscatter appeared as a broad bump over the energy range 100 to 130 keV of the bremsstrahlung spectrum, and as a uniform increase of the background in coincidence spectra numbered 10-13. The two-parameter analysis allowed this effect to be separated from the IB data; however, large errors resulted from this separation, and thus it was desirable to minimize this effect.

A tin collimator and cadmium ring were designed to reduce scattering between the two detectors. The collimator was 14.5 mm thick at its edges, subtended a half-angle of 51 degrees, and contained a 6.5-mm-diameter hole, which the source was centered over. A small tapered cadmium ring was designed to fit over the source in the Lucite source holder, on the side facing the Ge(Li) detector, in order to reduce the possibility that photons scattered from the Ge(Li) detector would pass through the hole in the collimator. The NaI(Tl) detector was positioned at the greatest distance from the collimator which would permit it to view the full solid angle subtended by the collimator. The collimator design is shown in Fig. 1.

It was found that there were three factors in the collimator design which affected the coincidence spectra. The thickness of the filter affected mainly the high energy portion of the backscatter spectrum. Increasing this thickness, however, required increasing the source--NaI(Tl) detector distance which lowered the detector efficiency. The effect of the cone half-angle was seen mainly on the low energy side of the backscatter spectrum, since the tapered section of the filter was more effective attenuating low energy photons than high energy photons. And finally, the intensity of the backscatter peak was proportional to the square of the hole diameter. However, the hole could not be made too small, as scattering from the edge of the hole became significant.

The final filter design was obtained by varying these factors, and represented a compromise between minimizing the backscatter and maximizing the counting rate in the NaI(Tl) detector.

VI. SYSTEM ELECTRONICS AND TIME SPECTRUM

Information on the time difference between the detection of photons emitted simultaneously was determined by the T.A.C. (Time to Amplitude Converter). In general, photons which are emitted in coincidence will give rise to pulses which are separated in time due to geometrical considerations and inherent delays in the system electronics. The T.A.C. (Ortec 437A) is driven by start and stop input pulses, which are derived from Constrant Fraction Timing Discriminators (Ortec 453)

located in either branch of the system. The start pulse initiates a linear ramp voltage, which is interrupted upon arrival of the stop pulse. Thus the ramp pulse, which is the T.A.C. output, has an amplitude proportional to the time delay between the two input pulses. The T.A.C. pulses will show some scatter about a mean value, and the ability of the T.A.C. to distinguish true coincident events from random coincident events is determined by the extent of this scatter. A spectrum of these time pulses for a representative run is shown in Figure 4. It proved advantageous to start the T.A.C. with Ge(Li) pulses, and stop the T.A.C. with NaI(Tl) pulses delayed by 50 ns. This arrangement allowed maximum coincidence counting efficiency.

The FWHM of the time spectrum was $\approx$ 13 ns. The window on the time spectrum (as indicated by the arrows) did not include the full peak, but cut the wings of the peak in order to improve the true-to-random ratio. This was accounted for in the determination of the coincidence efficiency of the system. The contribution of random coincidences in the time peak was determined by shifting the window 200 ns to the flat background portion of the spectrum, which consisted of random coincidence pulses only.

In order to measure the coincident photons within the energy ranges of interest, a slow coincidence system was used. The slow coincidence unit (Ortec 418) generates an output pulse provided two slow logic (0.5 usec wide) input pulses overlap in time. These logic pulses are derived from single-

channel analyzers (Ortec 455) included in both branches of the system, and signify the detection of photons in the desired energy ranges. The coincidence accuracy of the slow system is no better than 1 usec; however, by using the output of the 418 to strobe the T.A.C. output, one is assured of pulses which not only have good timing, but also satisfy the energy restrictions placed on the single-channel analyzers. A block diagram giving the general setup of the electronics is shown in Figure 3, and Figure 4 shows the electronics modules used.

In the final analysis, the accuracy of the system was a matter of fine tuning the electronics, and monitoring it at various places to insure that erroneous data was rejected.

SOURCE - DETECTOR GEOMETRY FIG 1

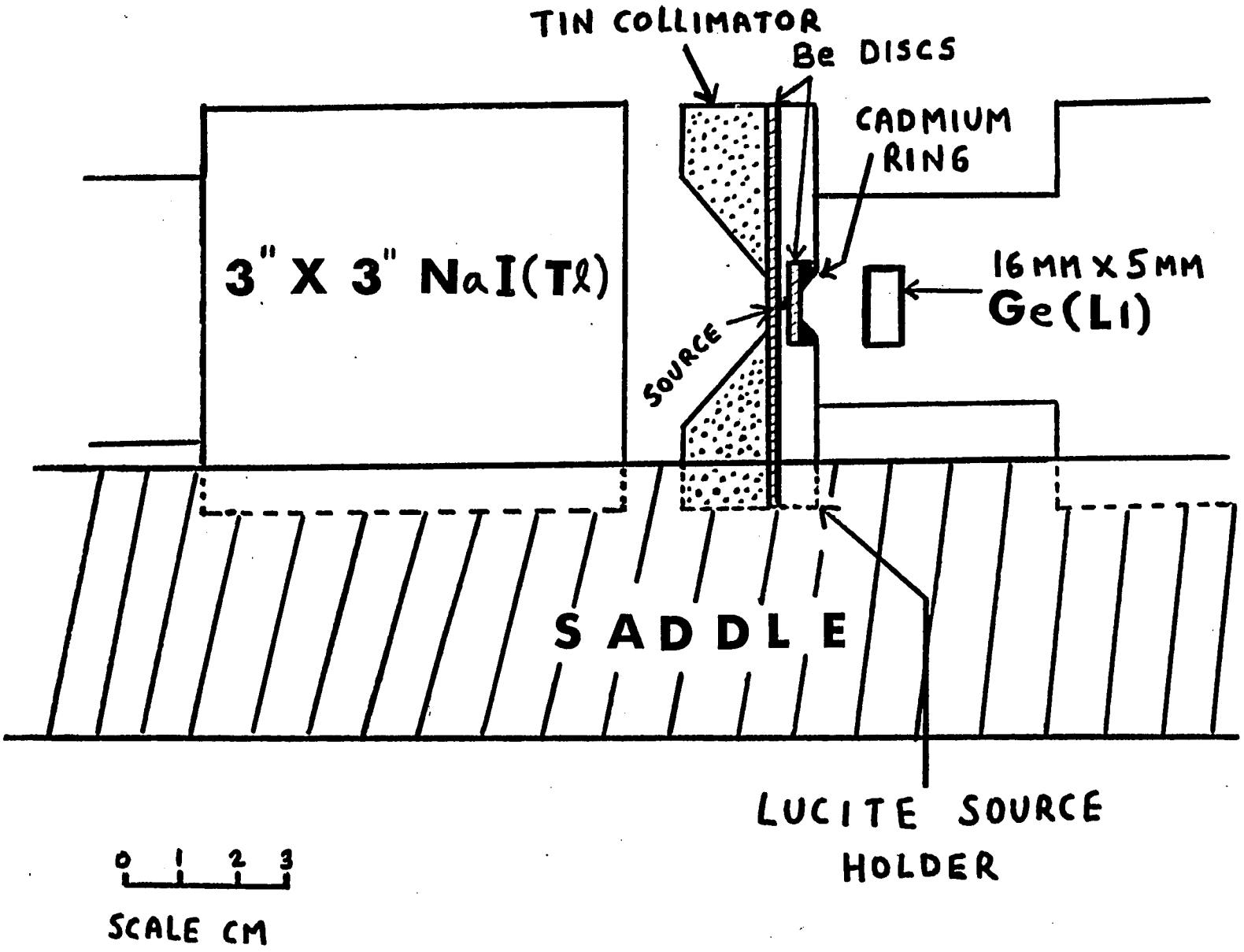

SOURCE HOLDER

FIG 2

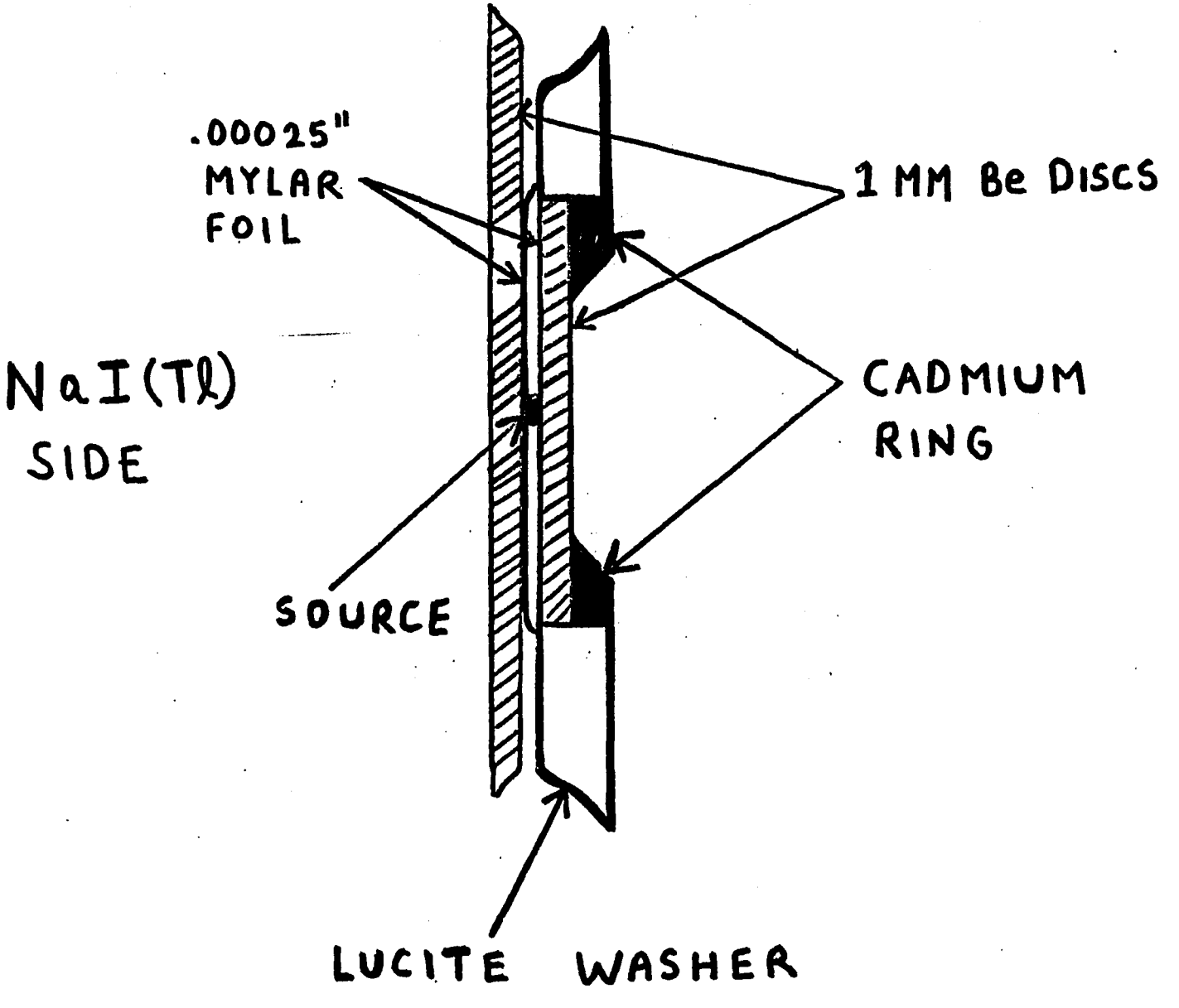

SYSTEM ELECTRONICS

FIG 3

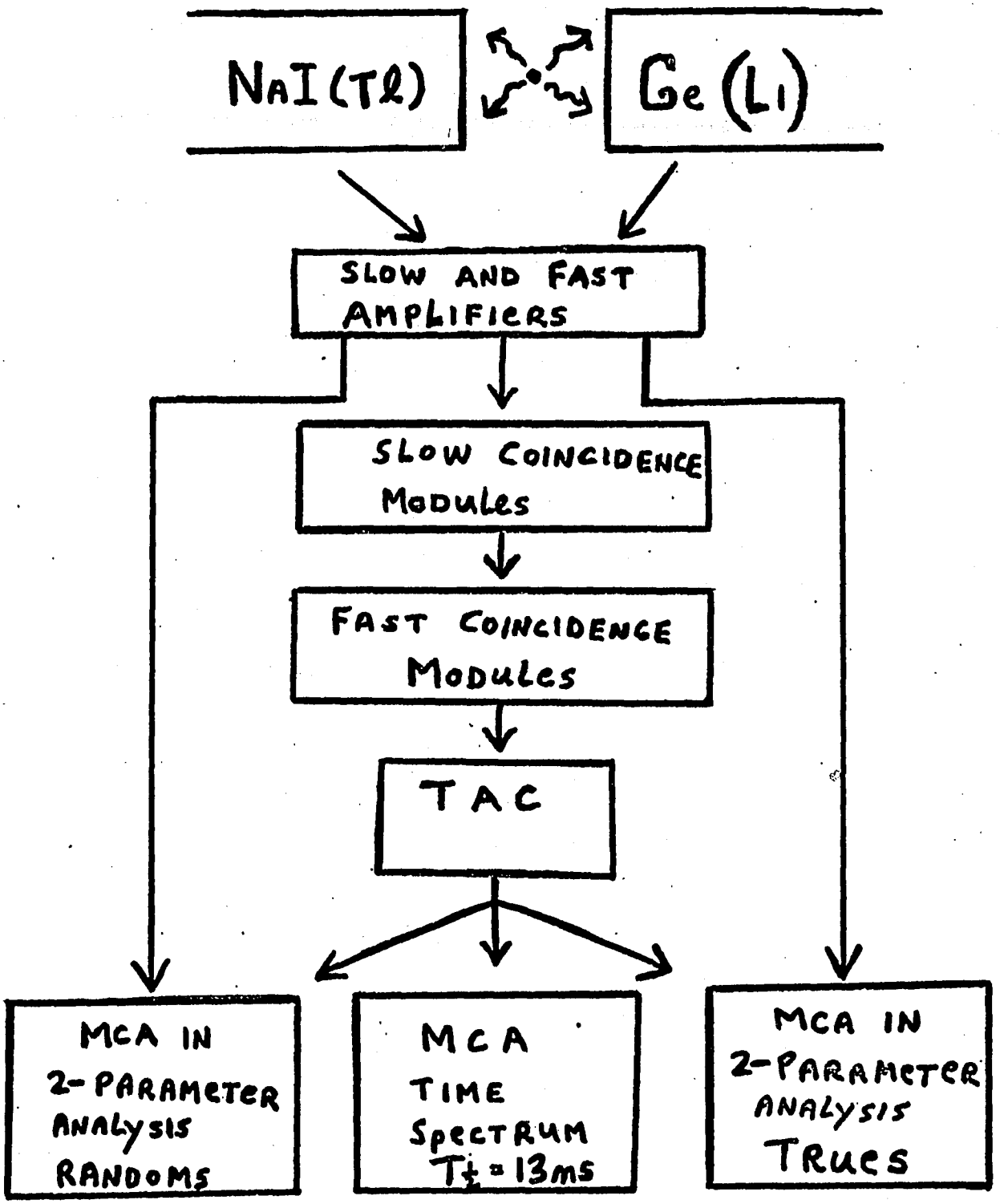

ELECTRONICS MODULES

FIG 4

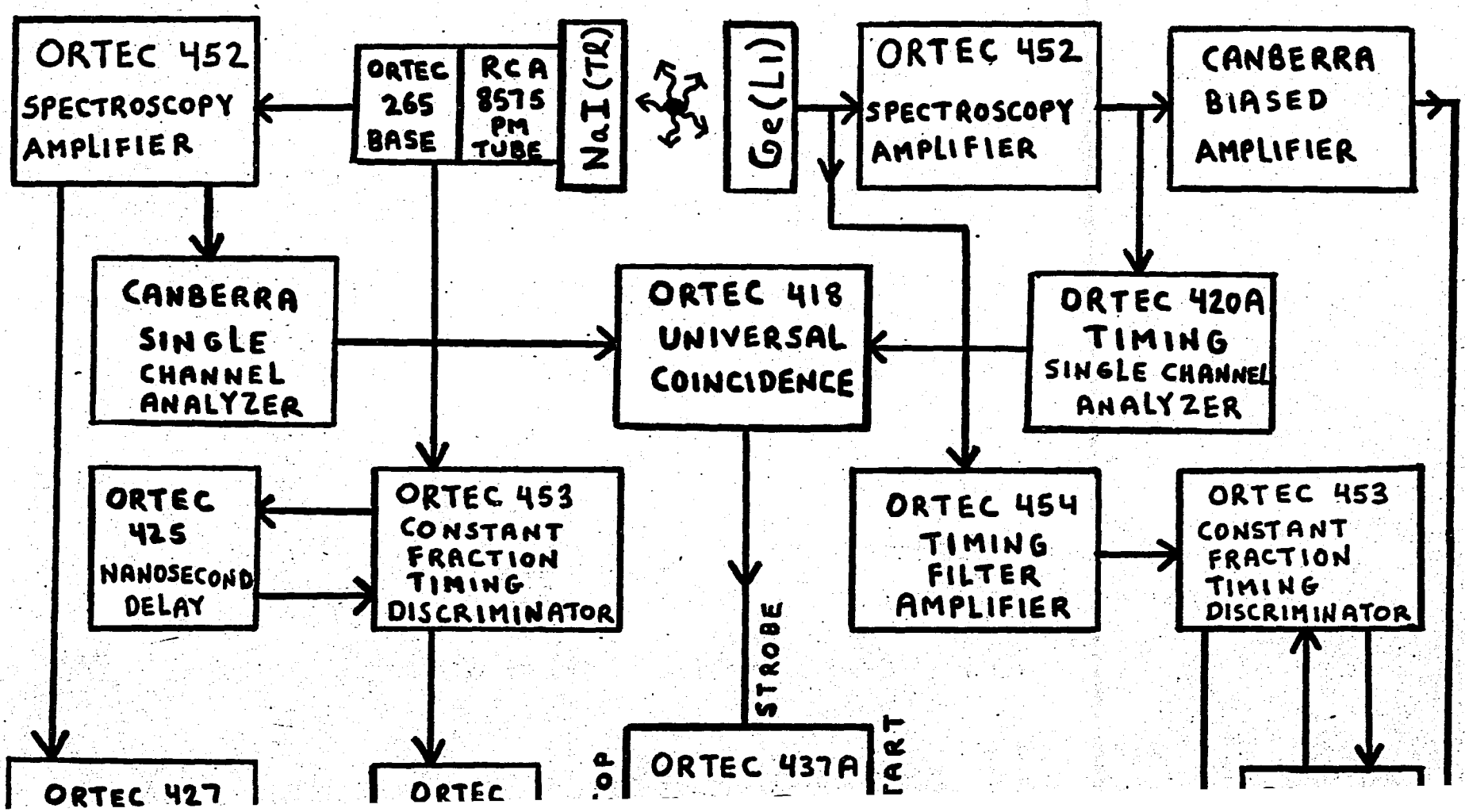

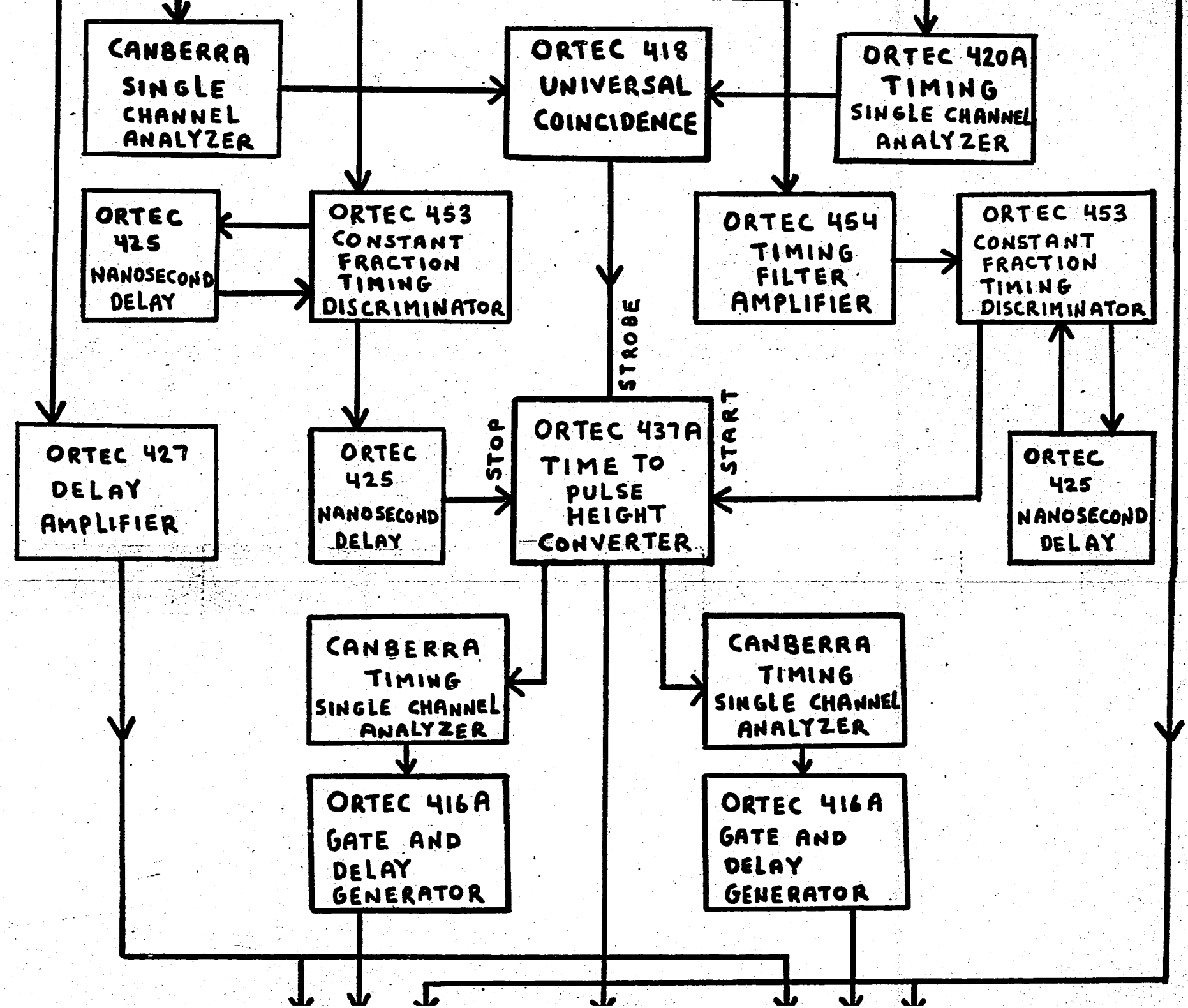
CANBERRA SINGLE CHANNEL ANALYZER
ORTEC 418 UNIVERSAL COINCIDENCE
ORTEC 420A TIMING SINGLE CHANNEL ANALYZER
ORTEC 425 NANOSECOND DELAY
ORTEC 453 CONSTANT FRACTION TIMING DISCRIMINATOR
ORTEC 454 TIMING FILTER AMPLIFIER
ORTEC 453 CONSTANT FRACTION TIMING DISCRIMINATOR
STROBE
ORTEC 427 DELAY AMPLIFIER
ORTEC 425 NANOSECOND DELAY
STOP
ORTEC 437A TIME TO PULSE HEIGHT CONVERTER
START
ORTEC 425 NANOSECOND DELAY
CANBERRA TIMING SINGLE CHANNEL ANALYZER
CANBERRA TIMING SINGLE CHANNEL ANALYZER
ORTEC 416A GATE AND DELAY GENERATOR
ORTEC 416A GATE AND DELAY GENERATOR

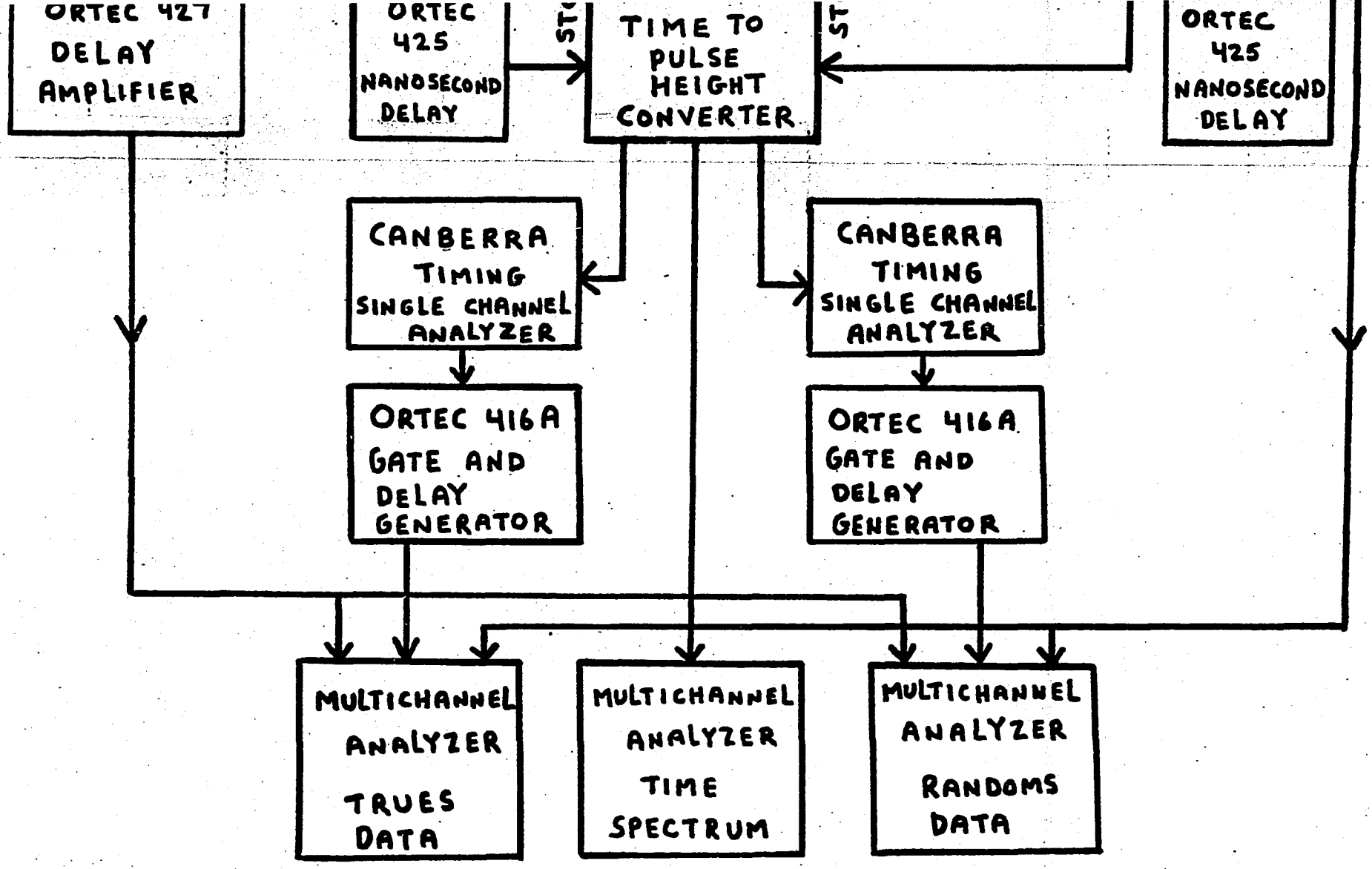
ORTEC 427
DELAY
AMPLIFIER
ORTEC
425
NANOSECOND
DELAY
TIME TO
PULSE
HEIGHT
CONVERTER
ORTEC
425
NANOSECOND
DELAY
CANBERRA
TIMING
SINGLE CHANNEL
ANALYZER
CANBERRA
TIMING
SINGLE CHANNEL
ANALYZER
ORTEC 416A
GATE AND
DELAY
GENERATOR
ORTEC 416A
GATE AND
DELAY
GENERATOR
MULTICHANNEL
ANALYZER
TRUES
DATA
MULTICHANNEL
ANALYZER
TIME
SPECTRUM
MULTICHANNEL
ANALYZER
RANDOMS
DATA

TIME SPECTRUM

1.1 MS PER CHANNEL

FIG 5

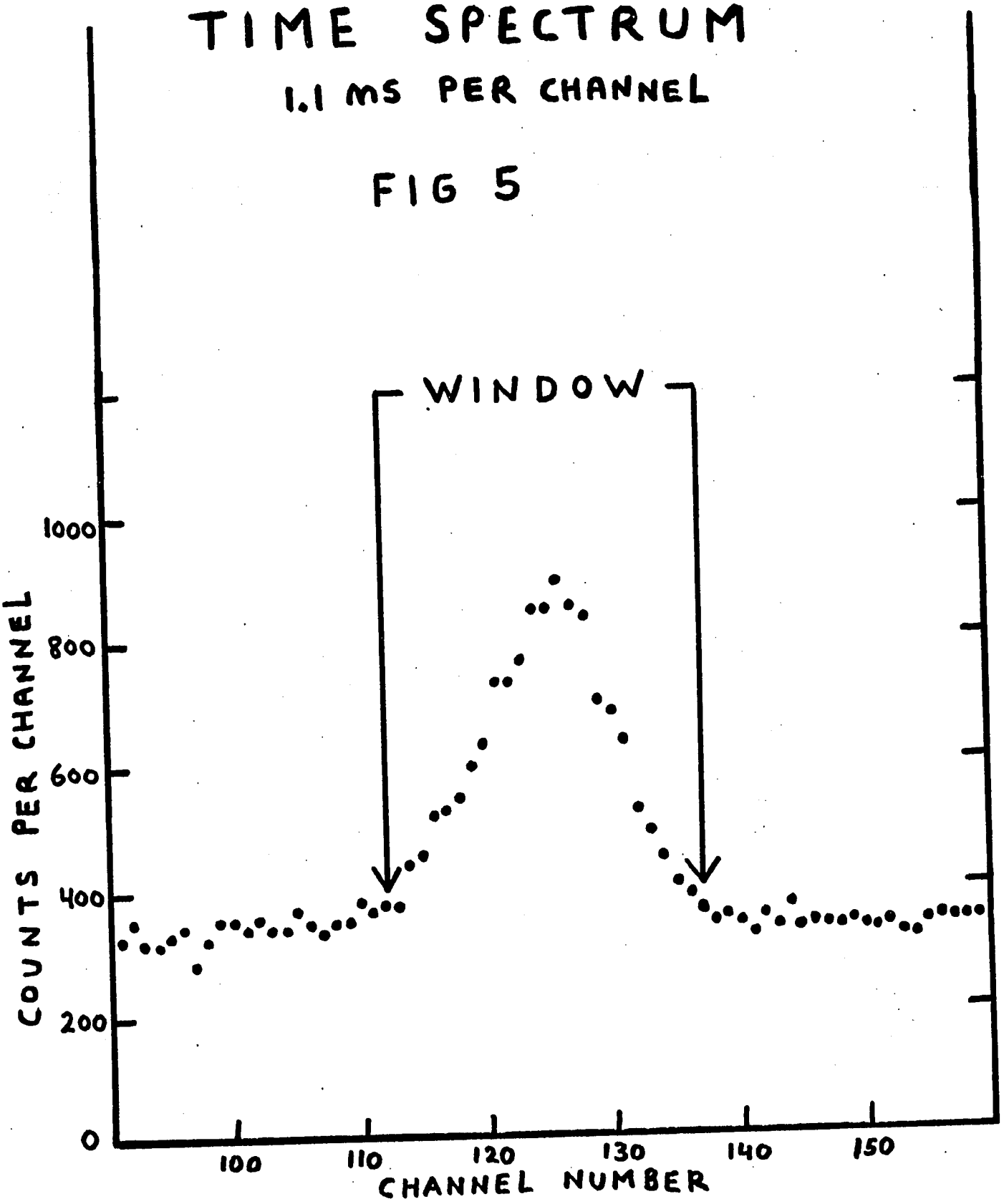

V. SYSTEM COINCIDENCE EFFICIENCY

I. ANALYSIS AND DATA ACQUISITION

The efficiency of the coincidence system was determined using a ^{207}Bi source.

This source is ideally suited for the measurement since it decays through electron capture only, resulting in a high rate of coincidences between ^{207}Pb K x rays and 569.7 keV gamma rays. These energies lie within the ranges of the single-channel-analyzers used in preparing the system for the ^{204}Tl source measurements, and the high rate of coincidences per source decay allowed the measurement to be made in a reasonable amount of time.

The ^{207}Bi source was prepared and mounted on a 1-mm-thick Lucite washer in the same manner as the ^{204}Tl source, and was positioned in the same experimental geometry, and the coincidence efficiency run was made under essentially the same conditions as the thallium source run.

The data, including singles and coincidence data, are summarized in the calculations in this section. The singles spectra of ^{207}Bi taken on the NaI(Tl) and Ge(Li) detectors are presented in Figures 1 and 2.

The ^{207}Bi coincidence data was stored and displayed in the same data acquisition mode as the thallium coincidence data. In this way the multichannel analyzers were checked for reliability in this mode of operation. The pulses from the Ge(Li) detector, containing the Pb K x rays, covered an

energy range 65-87 keV and were stored in the x-parameter, while the pulses from the NaI(Tl) detector, which contained the 570 keV — γ rays, covered an energy range 15-600 keV and were stored in the y-parameter. The coordinates (channels) of the x-axis were regarded as the columns of the matrix, and the coordinates (channels) of the y-axis were taken as matrix rows. The singles spectra from the detectors were stored along their respective axes. Each axis spanned 64 channels, i.e., i=1...64; j=1,...64, and the coincidence data was stored at the coordinates of the matrix. Thus two photons emitted simultaneously by the source with the energies corresponding to Ge(Li) channel i and NaI(Tl) channel j which were detected by the system, would appear as a count at the point (i.j) of the matrix. A diagram of the ^{207}Bi data matrix is given in Fig. 3.

II. CALCULATIONS

From the decay scheme of ^{207}Bi[1] shown in Fig. 4, one can make the following observations. The .5696 MeV level can be reached either directly by electron capture (EC) in 3% of the source decays, or in cascade by EC to higher levels. The EC branching ratio is 9% to the 2.3393 MeV level, 88% to the 1.6331 MeV level, and 3% to the .5696 MeV level. The cascade via EC to the 2.3393 MeV level can be ignored, since K-capture is energetically forbidden to this level and the K-shell internal conversion for the 1.7697 MeV gamma ray is negligible. The 1.6331 MeV state is an isomeric state ($T_{\frac{1}{2}}$= .80 sec), and decays by M4 multipole radiation to the 0.5696 MeV state. This transition is strongly converted. Since the internal conver-

sion coefficient for the K atomic shell, α_K, and the ratio of K-shell conversion to L+M+...conversion is known, one can readily calculate the fraction by which the 1.6331 MeV state decays to the 0.5696 MeV state through K-shell conversion.

Let N_γ equal the fraction of decays resulting in gamma emission, while N_i, i=k,L,...represent the fractions of decays for internal conversion in the $i^{\underline{th}}$ shell. Since

$$\alpha_K = \frac{N_K}{N_\gamma} = 0.096^{(2)}, \quad \frac{N_K}{N_{L+M+\ldots}} = 4.0 \pm 0.25^{(2)}$$

and $$1 = N_\gamma + N_K + N_{L+M+\ldots})$$

then $$\frac{1}{N_K} = \frac{N_\gamma}{N_K} + 1 + \frac{N_{L+M+\ldots}}{N_K}$$

thus $$N_K = 0.086 \pm 0.0001$$

If the decay rate of the source is I_0, then the emission rate of the simultaneous Pb K x-ray—570-keV photons through the decay of the 1.6331 MeV state will be:

$$.88 I_0 N_K W_K = .0727 I_0$$

where we have included the fluorescence yield W_K=.96 of Pb K x rays.[3]

To the above expression we must add the photon coincidences that arise from the electron capture to the 0.5696 MeV level. This requires a knowledge of P_K, the fraction of captures in the K shell. Unfortunately, P_K has not been measured. To determine the value of P_K we can use the formula from Brysk

and Rose:[4]

$$\frac{EC(L_1)}{EC(K)} = K_1 \left(\frac{E-BE(L_I)}{E-BE(K)} \right)^4$$

where E = energy available for the capture transition; $BE(L_I)$ = binding energy of the L_I subshell; and K_1 is a parameter that depends on the automic number. Since the Q-value for electron capture is 2.40 MeV, the energy available for capture to the .5696 MeV state is 1.8304 MeV. The binding energy for the L_1 subshell and the K shell is 15.86 and 88.00 keV, respectively.[1] Using the value k_1 (Z) = 0.15 for Z=82, we get

$$EC(L_I)/EC(K) = 0.175$$

We can express P_K in the following way:

$$P_K = EC(K)/(EC(K) + EC(L) + \ldots)$$
$$= \left\{1 + (EC(L_1)/EC(K)) + (EC(L_1)/EC(K))(EC(L_{II})/EC(L_1))\right\}^{-1}$$

The quantity $\frac{EC(L_{II})}{EC(L_1)}$ is $\approx$ 10%, whereas $\frac{EC(L_{III})}{EC(L_1)}$ is less than 1% and has been neglected.[4]

Using these values we obtain P_K = 0.84.

Thus as a result of EC to the 0.5696 MeV state, we obtain the following intensity of Pb K x-ray --570-keV photon pairs:

$$.03 I_0 P_K W_K = .024 I_0.$$

Combining both terms, we obtain $0.0967 I_0$ as the photon pair emission rate.

In order to determine the number of coincident photons detected by the system, it is necessary to know the source intensity I_0, the efficiencies of the Ge(Li) and the NaI(Tl) detectors, ϵ_{GeLi}^{PbKx}, $\epsilon_{NaI}^{\gamma\text{-}570}$, the electronic coincidence

efficiency of the system, ϵ_{coin} , and the angular correlation between the coincident photons. Here the detector efficiencies are total detection efficiencies including solid angle, and the superscripts indicate the energies at which the detector efficiencies are evaluated. The quantity ϵ_{coin} defines the efficiency of all the electronics, including the fast and slow electronics. If we define the coincidence counting rate as R_c then we get:

$$R_c = .0967\, I_o\, \epsilon_{GeLi}^{PbKx}\, \epsilon_{NaI}^{\gamma\text{-}570}\, \epsilon_{coin} .$$

This expression compares the number of coincidences emitted by the source to the number counted by the system, and can be used to determine the coincidence efficiency ϵ_{coin} . The quantities I_o , $\epsilon_{GeLi}^{Pb\,Kx}$, and $\epsilon_{NaI}^{\gamma\text{-}570}$ can be determined from separate measurements of singles spectra, provided these measurements are carried out in the same experimental geometry as the coincidence measurements.

It is convenient to express $\epsilon_{GeLi}^{Pb\,Kx}$ in terms of ϵ_{NaI}^{PbKx} If R_{GeLi}^{Kx} and R_{NaI}^{Kx} are the number of Pb K x rays counted by the detectors in equal time intervals, then

$$\epsilon_{GeLi}^{Pb\,Kx} = \epsilon_{NaI}^{Pb\,Kx}\, \frac{R_{GeLi}^{Kx}}{R_{NaI}^{Kx}} .$$

Since the photopeak portions of the detector spectra are least likely affected by scattered photons, the above relation is more accurate when R_{GeLi}^{Kx} and R_{NaI}^{Kx} correspond to the number of pulses in the photopeaks. From this relation it is possible to determine the Ge(Li) efficiency ϵ_{GeLi}^{kx} without knowledge

of the source intensity.

A further simplification for R_c can be made. The source decay rate I_o is not easily measured. However, from an examination of the ^{207}Bi decay scheme in Figure 4, one can relate I_o to the intensity of the 570-keV photons, which is an easily measured quantity. The branching ratios to states which populate the .5696 MeV level are known, and the fraction of decays from this level which result in emission of the 570-keV photons can be determined. Defining I_{570} as the intensity of the 570-keV gamma rays, and using symbols previously defined, we obtain:

$$I_{570} = \frac{(.09)(.98)N_\gamma + (.88)I_o N_\gamma + (.03)I_o N_\gamma}{N_\gamma + N_K + N_L + \ldots}$$

where now N_γ and N_i, $i = K, L, \ldots$ refer to the decay of the 0.5696 MeV state

But

$$\frac{N_\gamma + N_K}{N_\gamma} = \left(1 + \alpha_K + \alpha_K\left(\frac{\alpha_{L+M+\ldots}}{\alpha_K}\right)\right)$$

where $\alpha_K = .017$ [2], and $\left(\frac{\alpha_{L+M+\ldots}}{\alpha_K}\right)^{-1} = \frac{N_K}{N_{L+M+\ldots}} = 3.4 \pm 0.4$ [2]

for the .5696 MeV state. Thus we obtain

$$I_{570} = .98 I_o$$

Therefore the intensity of the 570-keV gamma ray is almost the same as the source intensity.

Subtracting this result and the relation developed for ϵ_{6cLi} into the expression for R_c, and rewriting it in terms of ϵ_{coin}

we get

$$\epsilon_{coin} = \frac{(10.1)\, R_c\, R^{Kx}_{NaI}}{\epsilon^{kx}_{NaI}\, R^{\gamma\text{-}570}_{NaI}\, R^{Kx}_{GeLi}}$$

where all the R-labelled terms are normalized to equal times intervals, and where $R^{\gamma\text{-}570}_{NaI} = \epsilon^{\gamma\text{-}570}_{NaI}\, I_{570}$.

We now list the values used in this expression. Referring to Figure 3, if we call the number of counts corrected for background in the channels whose coordinates are (i,j) as N(i,j) then

$$R^{Kx}_{GeLi} = \sum_{i=18}^{35} N(i,1) = 375 \pm 1.12 \text{ sec}^{-1}$$

$$R^{Kx}_{NaI} = \sum_{j=3}^{10} N(1,j) = 819 \pm 1.8 \text{ sec}^{-1}$$

$$R^{\gamma\text{-}570}_{NaI} = \sum_{j=43}^{60} N(1,j) = 369 \pm 1.3 \text{ sec}^{-1}$$

$$R_c = \sum_{j=43}^{60} \sum_{i=18}^{36} N(i,j) = 1.01 \pm 0.016 \text{ sec}^{-1}$$

These expressions were corrected for absorbers and multi-channel analyzer dead time. The value for ϵ^{Kx}_{NaI} was determined by an interpolation over Heath's tabulated values,[5] giving $\epsilon^{kx}_{NaI} = .07 \pm 0.002$.

We obtain $\epsilon_{coin} \approx 86 \pm 3\%$. This result, however, does not take into account the clipping of the tails of the time spectrum, which was done to improve the true-to-random ratio. By

a careful analysis of the area under the time spectrum, this reduction amounted to about 7%.

Thus a more accurate value for ϵ_{coin} is $\approx 93 \pm 3\%$.

This less than perfect value was somewhat disappointing, since there were several attempts at establishing 100% coincidence efficiency. Many of the "bugs" in the system were intermittant, and could not be found at any one time. The fast discriminators posed particularly difficult problems. In the final acceptable run, an Ortec fast discriminator which had a 4% loss of pulses was used. This unit, which was in the x-ray branch, was tested with a pulser which showed that the loss was independent of energy, and thus a direct correction was made.

REFERENCES - SYSTEM COINCIDENCE EFFICIENCY

1. C. M. Lederer, J. M. Hollander, and I. Perlman, "Table of Osotopes" (John Wiley and Sons, Inc., New York, 1967), 6th edition.

2. D. E. Alburger and A.W. Sunyar, Phys. Rev. 99, 695 (1955).

3. R. W. Fink, R. C. Jopson, Hans Mark, and C. D. Swift, Rev. Mod. Phys. 38, 513 (1966).

4. H. Brysk and M.E. Rose, Oaks Ridge National Laboratory Report, ORNL-1830 (1955).

5. R. L. Heath, USAEC Report No. IDO-16880-1, 1964, (unpublished).

^{207}Bi SINGLES SPECTRUM TAKEN WITH THE NaI(Tl) DETECTOR

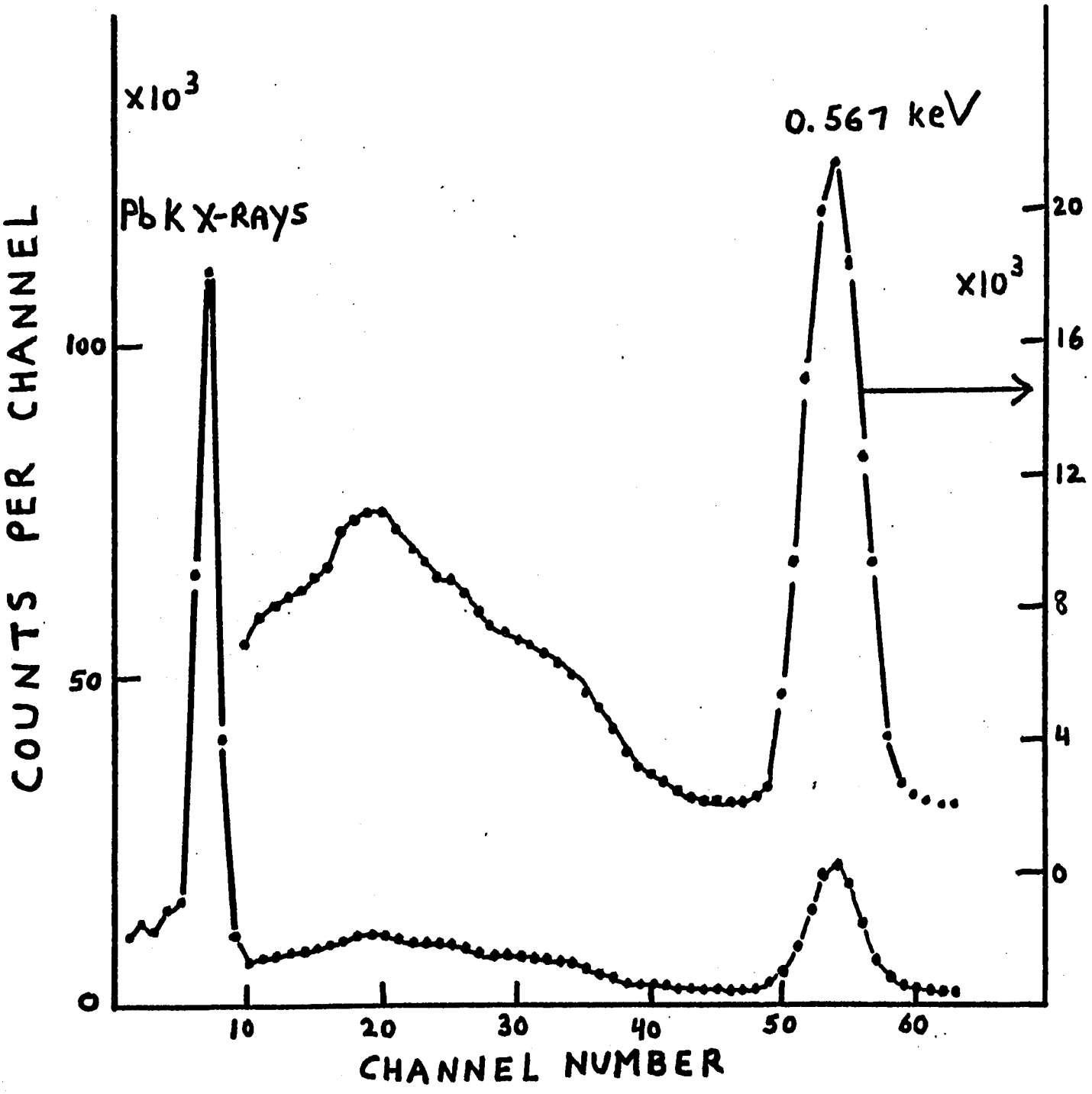

FIG 1

^{207}Bi SINGLES SPECTRUM TAKEN WITH THE Ge(Li) DETECTOR

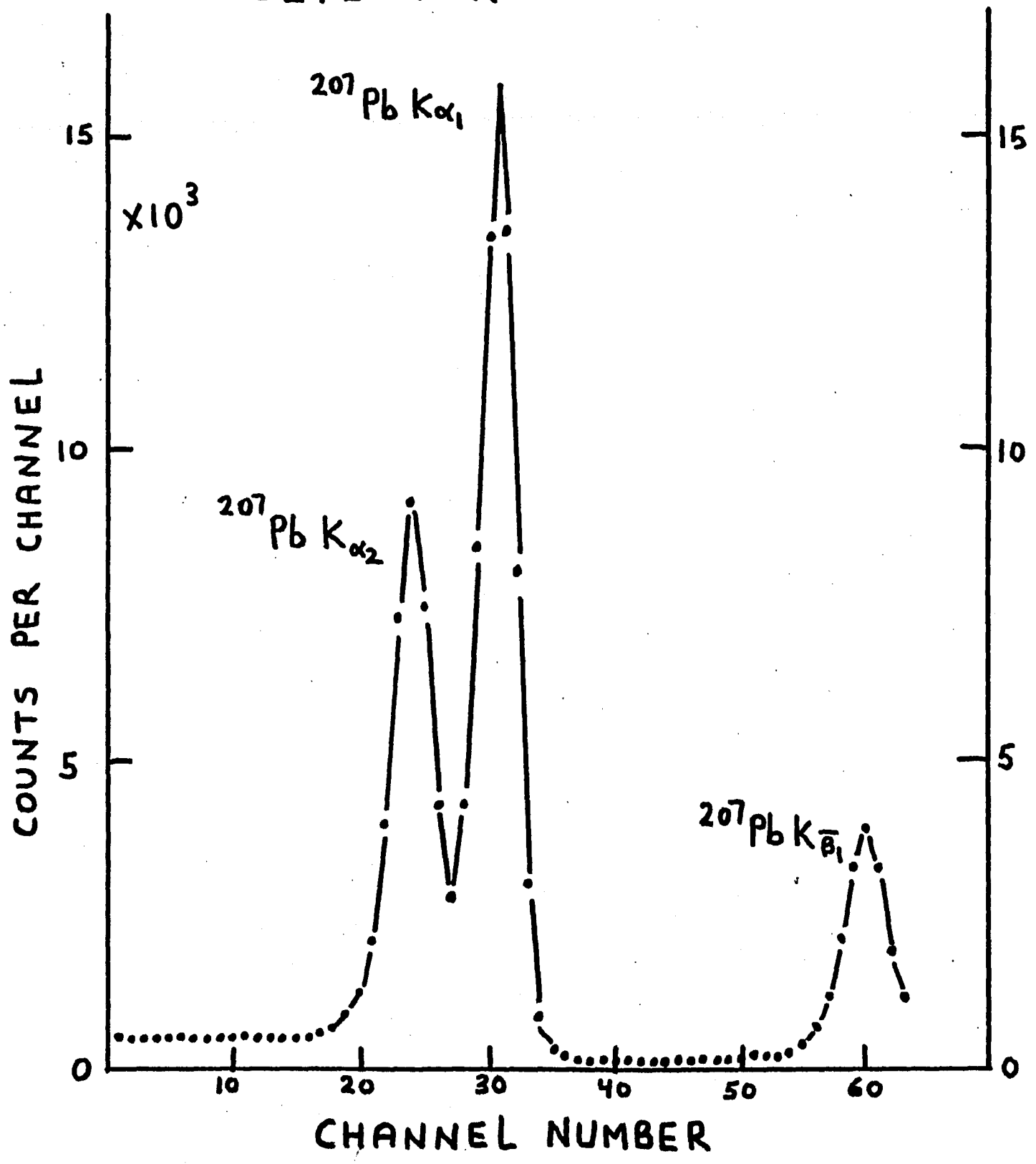

FIG 2

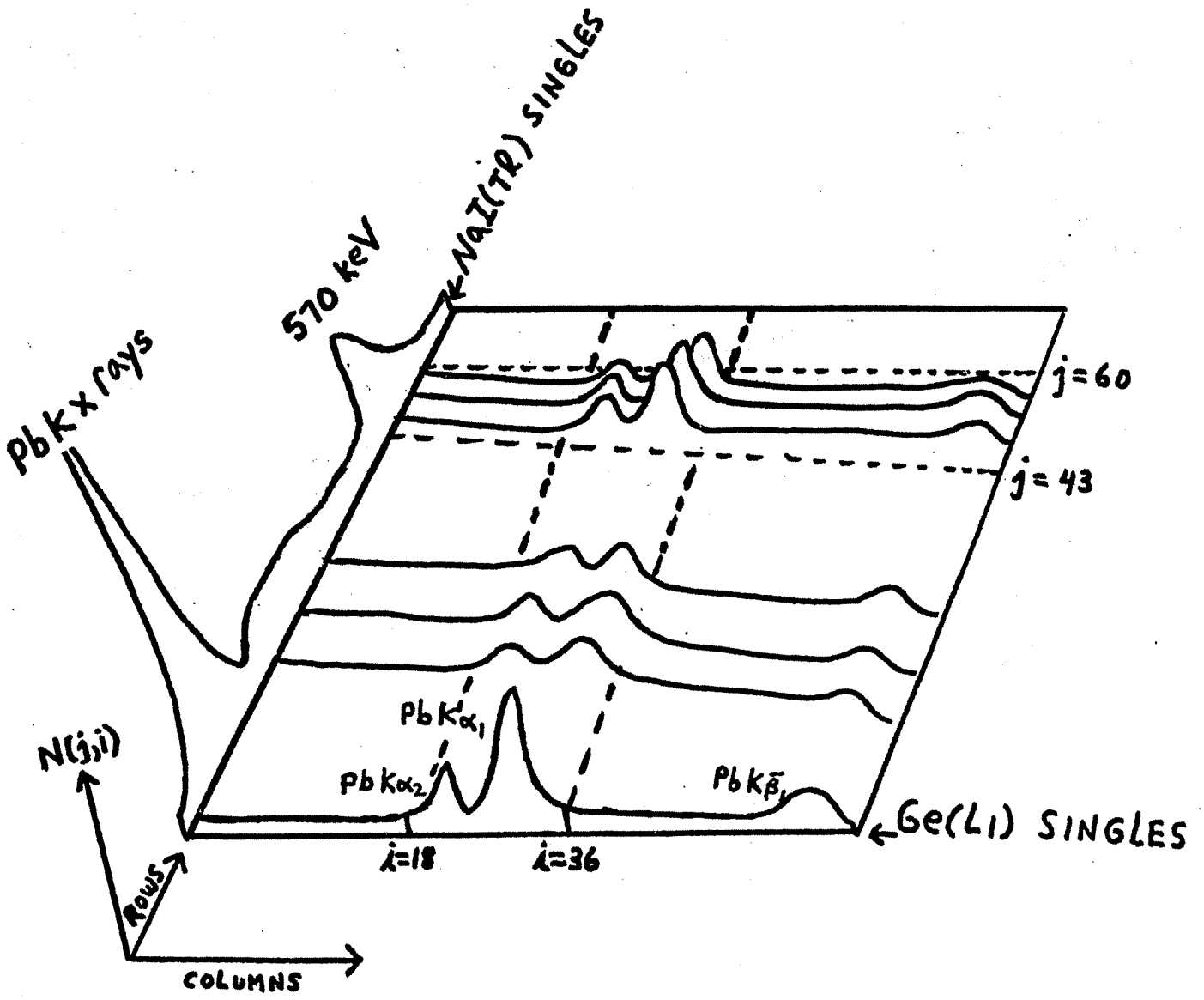

2-PARAMETER DISPLAY OF COINCIDENCE EFFICIENCY DATA

FIG 3

^{207}Bi DECAY SCHEME

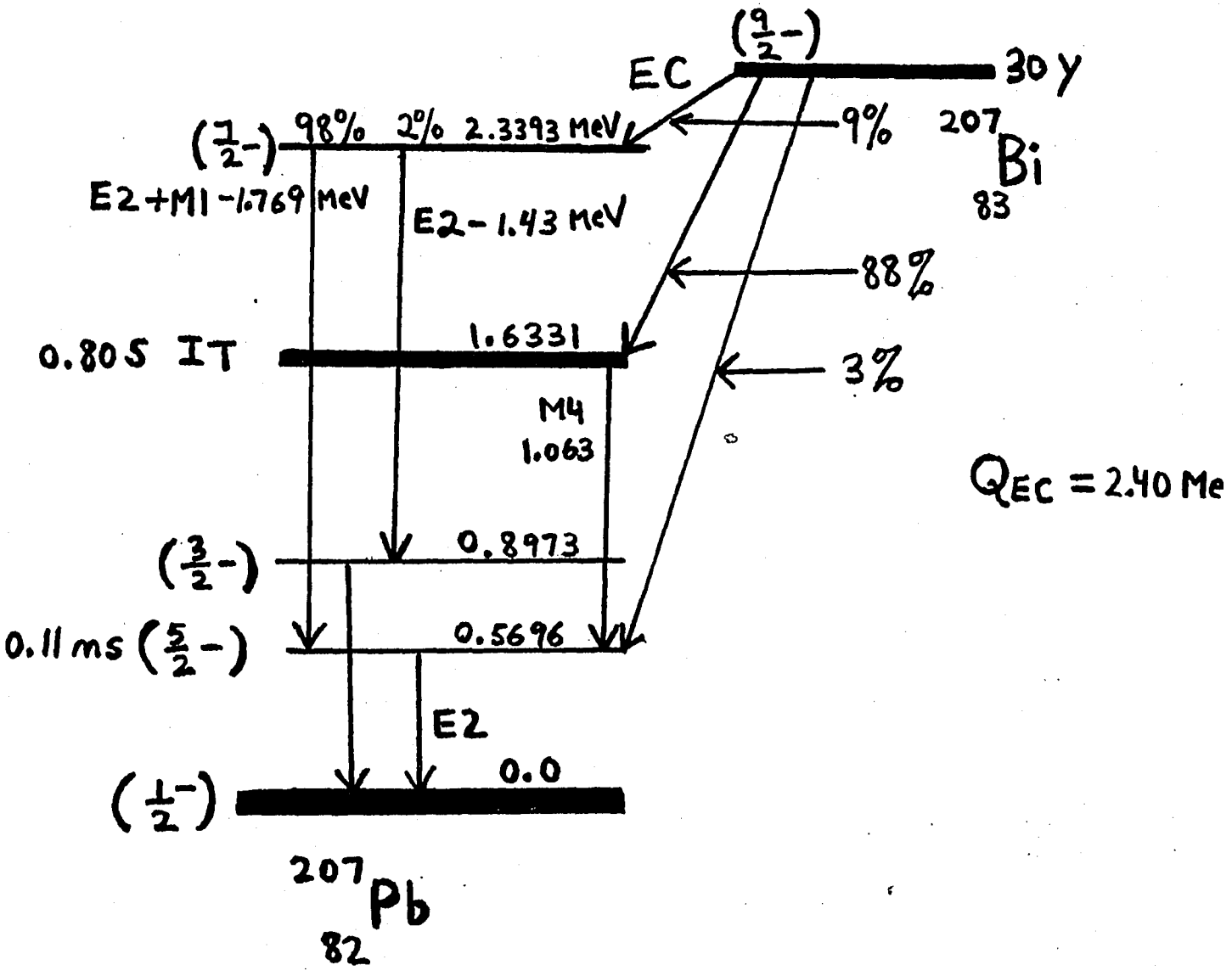

Fig 4

VI. RESPONSE MATRIX OF THE NaI(Tl) DETECTOR

I. PRELIMINARY CONSIDERATIONS

In order to compare the experimental and theoretical data, it was necessary to determine the response of the scintillation detector to monochromatic photons. As is well known, the response of a scintillation spectrometer to a monochromatic gamma ray takes the form of a broad pulse-height distribution. This instrumental distortion of the pulse must be properly understood if observations made with the spectrometer are to be properly interpreted. The pulse-height distributions can be measured for a series of radiactive sources, each emitting only one gamma ray. In order to correct the observed continuous photon spectrum for the influence of the spectrometer, it was necessary to know its output pulse-height distribution for monochromatic gamma rays within the range of the spectrum.

The main components of the pulse-height spectra are the photopeak and Compton regions, which depend on the size and shape of the detector, and on the energy of the incident photons. The shape--and to a lesser degree the magnitude--of the spectra will also be affected by factors related to the experimental environment; for this reason the detector response is always a non-unique function of incident photon energy. Given the experimental setup, the shape of the spectrum can be determined for gamma rays of a number of energies. For arbitrary energies, the response may be found

by interpolation between known responses of standard sources, using a fairly detailed graphical procedure.

We begin our discussion with an analysis of the basic processes involved in the formation of the pulse-height distribution. Finally, the Response Matrix will be constructed.

II. BASIC PROCESSES

The response of the NaI(Tl) crystal to a single gamma ray can be understood from a knowledge of the basic interactions that occur in the detector. The photopeak, or full energy region of the spectrum, is gaussian-like in appearance and is produced by events in which the incident photon delivers all of its energy to the crystal. This can occur either by a photoelectric process or by successive Compton collisions. The photopeak is the most useful component of the pulse height spectrum, since the mean position of the photopeak is proportional to the energy of theincident photon, and the photopeak region is lease affected by scattered radiation and other effects which complicate the interpretation of the pulse-height distribution. The broadening of the photopeak has two main causes--there will be a variation in the number of light flashes produced by the detector for a given quantity of energy absorbed, and for a given quantity of light incident on the photo-cathode of the photomultiplier tube, there will be a statistical fluctuation in the number of electrons emitted.

The second prominent region of the pulse-height spectrum is the Compton distribution. This is represented by a roughly uniform distribution of pulse heights, extending from noise

level up to a maximum value called the Compton edge. In Compton scattering only a fraction of the incident photon's energy is absorbed by the crystal. The remaining energy appears in the scattered photon, and this has a good chance of escaping from the crystal. The pulses in the Compton distribution represent the spectrum of the Compton recoil electrons, and the Compton edge corresponds to the maximum energy transferred to recoil electrons, which occurs at 180 degree scattering (backscattering) of the incident photon. For Compton scattering, if the energy of the incident photon is E_γ and it is scattered through an angle θ, then the energy of the recoil electron is:

$$E_c = \frac{E_\gamma^2 (1-\cos\theta)}{Mc^2 + E_\gamma (1-\cos\theta)}$$

where M is the rest mass of the electron. This relation has a maximum value of

$$E_c = \frac{E_\gamma}{1+(Mc^2/2E_\gamma)}$$

corresponding to the backscattering $(\theta = 180^\circ)$ of the incident photon.

The electrons which are set in motion through photo and Compton collisions release their energy through a large number of secondary encounters with the crystal electrons, which result in low energy photons which are capable of activating the cathode of the PM tube. In order to ensure that this fluorescent radiation has a high probability of escaping the crystal, a small amount of thallium impurity is added to the crystal. This prevents resonance re-absorption of the emitted light.

III. OTHER CONTRIBUTIONS TO THE SPECTRA

It is possible to characterize the components of pulse-height spectra as either characteristic of the crystal properties, or related to the crystal environment. Thus the photopeak and Compton components, whose shapes and relative intensity depend on the physical characteristics of the crystal, are common to all pulse-height spectra, whereas the "backscattering" peak (sometimes referred to as scattering peak), as well as other effects, can be shown to be caused by the crystal environment.

To reduce the level of background radiation, it is usually necessary to operate the NaI(Tl) detector inside a shielded enclosure. This shield represents the major source of scattered radiation. Scattering also occurs from the source holder, the material used to prepare the source, and the packaging material surrounding the NaI detector. A prominent feature of the scattered spectrum is the "backscattered" radiation, which is often manifest as a rather broad peak lying on the flat Compton region.

If the shield is assembled of lead bricks, then characteristic Pb x rays may also appear in the pulse-height spectrum. As is well known, the ejection of a photoelectron from the K-shell of an atom is followed by the emission of characteristic x rays. If a photon which originates in the source interacts at the surface of the walls of the shield through a photo encounter, then Pb x rays may be produced.

Similarly to the production of the Pb x rays, it is also

possible to excite iodine x rays in the surface of the NaI(Tl) detector following a photoelectric event. Photons with energies less than 200 keV incident upon the detector have a large probability of being detected by the photoelectric process. If the interaction occurs near the surface of the detector, iodine K x rays may escape without further interaction. The energy of the x rays (28 keV) will be lost when this occurs, and an additional peak will appear in the spectrum at 28 keV below the photopeak. The escape peak decreases rapidly in intensity with increasing gamma ray energy, and will not be present for energies less than the K-edge of iodine (33.2 keV).

These effects will occur in even "simple" geometries, that is systems consisting of one detector and a minimum amount of material in the experimental geometry. However, in the study of certain phenomena of very low intensity it is not possible to obtain reliable results unless a coincidence measurement is employed, since then events which are random in nature can be properly determined. For these more "complex" systems, two or more detectors are often used, and it is also not uncommon to employ an arrangement of especially designed collimators and filters to reduce scattering between the detectors and block out undesirable coincident events originating within the source. In the present measurements, because of the proximity of the two detectors and the use of a fairly complex geometry, a greater amount of scattered radiation was present in the data than would appear under a more simple arrangement. In particular, the beryllium absorbers, the tin collimator, and the positioning

of the Ge(Li) detector very close to the source resulted in an increase in the number of pulses on the Compton ridge and in the region just below the photopeak of the NaI(Tl) detector spectra.

In order to accurately determine the shape and magnitude of the IB spectrum, it was necessary to include the effects of this "close" geomtry on the bremsstrahlung spectra. This was accomplished by taking spectra of the calibration sources in the same experimental geometry. The experimentally determined shapes of these spectra were then used to interpolate a set of response functions. The interpolation was carried out over the characteristic parameters of the distributions, that is the photopeak, Compton, and backscatter regions. In order to fit these shapes as closely as possible to the experimental shapes the Compton regions were divided into ten sections, and interpolations were performed separately over each section. This procedure was perferred to assuming a Compton distribution of constant amplitude or by fitting the Compton to geometrical shapes, since it gave better fits to the broad bump of the Compton edge and to the upward sweep of the Compton ridge in the direction of lower energies. In addition, by assuring a better fit to the shapes of the experimental Compton distributions, the effects associated with the "close" geometry were more accurately represented in the data. In order to ensure continuity of the pulse-height distribution between the Compton edge and the low energy side of the photopeak, this region was also incorporated into the interpolation procedure.

IV. CONSTRUCTION OF THE RESPONSE MATRIX

IV.1 DEFINITIONS

We have shown that there are certain features common to the pulse-height spectra of single gamma emitters. Examples of the pulse-height spectra of several sources are shown in Figures 1-5. The characteristic features of these spectra have been identified in the figures.

In constructing the response matrix we are interested in the probability that a photon with energy corresponding to mean photopeak channel j is incident on the detector and will be recorded as a pulse in channel i, where j=1,..., 64, and i=1,..., 64. We define this quantity as P_{ji}. This is actually the product of several efficiencies: the geometric efficiency Ω, which is the source solid angle subtended by the detector, and gives the probability that a photon emitted by the source will be incident on the detector; the intrinsic efficiency $\epsilon(E_\gamma)$, which gives the probability that a photon of energy E which is incident on the detector will result in a pulse in any channel; and finally the partial probability a_{ji} that the pulse will occur in channel i.

Thus

$$P_{ji} = \Omega\, \epsilon(E_\gamma)\, a_{ji} .$$

Usually the solid angle efficiency is absorbed into the intrinsic efficiency, and the result referred to as the total detector efficiency, $\epsilon(\Omega, E_\gamma)$. These values have been determined by Heath[1] for standard-sized NaI(Tl) detectors as a

function of energy, for various values of the source-detector distance. The total efficiency for the present experimental source-detector distance of 26 mm is shown in Figure 6.

The quantities a_{ji} were determined from the shapes of the calibration spectra, which were principally due to the photo and Compton processes. In order to obtain the relative intensities of these processes for any j value, it was necessary to know the peak-to-total ratio as a function of bremsstrahlung channel j. The peak-to-total ratio is defined as the ratio of the number of pulses under the photopeak to the total number of pulses in the pulse-height spectrum of a single energy gamma emitter. By using the calibration sources discussed earlier under the same experimental conditions, it was possible to obtain values of this ratio at several energies. These values were plotted and connected by a smooth curve to obtain the peak-to-total ratio over a broad range of energies. This curve is represented in Figure 7. In determining the peak-to-total ratios of the calibration spectra, the backscattering peak and Compton edge were excluded from the summations over the Compton regions. This was done since these effects were evaluated separately.

The peak-to-total ratio obtained by Heath[1] under "ideal" experimental conditions is also included for comparison with the present values. In Heath's geometry, scattering and other environmental effects were negligible. The curve through Heath's data points gives the theoretical peak-to-total ratio. It is seen that the use of a "close" geometry affects the peak-

to-total ratio, and to use theoretical estimates of this quantity would not be accurate. The present data shows fair agreement with the shape of the theoretical curve, but the magnitude of the data taken in "close" geometry is lower than the theoretical (ideal geometry) values. It is assumed that this difference is due largely to scattering of the source photons from the tin collimator, which results in a lowering of the peak-to-total ratios.

IV.11 PHOTOPEAK ANALYSIS

Spectra of the calibration sources were taken in the same source-detector geometry as in the determination of the bremsstrahlung spectra. A "dummy" source measurement was taken to determine the background, which was subtracted from the calibration data. Figures 1-5 show these resulting spectra. The various components of these spectra have been indicated on the figures.

Two quantities were determined from the photopeak portion of each spectrum: the full width at half-maximum peak height (FWHM), and the center of the photopeak in channel units, which was not necessarily in integer values. We have assumed that the photopeaks could be satisfactorily described by a gaussian function:[1][2]

$$y(x) = y_0(x_0)\, e^{-(x-x_0)^2/b_0}$$

where y is the calculated value in channel X, X_0 is the channel (pulse height) at the center of the symmetrical dis-

tribution, and y_o is the calculated number of counts per channel at channel x_o. The FWHM for this peak is

$$\Delta E_{\frac{1}{2}} = 2\sqrt{\ln 2}\,\sqrt{b_o}$$

By using the transformation equations

$$\mu = \ln y \;,\quad K = \ln y_o - x_o^2/b_o$$
$$L = 2x_o/b_o \;,\quad M = -1/b_o$$

the guassian can be transformed into a parabola

$$\mu = K + Lx + Mx^2$$

This equation was fitted to the channels of the experimental photopeaks by a least-squares routine to obtain best estimates of y_o, x_o and b_o. The guassians obtained from these estimates were compared to the experimental data points, and the fits were quite good, except for the tails of the photopeaks, which showed some deviation from the guassian shapes. These low energy tails are due to multiple scattering events in the detector which do not result in full-energy loss, while the high energy tails are thought to be caused by optical problems in the detector.[1] Smooth curves were drawn through the photopeak channels. These are shown in Figures 8-12. The FWHM values of these curves were measured, and compared to the calculated values of $\Delta E_{\frac{1}{2}}$. It is seen that the fits are good, and that the approximation to the photopeaks as gaussians is satisfactory. The values of x_o and $\Delta E_{\frac{1}{2}}$(calculated) for the calibration energies are presented in Table II of the section on Detector Calibrations.

From the above values of X_o and $\Delta E_{\frac{1}{2}}$, a curve was constructed so that $\Delta E_{\frac{1}{2}}$ for all integer channels could be determined graphically. The resulting curve is shown in Figure 13. In this manner the photopeaks correponding to all channels j of the response matrix were determined.

To determine the distribution of pulses belonging to the photopeak centered on channel j, first each channel in the photopeak was integrated over its limits to give the fraction of the photopeak in that channel, and then the total area of the photopeak was normalized to 1000 counts. These integrations were easily performed by expressing the extremes of each channel in units of σ, the standard deviation of the photopeak, and then referring to standard tables on the normal distribution. In determining these areas we have assumed that all channels have the same width, and that the mean pulse in a channel occurs at the center of the channel. The photopeak portion of the response matrix is shown in Table I. Only that portion of the matrix (rows 9-40) which was significant in the calculations is shown. The data is arranged so that the rows of the matrix are ordered horizonally, and the columns of the matrix are ordered diagonally. Finally, to include the effect of NaI(Tl) detector efficiency on the matrix elements, each row j of photopeak entries must be multiplied by $\epsilon(\Omega, E_\gamma)$.

IV.111 COMPTON MATRIX ELEMENTS

The following procedure was used to calculate the Compton elements in the response matrix. First, the Compton portions of the experimental calibration spectra were multiplied by

the necessary factors to give the proper peak-to-total ratios, assuming a photopeak intensity of 1000 counts. The resulting spectra preserved the shapes of the experimental spectra. In order to maintain normalization to a source emission rate of 1000 counts/sec, these spectra were multiplied by their respective peak-to-total ratios. Finally, since the intensity of the whole spectrum in a given row is proportional to the probability of locating a pulse in that row, each row was multiplied by its corresponding $\epsilon(\Omega, E_\gamma)$ value.

This procedure was repeated on the Compton regions of all the calibration spectra. The resulting spectra, whose shapes follow the exact experimental shapes, were used to generate the Comptons for intermediate energy spectra. This was accomplished by dividing the Compton region, from zero pulse height to the Compton edge, into ten sections and interpolating between corresponding sections.

In order to check the accuracy in the intensity of the interpolated spectra, the peak-to-total ratios of these spectra were measured, and compared to the data of Figure 7. It was found that the agrement was within 1%, except for the spectra between ^{7}Be and ^{51}Cr, where the difference was as high as 7%. The Compton intensities in these spectra were corrected to give the proper peak-to-total ratios. The Compton elements of the response matrix are shown in Table II. These values include the effect of the NaI(Tl) detector efficiency on the matrix elements a_{ji}.

IV.IV BACKSCATTERING

The backscatter contributions to the matrix elements were obtained by empirically determining both the intensity and position of the backscatter peak along each row of the matrix. The FWHM values of these peaks were obtained from their energies by using Fig. 13. The method used her to analyze the backscatter is similar to that used by Bosch and Munczek,[3] and Olsen, Mann and Lindner.[4]

Curve 14 shows the backscatter contribution to the pulse-height spectra as a fraction of the full energy peak, plotted against incident photon energy. The curve is a smooth fit through data points collected with the calibration sources. An additional point was taken with a ^{137}Cs source. One can see that for incident photon energies less than 400 keV, the intensity of backscattering is less than 7% of the photopeak.

In general, as the size of the shield housing increases, the scattering peak becomes narrower and approaches a monochromatic line, since then the solid angle for a point on the shield to the detector volume decreases and the detector views only 180° scattered photons from the shield wall. The relation in energy between the incident and Compton scattered photons was given previously. For 180° scattered photons, this relation becomes:

$$E_{back} = \frac{E_{INC}}{1+(2E_{INC}/511)}$$

where the energies are expressed in keV. This relation, which allows one to fix the position of the backscatter peak in relation to the photopeak assuming perfect 180° scatter-

ing, was compared to the experimentally determined scattering data (Figure 15). One can see that in the energy range presented, the curves agree in shape, but the experimental data is higher than the theoretical data by an average of about 10%. This is not surprising, since photons scattered through angles other than 180° have greater energy than photons scattered through 180° . The ordinate of the graph gives the backscatter peak pulse height as a fraction of the photopeak pulse height, where the median pulse heights to the peaks were taken. On the basis of this data, the backscatter peak along each row of the matrix was determined, and added to the appropriate matrix elements.

IV.V IODINE ESCAPE X-RAYS

The magnitude of this effect is about 1% to 5% of the photopeak and it occurs in a part of the matrix where the matrix elements are very small. However, its contribution to these maxtrix elements is as high as 50%. A quantitive prediction of this effect which considers the fluorescence yield of iodine has been determined by McGowan[5] for a source-detector distance of 10 cm (Fig. 16). Since the present measurements were taken at a source-detector distance of 2.6 cm, the McGowan results do not carry over directly. The magnitude of this effect could not be reliably determined from the present experimental data, since it occurs over an energy range for which there was insufficient data to construct a curve. Thus it was decided to adopt the McGowan results, with the following proviso as to their applicability: As the source-detector distance is

decreased, the fraction of the escape peak in the spectrum increases, since edge effects reduce the effective solid angle for photon detection, whereas iodine escape occurs at the crystal surface and thus is not similarly affected.

An estimate of the discrepancy due to this difference in source-detector distance was made with the ^{141}Ce source, where it was possible to measure the escape probability. This gave a value of 4%, compared to the McGowan value of 2%. Thus the data of McGowan is employed with the understanding that these values are probably lower than the actual experimental values. The difference is expected to be smaller for incident photon energies less than the 145-keV Ce line, since the influence of edge effects diminishes for lower photon energies. The iodine escape effect was added to the matrix elements for incident photon energies in the range 100-170 keV. It is estimated that taking the McGowan data underestimates the magnitude of the IB in this energy range by about 1%.

REFERENCES - NaI(Tl) DETECTOR RESPONSE MATRIX

1. R. L. Heath, USAEC Report No. IDO--16880-1, 1964 (unpublished).

2. R. G. Helmer, R. L. Heath, Marie Putnam, and D. H. Gibson, A Non-Linear Least-Squares Program for the Determination of Parameters of Photopeaks by the Use of a Modified Gaussian Function, IDO-17015 (1964).

3. H. Bosch and H. Munczek, Phys. Rev., 106, 983 (1957).

4. J. L. Olsen, L. G. Mann, and M. Lindner, Phys. Rev., 106, 985 (1957).

5. F. McGowan, Phys. Rev., 93, 163 (1954).

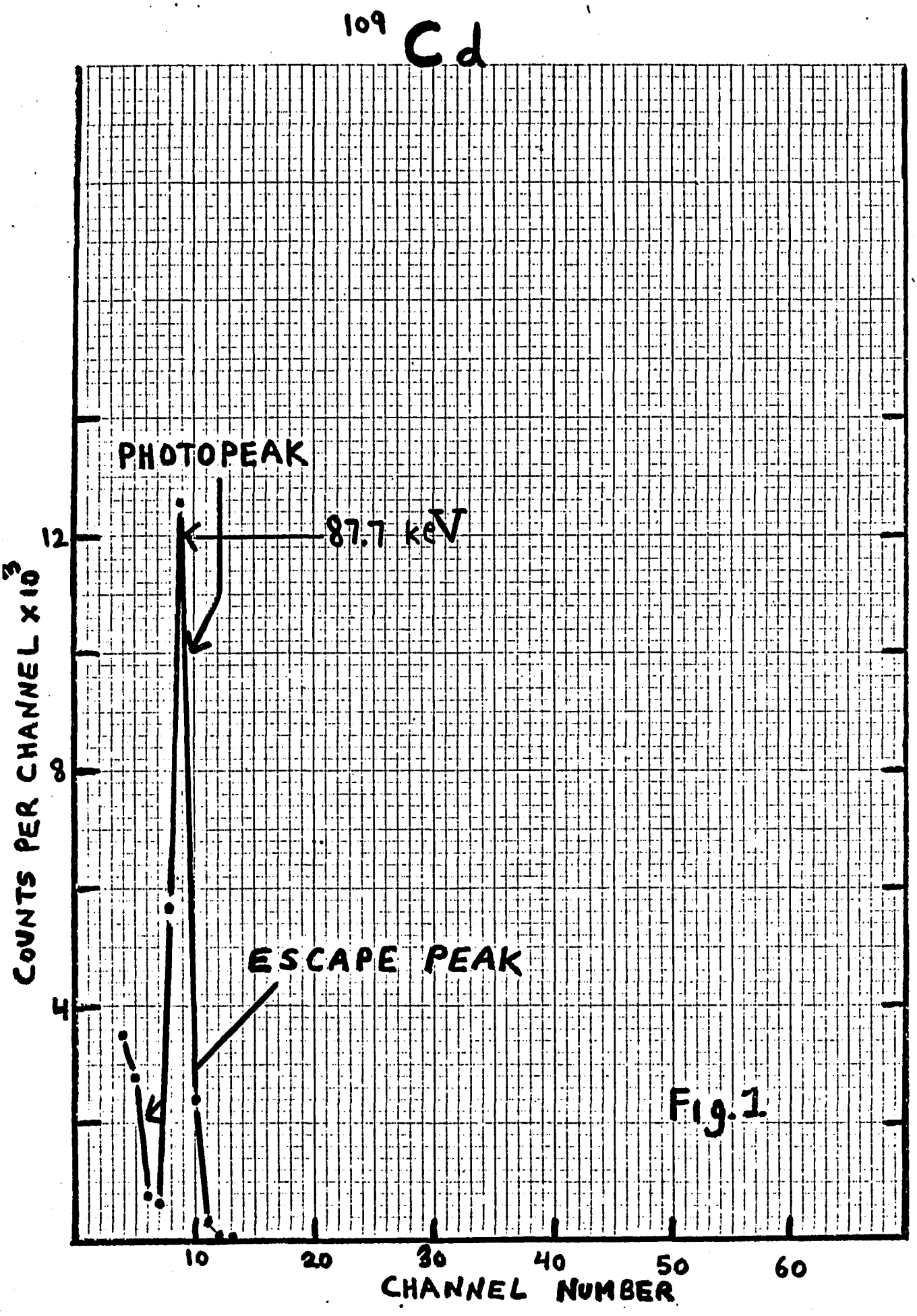
109 Cd
PHOTOPEAK
87.7 keV
ESCAPE PEAK
COUNTS PER CHANNEL x 10^3
12
8
4
10
20
30
40
50
60
CHANNEL NUMBER

Fig. 1

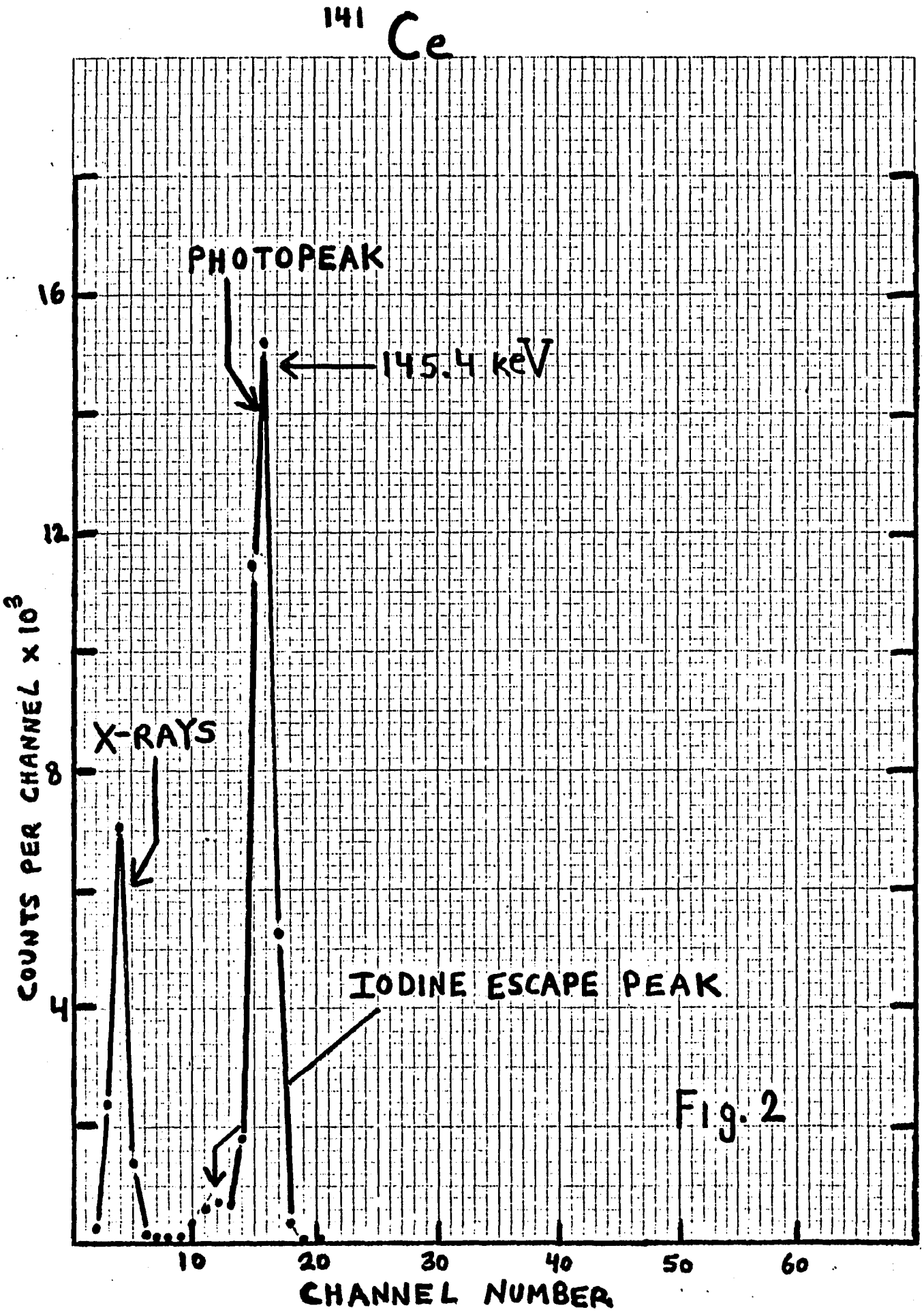
141 Ce
PHOTOPEAK
145.4 keV
X-RAYS
IODINE ESCAPE PEAK
COUNTS PER CHANNEL x 10^3
16
12
8
4
10
20
30
40
50
60
CHANNEL NUMBER

Fig. 2

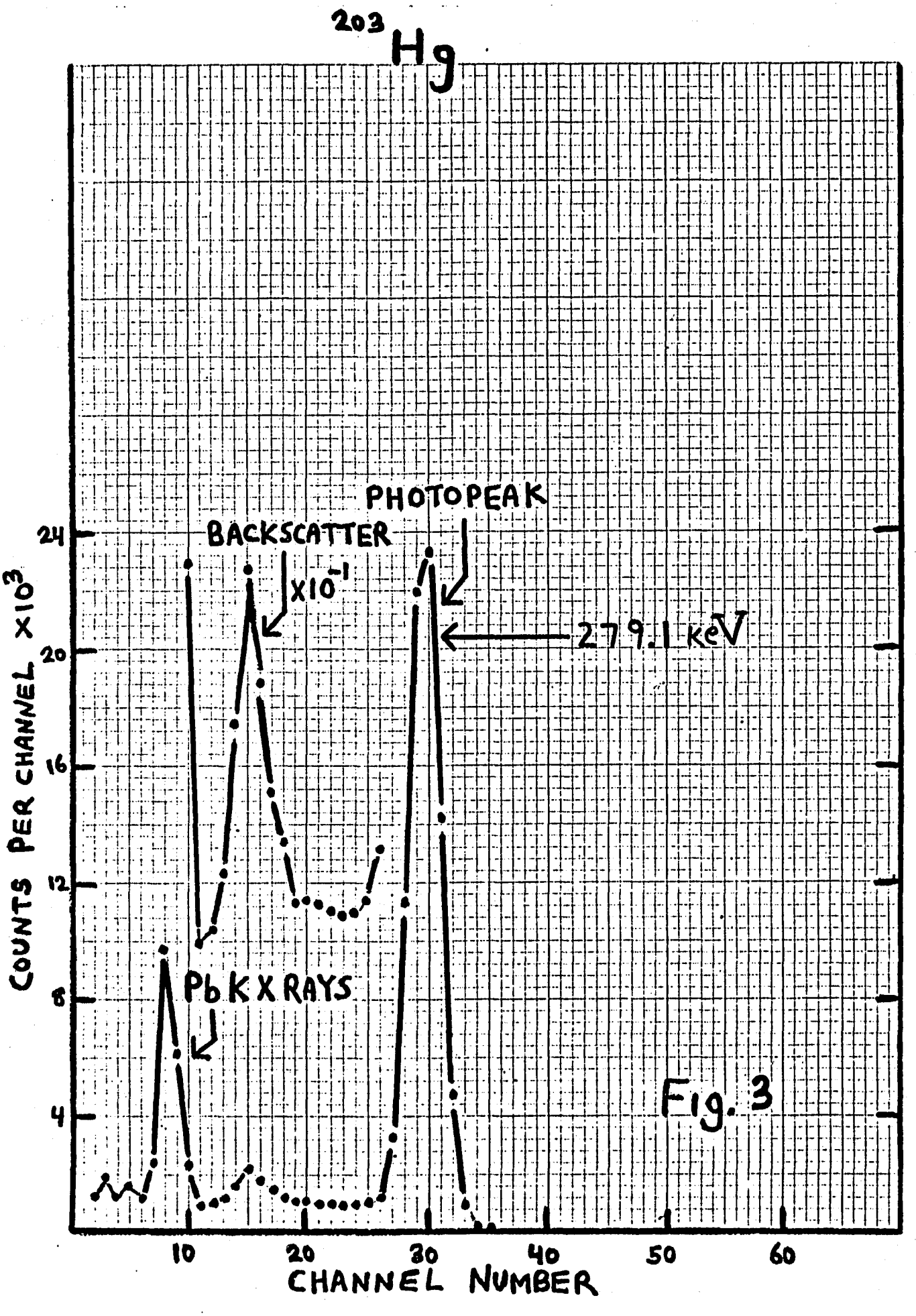
^{203}Hg
PHOTOPEAK
BACKSCATTER
X10^{-1}
279.1 KeV
Pb K X RAYS
COUNTS PER CHANNEL X10^3
24
20
16
12
8
4
10
20
30
40
50
60
CHANNEL NUMBER

Fig. 3

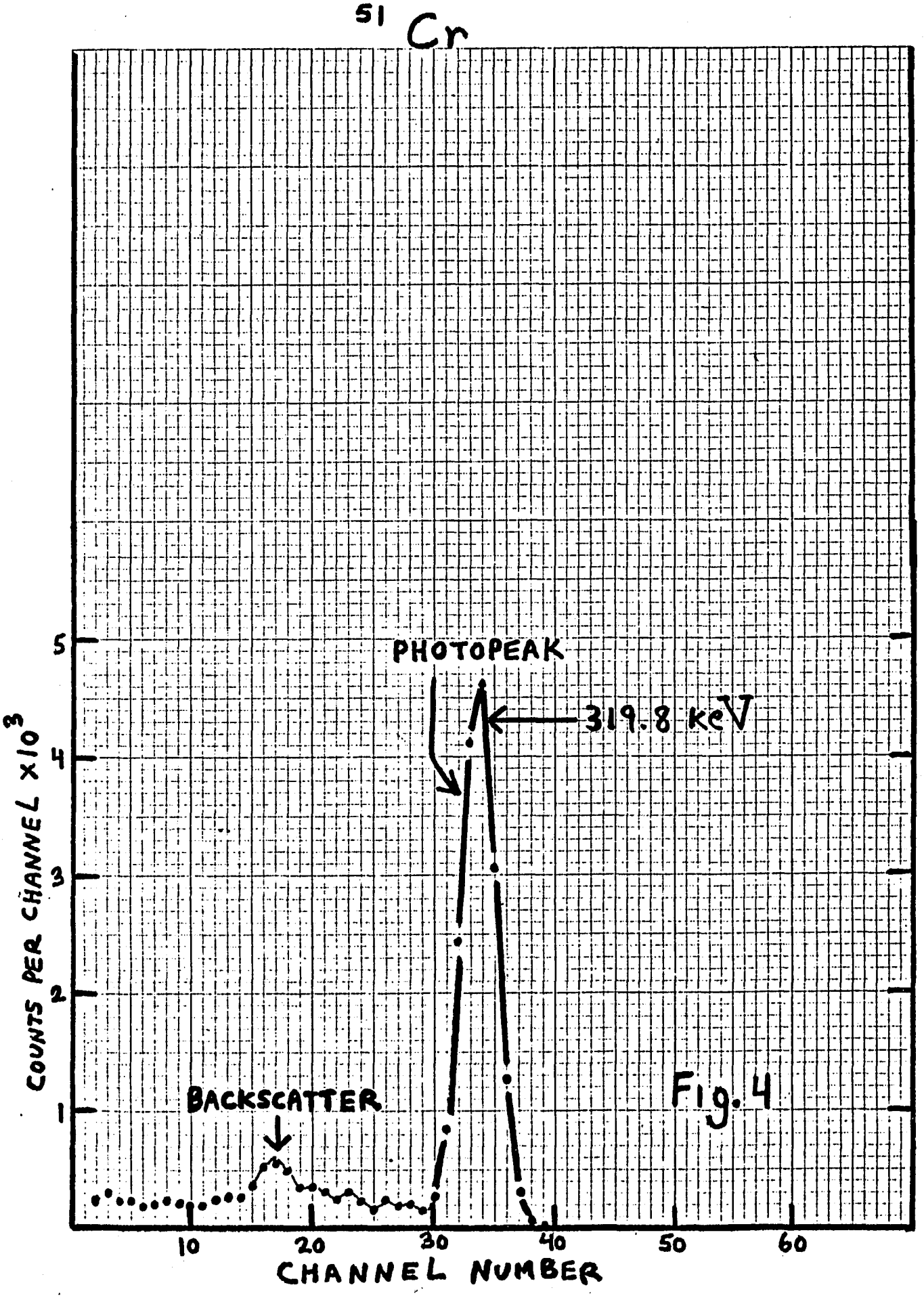
^{51}Cr
PHOTOPEAK
319.8 KeV
BACKSCATTER
COUNTS PER CHANNEL X10^3
1
2
3
4
5
10
20
30
40
50
60
CHANNEL NUMBER

Fig. 4

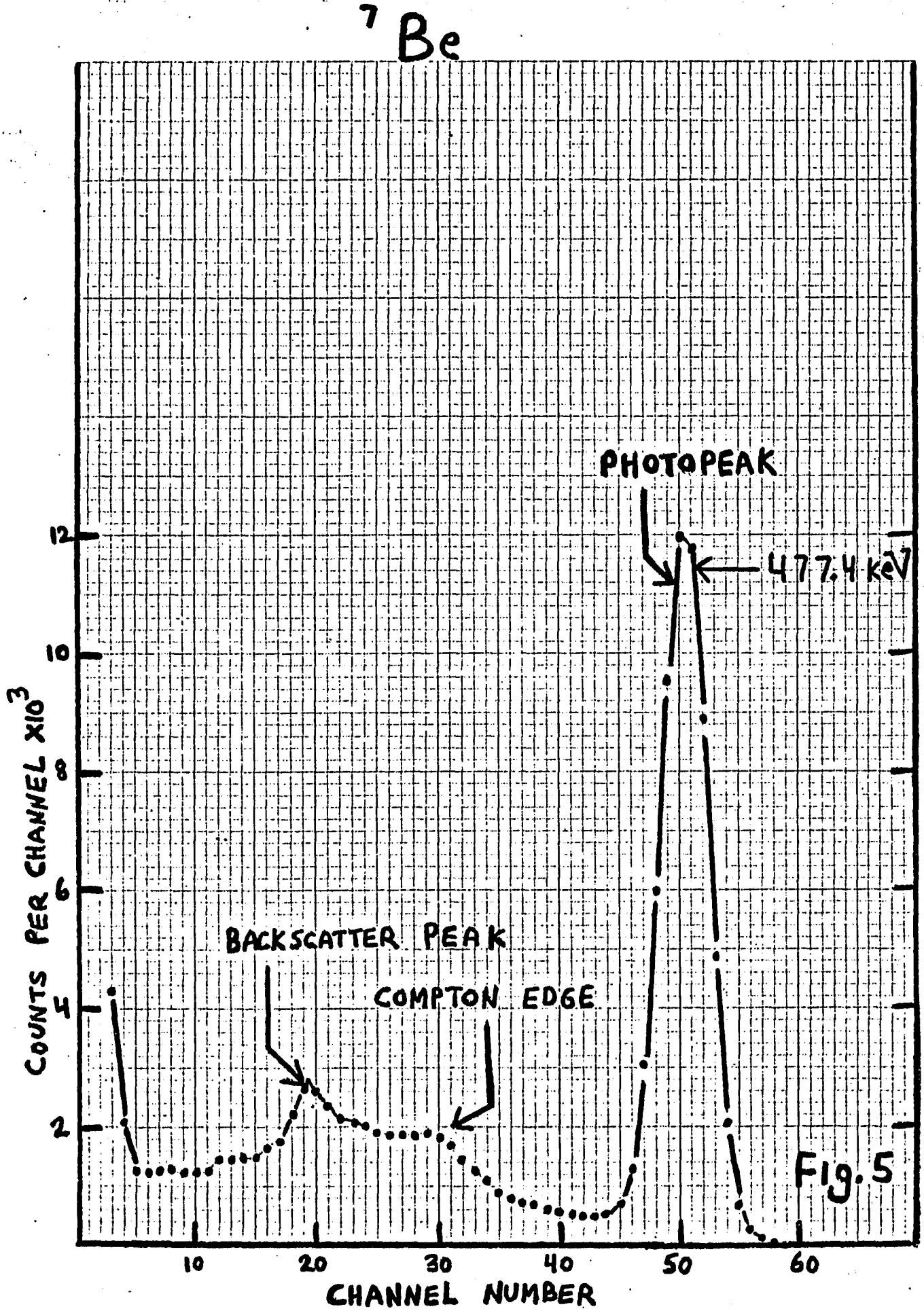
^{7}Be
PHOTOPEAK
477.4 keV
BACKSCATTER PEAK
COMPTON EDGE
COUNTS PER CHANNEL X10^{3}
12
10
8
6
4
2
10
20
30
40
50
60
CHANNEL NUMBER

Fig. 5

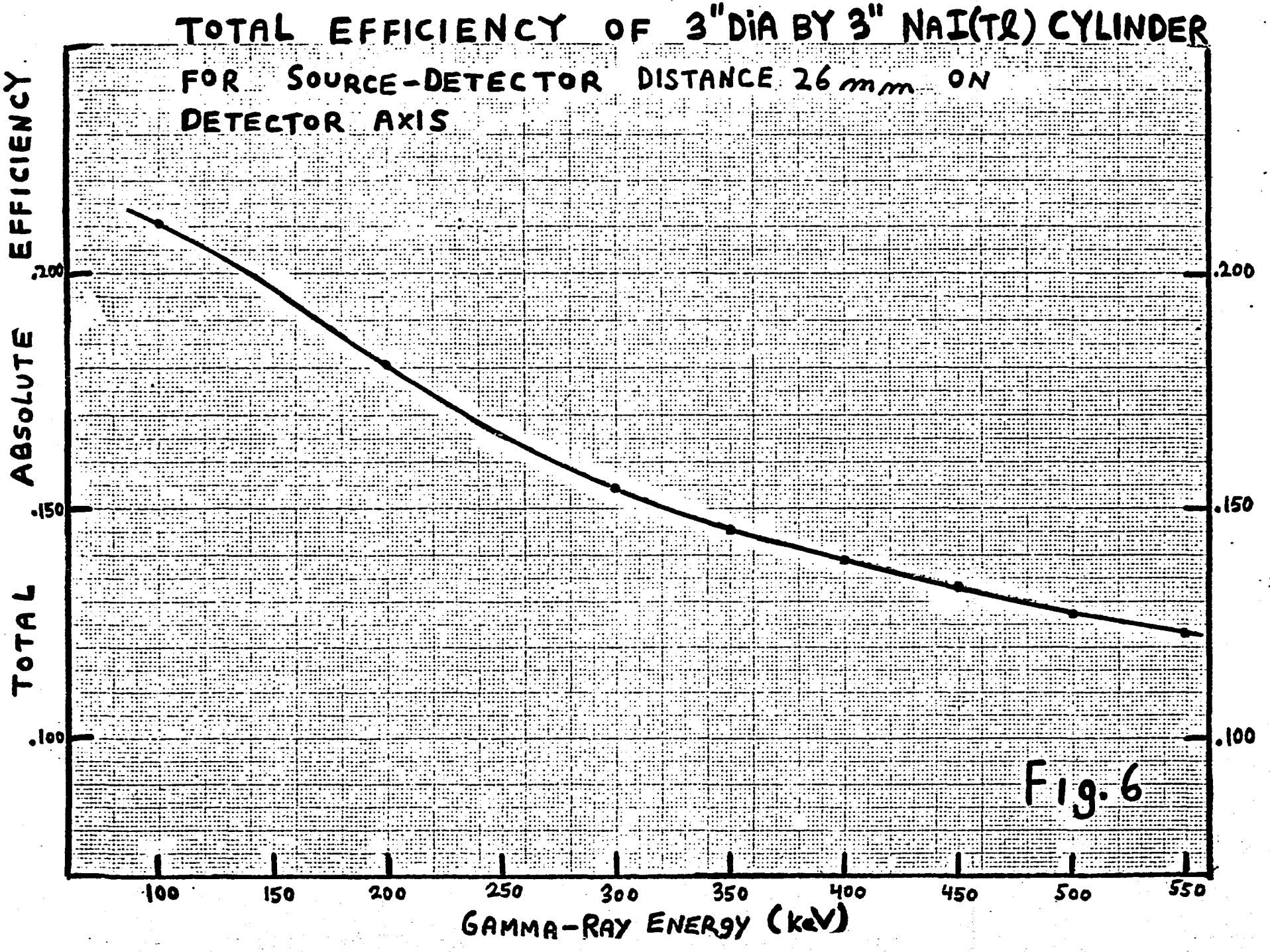
TOTAL EFFICIENCY OF 3"DIA BY 3" NaI(Tl) CYLINDER
FOR SOURCE-DETECTOR DISTANCE 26 mm ON DETECTOR AXIS
TOTAL ABSOLUTE EFFICIENCY
.200
.150
.100
100
150
200
250
300
350
400
450
500
550
GAMMA-RAY ENERGY (keV)

Fig. 6

PHOTOPEAK-TO-TOTAL RATIO
3" x 3" CYLINDER NaI(Tl)
EXPERIMENTAL GEOMETRY (I)
"IDEAL" GEOMETRY (II)

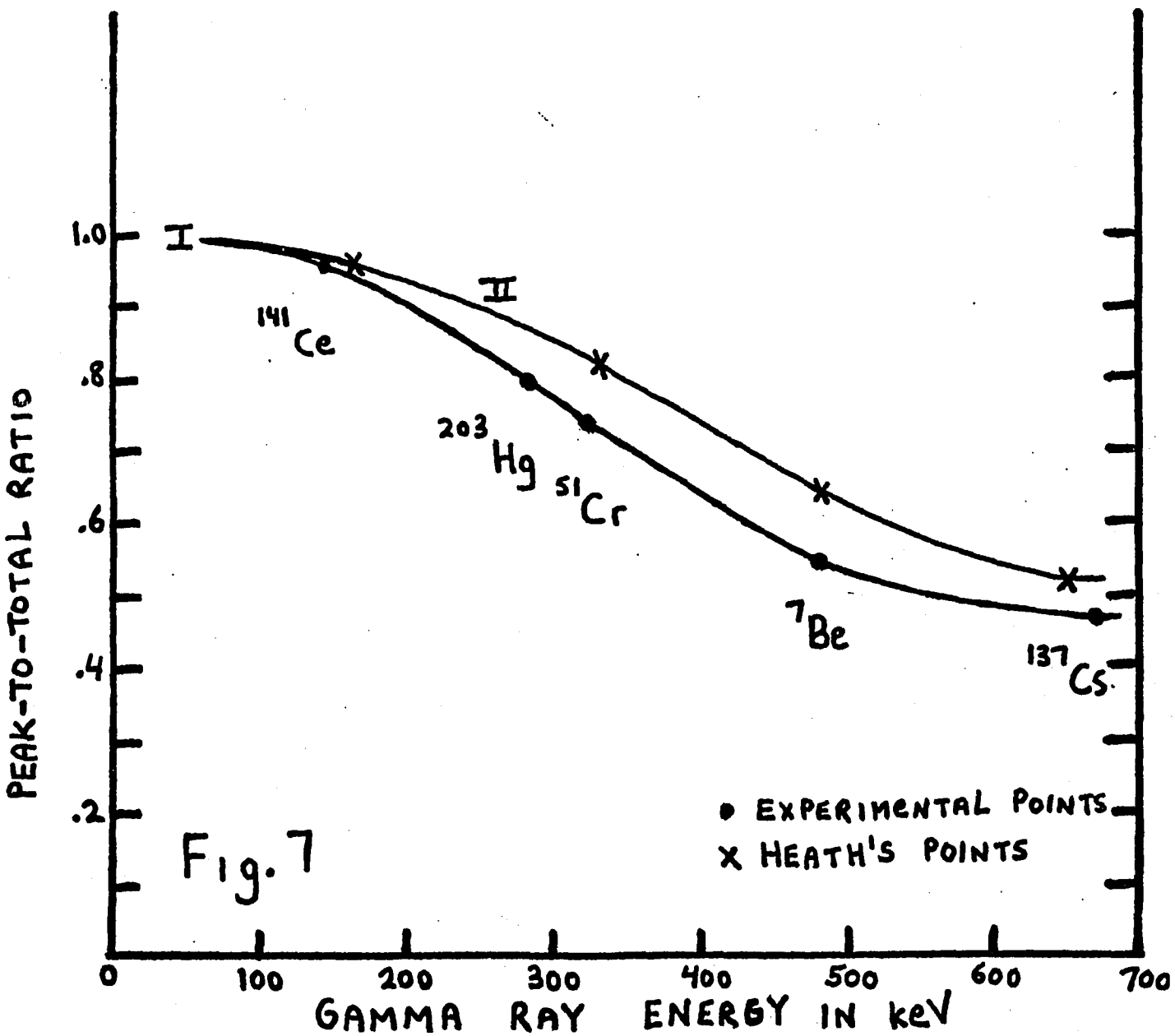

Fig. 7

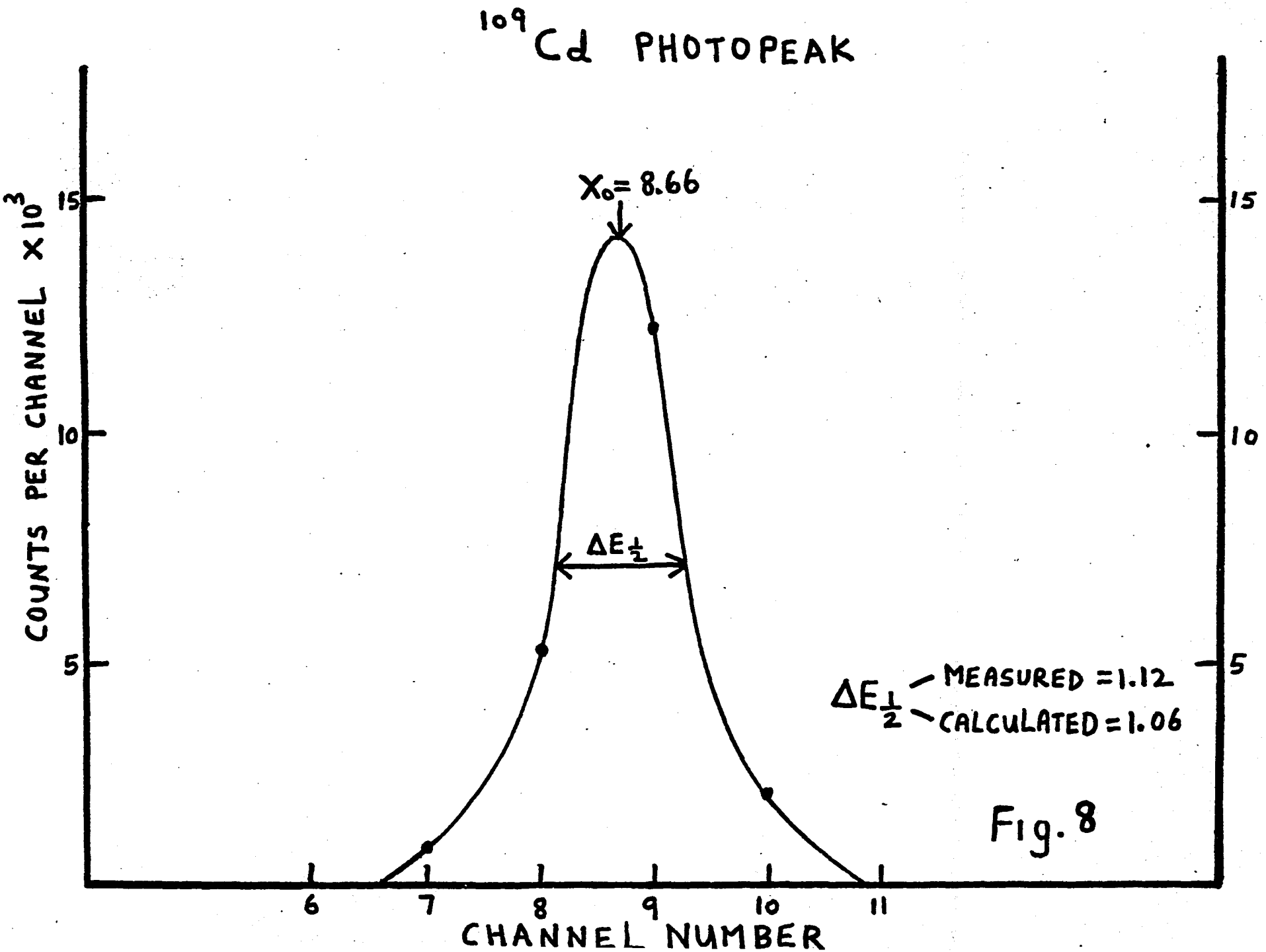
^{109}Cd PHOTOPEAK
$X_o = 8.66$
$\Delta E_{\frac{1}{2}}$
COUNTS PER CHANNEL $\times 10^3$
15
10
5
6
7
8
9
10
11
CHANNEL NUMBER
$\Delta E_{\frac{1}{2}}$ — MEASURED = 1.12
$\Delta E_{\frac{1}{2}}$ — CALCULATED = 1.06

Fig. 8

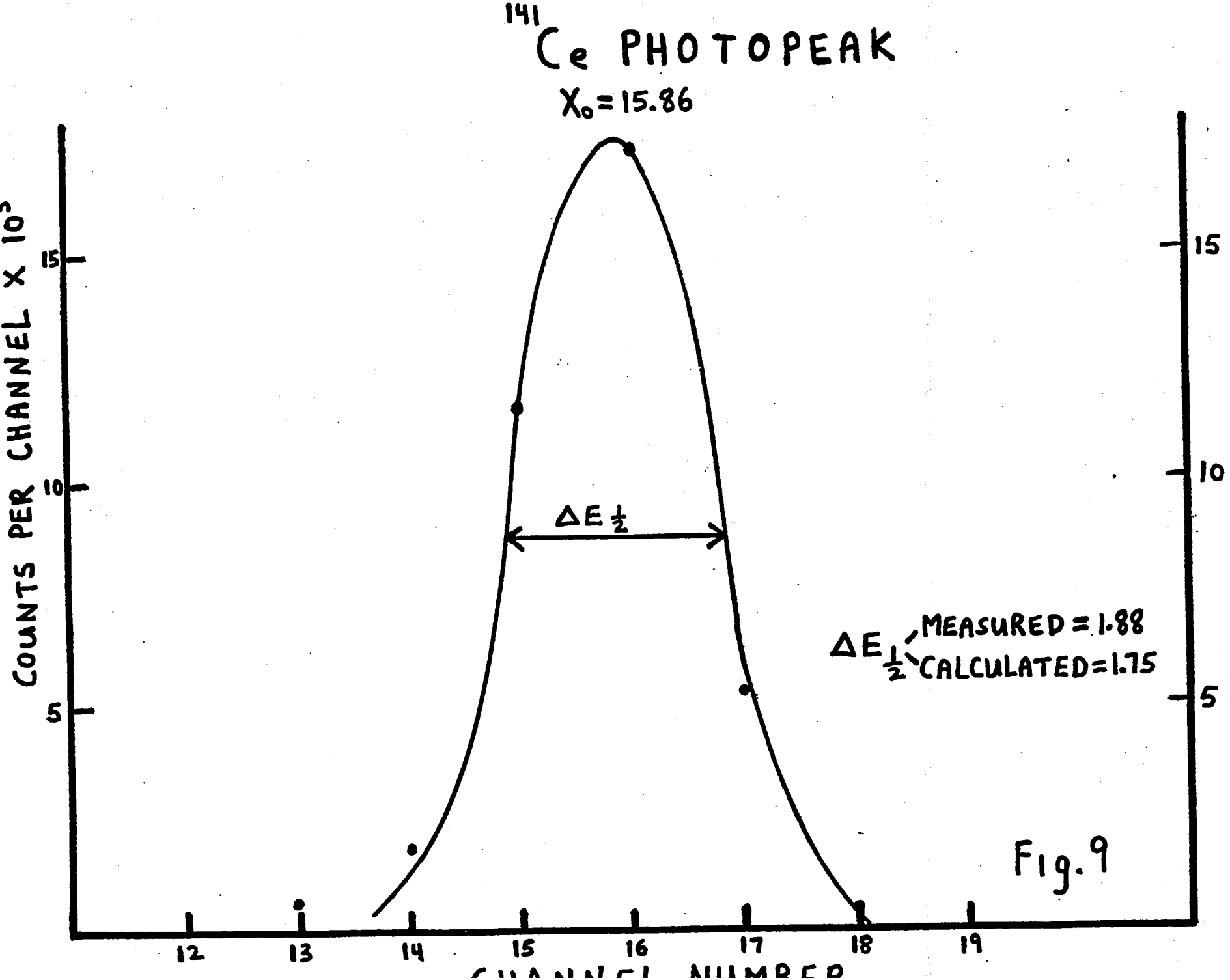
^{141}Ce PHOTOPEAK
$X_o = 15.86$
COUNTS PER CHANNEL X 10^3
15
10
5
$\Delta E_{\frac{1}{2}}$
$\Delta E_{\frac{1}{2}}$ MEASURED = 1.88
CALCULATED = 1.75
12
13
14
15
16
17
18
19
CHANNEL NUMBER

Fig. 9

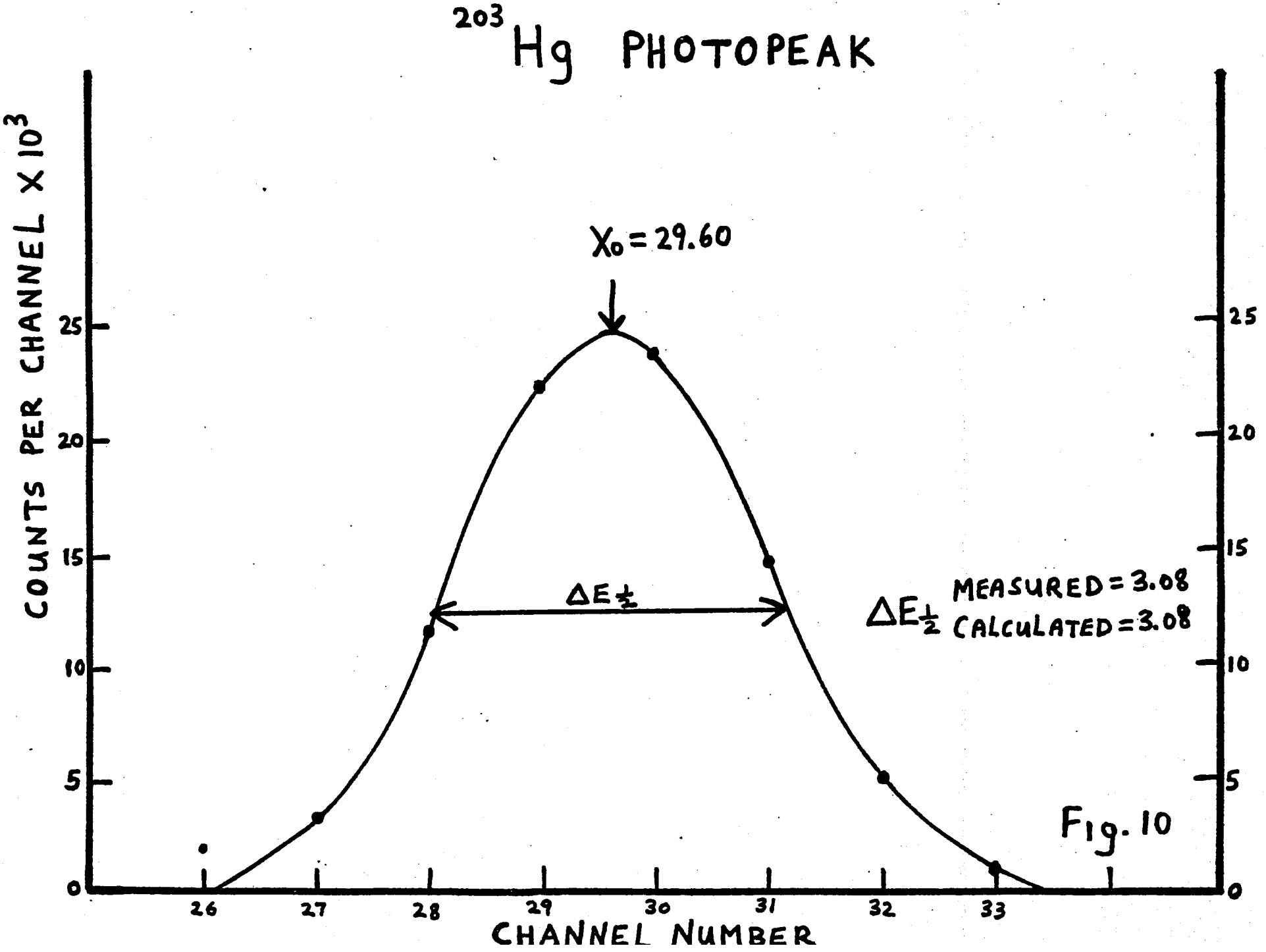
^{203}Hg PHOTOPEAK
$X_0 = 29.60$
$\Delta E_{\frac{1}{2}}$
$\Delta E_{\frac{1}{2}}$ MEASURED = 3.08
CALCULATED = 3.08
COUNTS PER CHANNEL X 10^3
CHANNEL NUMBER
0
5
10
15
20
25
26
27
28
29
30
31
32
33

Fig. 10

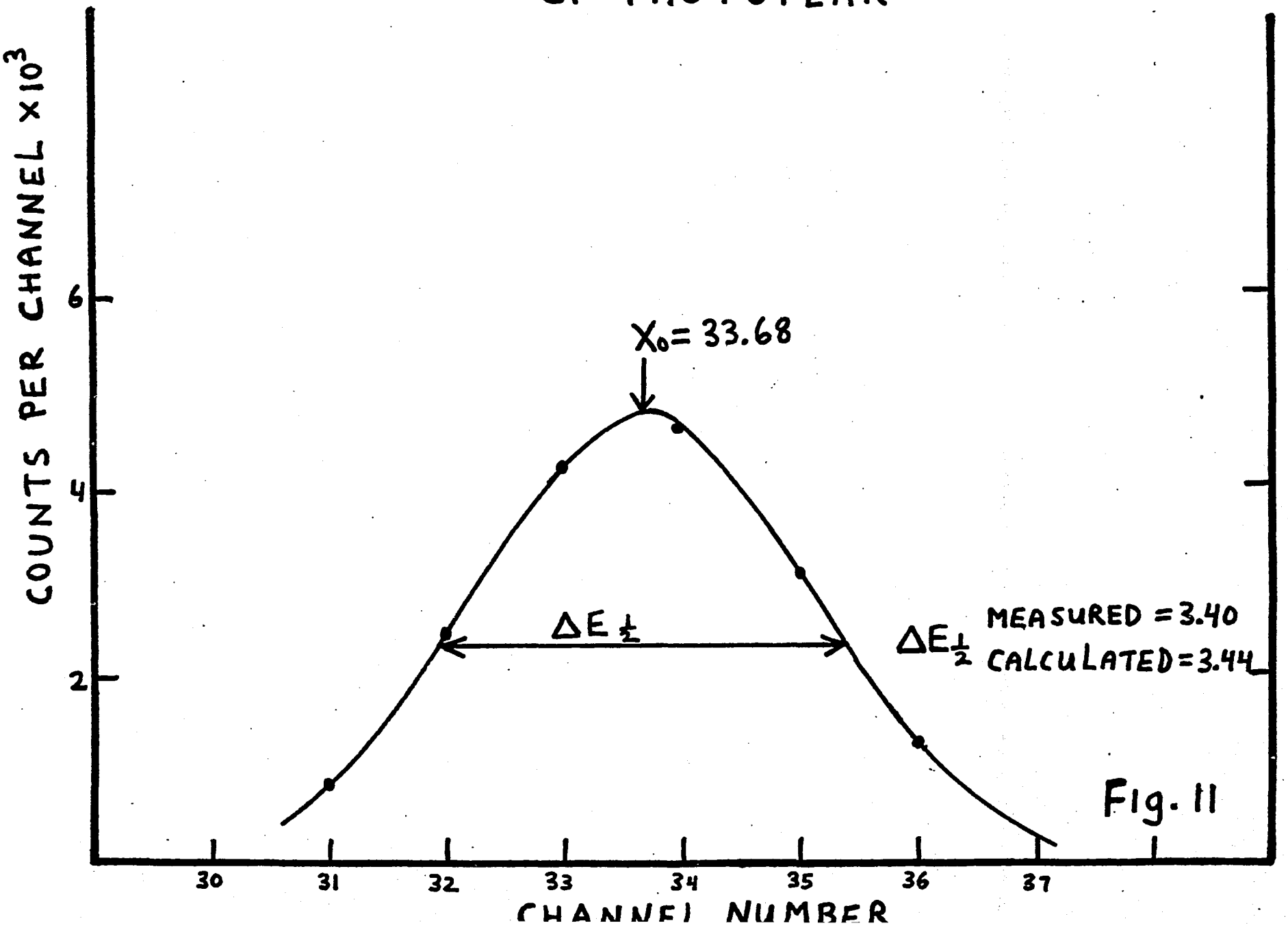
^{51}Cr PHOTOPEAK
COUNTS PER CHANNEL X10^3
6
4
2
X_0= 33.68
$\Delta E_{\frac{1}{2}}$
$\Delta E_{\frac{1}{2}}$
MEASURED = 3.40
CALCULATED = 3.44
30
31
32
33
34
35
36
37
CHANNEL NUMBER

Fig. 11

^{7}Be PHOTOPEAK

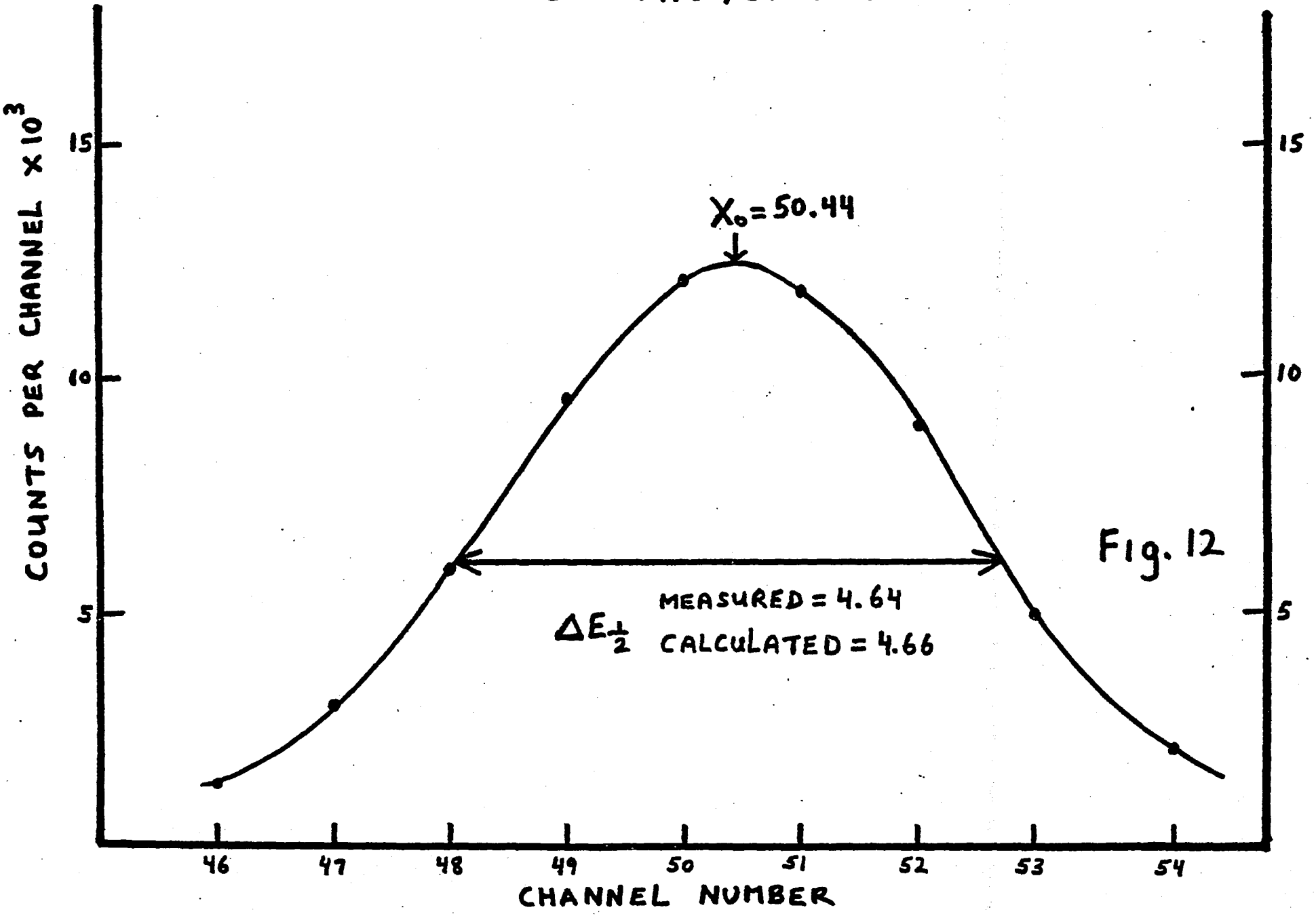

Fig. 12

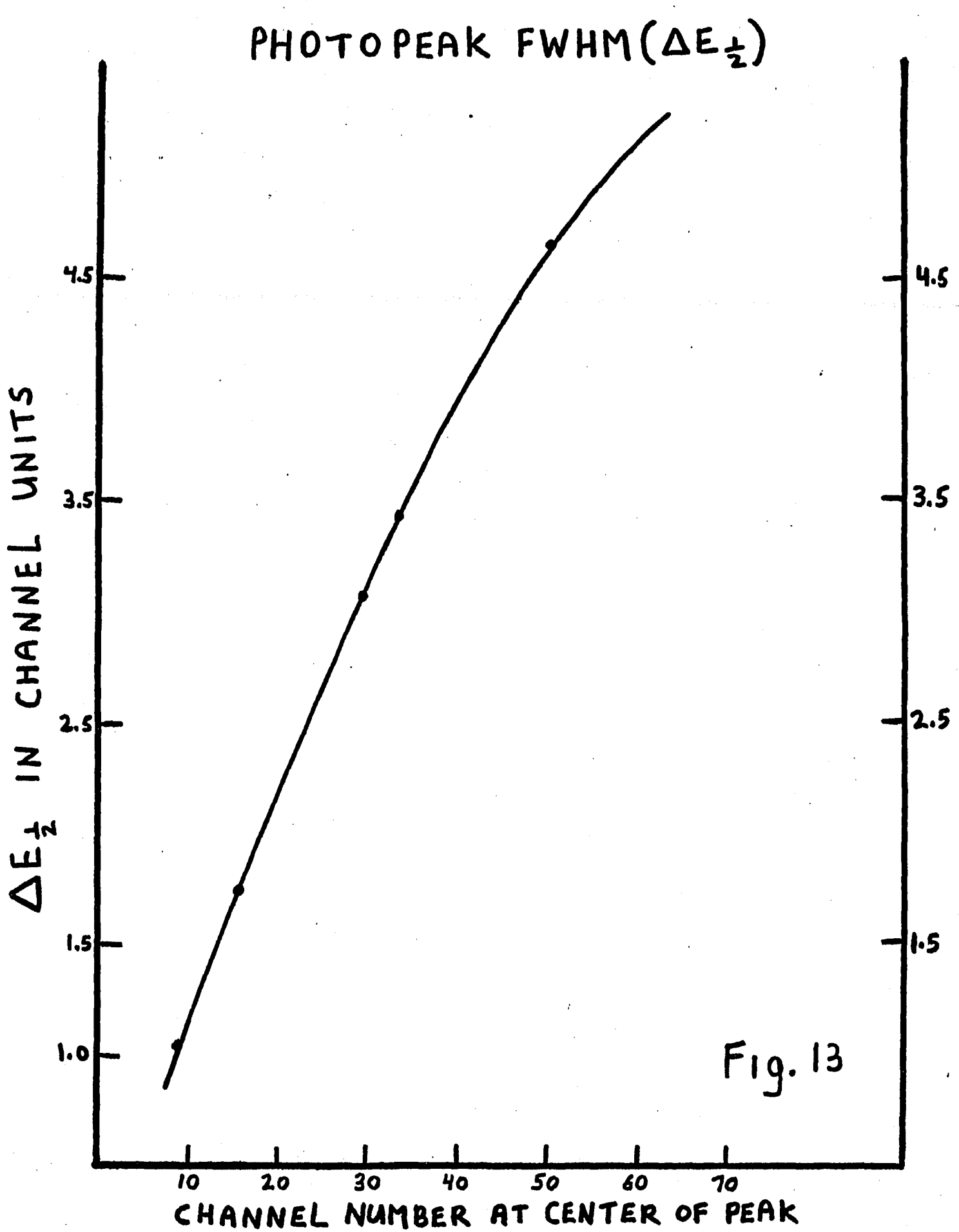
PHOTOPEAK FWHM ($\Delta E_{\frac{1}{2}}$)
$\Delta E_{\frac{1}{2}}$ IN CHANNEL UNITS
4.5
3.5
2.5
1.5
1.0
10
20
30
40
50
60
70
CHANNEL NUMBER AT CENTER OF PEAK

Fig. 13

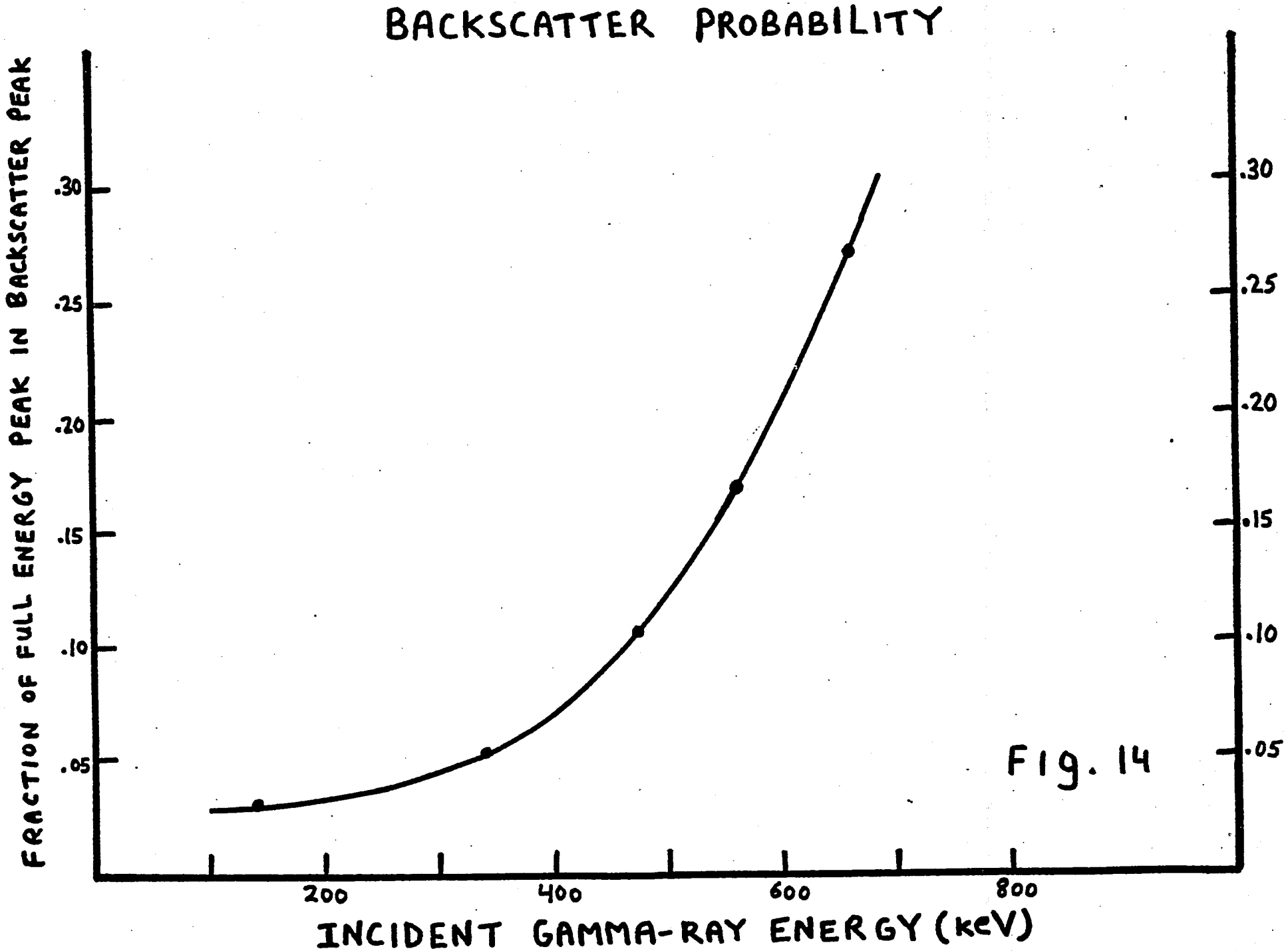
BACKSCATTER PROBABILITY
FRACTION OF FULL ENERGY PEAK IN BACKSCATTER PEAK
.30
.25
.20
.15
.10
.05
200
400
600
800
INCIDENT GAMMA-RAY ENERGY (keV)

Fig. 14

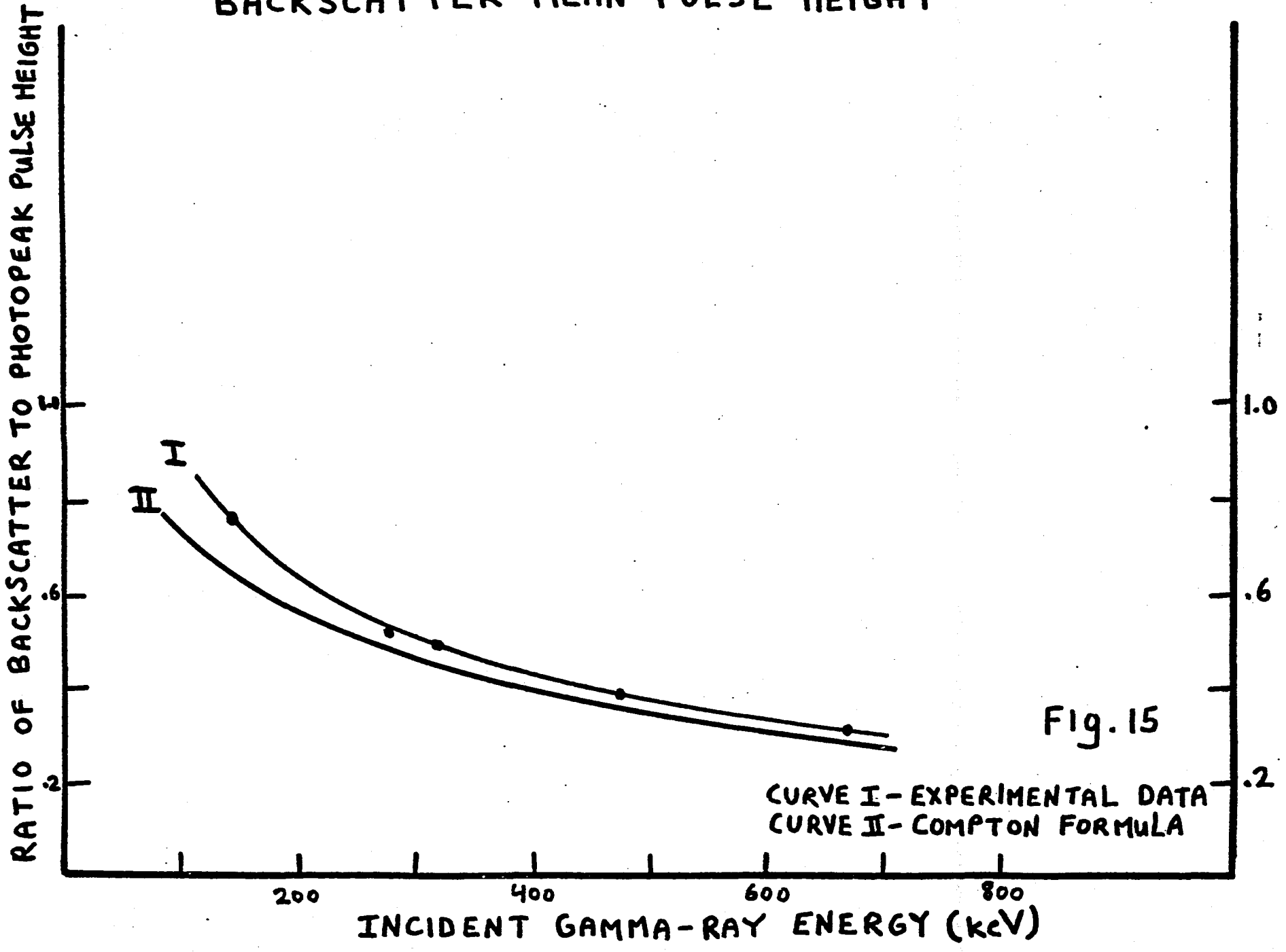
BACKSCATTER MEAN PULSE HEIGHT
RATIO OF BACKSCATTER TO PHOTOPEAK PULSE HEIGHT
1.0
.6
.2
I
II
200
400
600
800
INCIDENT GAMMA-RAY ENERGY (keV)
CURVE I - EXPERIMENTAL DATA
CURVE II - COMPTON FORMULA

Fig. 15

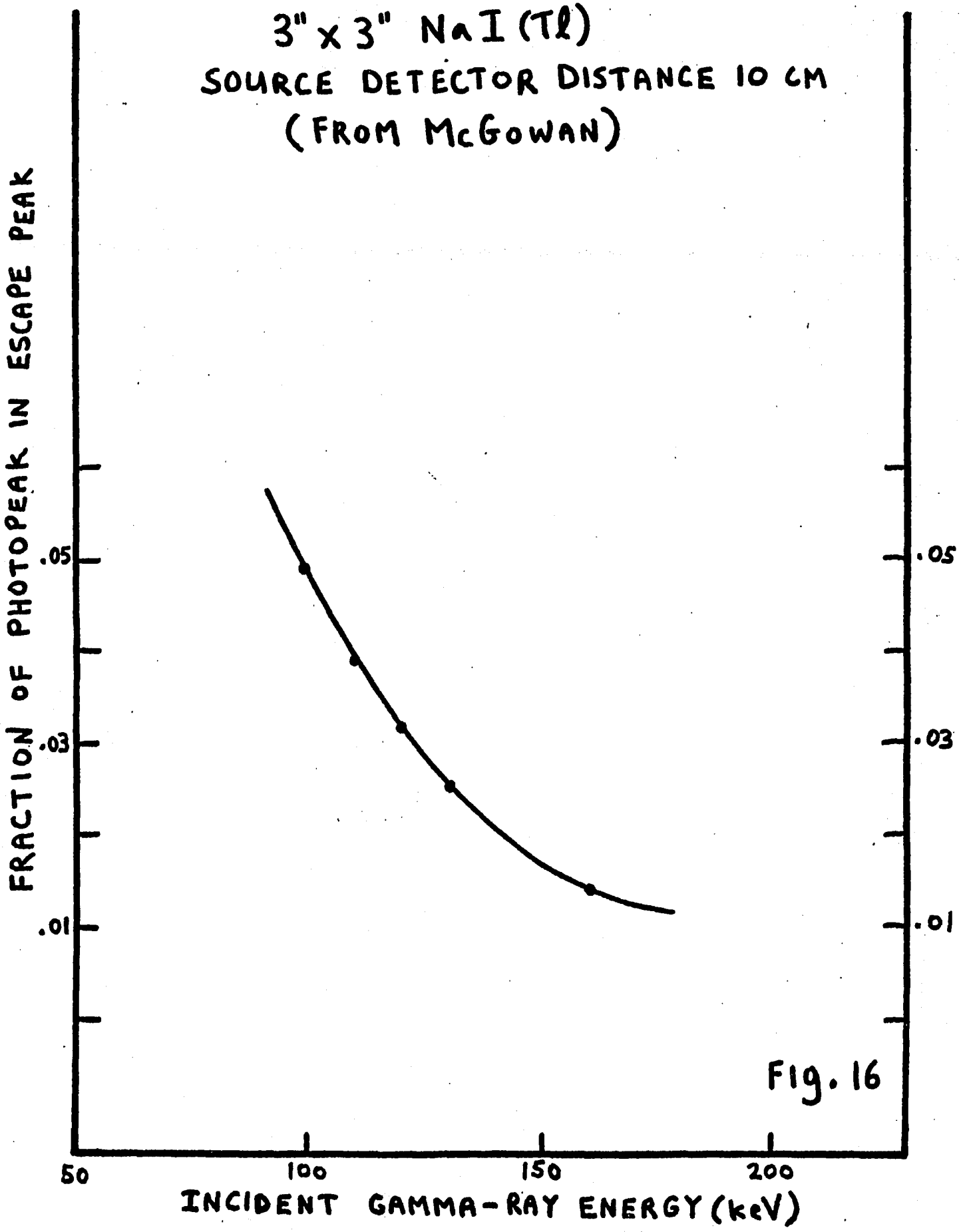
IODINE ESCAPE PROBABILITY
3" x 3" NaI (Tl)
SOURCE DETECTOR DISTANCE 10 CM
(FROM McGOWAN)
FRACTION OF PHOTOPEAK IN ESCAPE PEAK
.05
.03
.01
50
100
150
200
INCIDENT GAMMA-RAY ENERGY (keV)

Fig. 16

TABLE I
PHOTOPEAK ELEMENTS OF RESPONSE MATRIX

ROWS										COLUMNS
9 -			131	738	131					13
10 -		1	152	694	152	1				14
11 -		3	172	650	172	3				15
12 -		5	191	608	191	5				16
13 -		8	200	580	200	8				17
14 -		12	215	546	215	12				18
15 -		17	220	525	220	17				19
16 -		23	231	492	231	23				20
17 -		30	235	469	235	30				21
18 -	2	37	239	444	239	37	2			22
19 -	3	44	241	425	241	44	3			23
20 -	4	50	242	409	242	50	4			24
21 -	5	56	242	393	242	56	5			25
22 -	7	63	241	378	241	63	7			26
23 -	9	68	240	365	240	68	9			27
24 -	11	74	239	352	239	74	11			28
25 -	14	79	237	341	237	79	14			29
26 -	16	84	235	330	235	84	16			30
27 -	2	20	86	232	319	232	86	20	2	31
28 -	3	15	97	230	311	230	97	15	3	32
29 -	3	23	96	227	302	227	96	23	3	33
30 -	6	26	99	226	291	226	99	26	6	34
31 -	5	28	103	221	286	221	103	28	5	35
32 -	6	31	105	219	280	219	105	31	6	36
33 -	7	33	107	216	272	216	107	33	7	37

CONTINUATION TABLE I

ROWS	COLUMNS 29	30	31	32	33	34	35	36	37	38	
34	1	8	36	109	213	266	213	109	36	8	1
35	1	9	39	111	210	260	210	111	39	9	1
36	2	10	41	113	207	254	207	113	41	10	2
37	2	11	43	114	205	248	205	114	43	11	2
38	3	13	46	117	201	243	201	117	46	13	3
39	3	14	48	117	200	238	200	117	48	14	3
40	4	15	50	118	197	234	197	118	50	15	4

40 41 42 43 44 45

TABLE II

COMPTON ELEMENTS OF RESPONSE MATRIX

	i →														
	1	2	3	4	5	6	7								
9 –	.459	.459	.459	.459	.459	.459	.459								
10 –	.606	.606	.606	.606	.606	.606	.606	8							
11 –	.523	.523	.523	.523	.523	.523	.523	.523	9						
12 –	.575	.575	.575	.575	.575	.575	.575	.575	.575	10					
13 –	.610	.610	.610	.610	.610	.610	.610	.610	.610	.610	11				
14 –	.639	.639	.639	.639	.639	.639	.639	.639	.639	.639	.639	12			
15 –	.659	.659	.659	.659	.659	.659	.659	.659	.659	.659	.659	.659	13		
16 –	.905	.846	.818	.810	.764	.755	.747	.739	.734	1.046	.608	.584	.564	14	
17 –	.992	.945	.911	.899	.853	.837	.831	.835	.887	.822	.758	.728	.691	.656	
18 –	1.145	1.097	1.060	1.041	.988	.971	.965	.982	.991	.983	.928	.888	.842	.789	15
19 –	1.211	1.173	1.035	1.104	1.068	1.033	1.025	1.039	1.054	1.077	1.051	1.026	.973	.917	.861
20 –	1.268	1.240	1.198	1.167	1.144	1.084	1.08	1.078	1.117	1.129	1.15	1.12	1.101	1.06	.976
21 –	1.20	1.181	1.138	1.114	1.098	1.034	1.026	1.022	1.044	1.066	1.093	1.097	1.079	1.058	1.025
22 –	1.217	1.205	1.61	1.144	1.117	1.074	1.044	1.04	1.039	1.088	1.096	1.127	1.123	1.117	1.085
23 –	1.226	1.221	1.173	1.163	1.126	1.104	1.052	1.05	1.049	1.076	1.105	1.13	1.147	1.147	1.147
24 –	1.232	1.232	1.182	1.182	1.133	1.133	1.058	1.058	1.055	1.055	1.116	1.116	1.162	1.162	1.17
25 –	1.237	1.237	1.194	1.189	1.148	1.138	1.084	1.062	1.062	1.061	1.093	1.125	1.145	1.174	1.179
26 –	1.243	1.243	1.206	1.197	1.166	1.145	1.114	1.069	1.068	1.067	1.067	1.135	1.135	1.176	1.186
27 –	1.384	1.384	1.346	1.335	1.299	1.275	1.241	1.190	1.190	1.190	1.190	1.268	1.268	1.315	1.327

j ↓

															15
19	1.211	1.173	1.035	1.104	1.068	1.033	1.025	1.039	1.054	1.077	1.051	1.026	.973	.917	.861
20	1.268	1.240	1.198	1.167	1.144	1.084	1.08	1.078	1.117	1.129	1.15	1.12	1.101	1.06	.976	.923	16
21	1.20	1.181	1.138	1.114	1.098	1.034	1.026	1.022	1.044	1.066	1.093	1.097	1.079	1.058	1.025	.930
22	1.217	1.205	1.61	1.144	1.117	1.074	1.044	1.04	1.039	1.088	1.096	1.127	1.123	1.117	1.085	1.063
23	1.226	1.221	1.173	1.163	1.126	1.104	1.052	1.05	1.049	1.076	1.105	1.13	1.147	1.147	1.147	1.102
24	1.232	1.232	1.182	1.182	1.133	1.133	1.058	1.058	1.055	1.055	1.116	1.116	1.162	1.162	1.17	1.17
25	1.237	1.237	1.194	1.189	1.148	1.138	1.084	1.062	1.062	1.061	1.093	1.125	1.145	1.174	1.179	1.189
26	1.243	1.243	1.206	1.197	1.166	1.145	1.114	1.069	1.068	1.067	1.067	1.135	1.135	1.176	1.186	1.199
27	1.384	1.384	1.346	1.335	1.299	1.275	1.241	1.190	1.190	1.190	1.190	1.268	1.268	1.315	1.327	1.345
28	1.374	1.374	1.343	1.329	1.305	1.268	1.259	1.205	1.205	1.187	1.183	1.223	1.263	1.275	1.324	1.324
29	1.369	1.369	1.343	1.326	1.314	1.264	1.264	1.196	1.18	1.179	1.179	1.179	1.262	1.262	1.30	1.324
30	1.431	1.431	1.409	1.388	1.388	1.322	1.322	1.277	1.233	1.233	1.234	1.234	1.278	1.322	1.322	1.399
31	1.621	1.621	1.576	1.508	1.508	1.419	1.394	1.380	1.322	1.322	1.344	1.359	1.359	1.471	1.471	1.506
32	1.598	1.598	1.552	1.444	1.444	1.361	1.306	1.306	1.258	1.253	1.265	1.314	1.314	1.373	1.433	1.433
33	1.576	1.576	1.538	1.394	1.394	1.321	1.274	1.224	1.202	1.188	1.188	1.255	1.271	1.271	1.397	1.397
34	1.611	1.611	1.567	1.993	1.393	1.324	1.221	1.221	1.208	1.20	1.20	1.283	1.304	1.304	1.436	1.436
35	1.586	1.586	1.567	1.390	1.390	1.359	1.238	1.238	1.237	1.234	1.234	1.277	1.341	1.341	1.409	1.476
36	1.480	1.480	1.480	1.330	1.310	1.310	1.210	1.190	1.190	1.20	1.20	1.200	1.260	1.30	1.30	1.37
37	1.490	1.490	1.490	1.37	1.34	1.34	1.270	1.230	1.230	1.240	1.260	1.26	1.280	1.37	1.37	1.37
38	1.480	1.480	1.480	1.380	1.340	1.340	1.290	1.250	1.250	1.250	1.280	1.280	1.280	1.376	1.400	1.400
39	1.460	1.460	1.460	1.240	1.33	1.33	1.32	1.26	1.26	1.26	1.30	1.31	1.31	1.36	1.43	1.43
40	1.45	1.45	1.45	1.29	1.33	1.33	1.33	1.28	1.28	1.28	1.31	1.33	1.33	1.33	1.46	1.46

17																
.889	18															
.945	.916	19														
1.092	.95	.935	20													
1.114	1.114	.949	.949	21												
1.176	1.132	1.116	.962	.962	22											
1.207	1.184	1.150	1.115	.974	.974											
1.357	1.332	1.294	1.253	1.092	1.092											
1.355	1.359	1.321	1.295	1.234	1.09	23 1.09										
1.332	1.364	1.364	1.313	1.30	1.217	1.09	24 1.09									
1.389	1.410	1.431	1.431	1.369	1.369	1.258	1.147	25 1.147								
1.557	1.557	1.645	1.663	1.635	1.508	1.508	1.379	1.293	26 1.293	27 1.271						
1.506	1.524	1.589	1.673	1.673	1.588	1.460	1.46	1.328	1.271	1.271						
1.416	1.494	1.494	1.569	1.68	1.68	1.522	1.416	1.416	1.284	1.261	28 1.261					
1.456	1.639	1.539	1.616	1.729	1.729	1.54	1.414	1.419	1.291	1.261	1.261	29 1.199				
1.476	1.536	1.576	1.576	1.648	1.679	1.679	1.417	1.352	1.352	1.212	1.197	1.199				
1.43	1.43	1.47	1.52	1.52	1.53	1.55	1.55	1.48	1.22	1.22	1.20	1.07	30 1.07	31 1.04		
1.50	1.50	1.50	1.58	1.59	1.59	1.57	1.54	1.54	1.41	1.19	1.19	1.17	1.04	1.04	32 .99	
1.419	1.54	1.54	1.65	1.62	1.62	1.62	1.52	1.51	1.51	1.29	1.15	1.15	41	.99	.99	33 .95
1.42	1.57	1.57	1.67	1.62	1.65	1.65	1.62	1.47	1.47	1.47	1.17	1.1	1.1	1.04	.95	.95
1.46	1.53	1.6	1.6	1.6	1.68	1.68	1.68	1.56	1.44	1.44	1.44	1.05	1.05	1.05	.98	.9

34
.9

VII. ^{204}Tl SOURCE INTENSITY MEASUREMENTS

The intensity of the ^{204}Tl source was determined from the ^{204}Hg K x-ray emission rate. Two methods were used to obtain this value, based on separate measurements taken on the Ge(Li) spectrometer and the NaI(Tl) detector. The two values were weighted and averaged to give the final result.

In the first measurement, data was obtained with the Ge(Li) spectrometer, and the relation developed in the section on the System Coincidence Efficiency for the efficiency of the Ge(Li) spectrometer was applied here. The efficiency of the NaI(Tl) detector, $\epsilon_{NaI}^{Hg\,Kx}$, was 0.07 $\pm$ 0.002, and was taken from the tables of Heath.[1] This value was checked using calibrated sources of ^{57}Co and ^{133}Ba. The importance of taking tese extra measurements need not be underestimated--the intensity of the thallium source, and consequently the magntiude of the IB effect, depended on an accurate knowledge of $\epsilon_{GeLi}^{Hg\,Kx}$ and $\epsilon_{NaI}^{Hg\,Kx}$.

The remaining terms in the expression of $\epsilon_{GeLi}^{Hg\,Kx}$) i.e., N_{NaI}^{Kx} and N_{GeLi}^{Kx}, were obtained from singles spectra collected in the ^{207}Bi coincidence measurement. The N_{GeLi}^{Kx} was corrected for room background, for multichannel analyzer dead-time (6%), and for attenuation in the 3 mm beryllium and 0.015 mm copper foils, which were determined under separate measurements and amounted to 5% to 7%, respectively. The value for N_{NaI}^{Kx} was corrected for background, which consisted primarily of Compton scattering of the 570-keV gamma rays. The attenuation through the 1.5 mm-thick aluminum win-

dow of the NaI(Tl) detector and the 2 mm-thick beryllium sheet positioned between the source and tin collimator were also included in the value of N_{NaI}^{Kx} . These corrections were 8% and 3% respectively, and were measured values. The Ge(Li) and the NaI(Tl) detector singles spectra of ^{207}Bi used in this calculation are included in the section on the System Coincidence Efficiency. The intensities of the Pb K x rays in these spectra were, after corrections:

$$N_{NaI}^{PbKx} = 917.3 \text{ counts/sec}$$

$$N_{GeLi}^{PbKx} = 425.5 \text{ counts/sec}$$

Thus $\epsilon_{GeLi}^{Kx} = (.07)\frac{424.5}{917.3} = 0.0324 \pm 0.0021$.

It is convenient to introduce the following terms to compute the thallium source intensity. Let η_{Cu} be the correction for absorption in copper; η_{Be} be the correction for absorption in beryllium; τ_d denotes the deadtime of the MCA; $S_{K\alpha} = \sum_i C_i$ is the total number of counts, where C_i is the number of counts in channels $i=6$ to $i=23$. These channels define the lower and upper bounds of the ^{203}Hg $K\alpha$ x rays. Also $S_{K\beta} = \sum_{i=40}^{i=58} C_i$ is the number of counts under the $K\beta$ peak. Finally, we use the term B_K to represent the background in these channel ranges.

With these definitions, and using the Ge(Li) spectrum of ^{204}Tl shown in Figure 1, we get the following result for I_{HgKx} , the Hg K x-ray intensity of the source:

$$I_{HgKx} = \frac{(S_{K\alpha} - B_{K\alpha}) + (S_{K\beta} - B_{K\beta})}{\epsilon_{GeLi}\,\eta_{Be}\,\eta_{Cu}\,(1-\tau_d)}$$

$$= \frac{622 \pm 30}{.0324 \pm .0021}$$

$$= 19{,}198 \pm 1{,}550 \text{ sec}^{-1} .$$

The second method to obtain the K x-ray source intensity used spectra taken with the Harshaw 3" X 3" scintillation detector. In the course of the experiment, singles spectra of the thallium source were taken on the NaI(Tl) detector before each experimental run. In general this averaged about one per day. Several of these spectra were combined and the total spectrum is shown in Figure 2. On the basis of Heath's calculated values, we obtain $\epsilon_{NaI}^{HgKx} = 0.23 \pm 0.01$ for 74-keV photons at a source-detector distance of 26 mm. Using quantities defined in the previous discussion, with the understanding that they now apply to the NaI(Tl) detector and the absorbers inserted between the source and this detector, we obtain:

$$I_{HgKx} = \frac{N_{NaI}^{HgKx}}{\epsilon_{NaI}^{Kx}\,\eta_{Al}\,\eta_{Be}\,(1-\tau_d)}$$

In the determination of N_{NaI}^{HgKx}, the total number of counts under the Hg K x-ray peak, the summation was taken from channels 5 to 10 (see Figure 2). The x rays lie on a sizable background, which is internal bremsstrahlung accompanying orbital electron capture and beta decay, and external bremsstrahlung produced in stopping the beta particles in the beryllium absorbers surrounding the source. The bremsstrahlung background was subtracted from the x-ray peak by

assuming it behaved linearly in the region of the x rays. The room background also was subtracted from the x rays by this process.

Using the values $N_{NaI}^{HgKx} = 2933 \pm 128$ counts-sec^{-1}; $\epsilon_{NaI}^{Kx} = 0.23$; $\eta_{Al} = .92$; $\eta_{Be} = .97$; $\tau_d = .20$, we get for the Hg K x-ray intensity:

$$I_{HgKx} = 17,862 \pm 1100 \text{ - sec}^{-1} .$$

The two independently measured values were weighted by σ^{-2}, where σ is the standard deviation, and averaged to give a final result of:

$$I_{HgKx} = 18,309 \pm 897 \text{ - sec}^{-1} .$$

This is the K-x ray emission rate.

REFERENCES

(1) R. L. Heath, USAEC Report No. 100-16880-1, 1964 (unpublished).

SINGLES SPECTRUM OF ^{204}Hg KX RAYS ACCOMPANYING ELECTRON CAPTURE IN ^{204}Tl, TAKEN ON Ge(Li) DETECTOR

Fig. 1

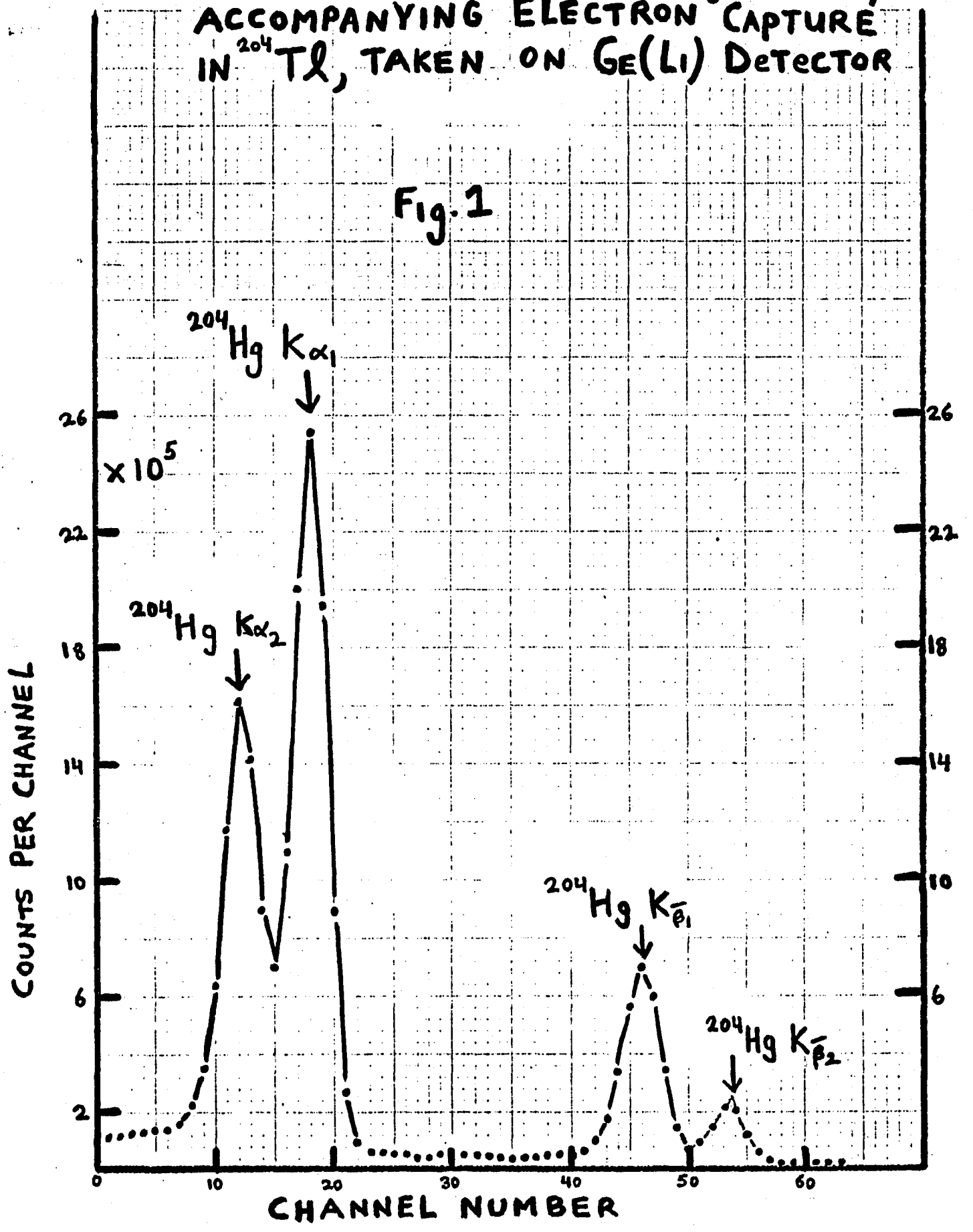

3"x3" NaI(Tl) DETECTOR

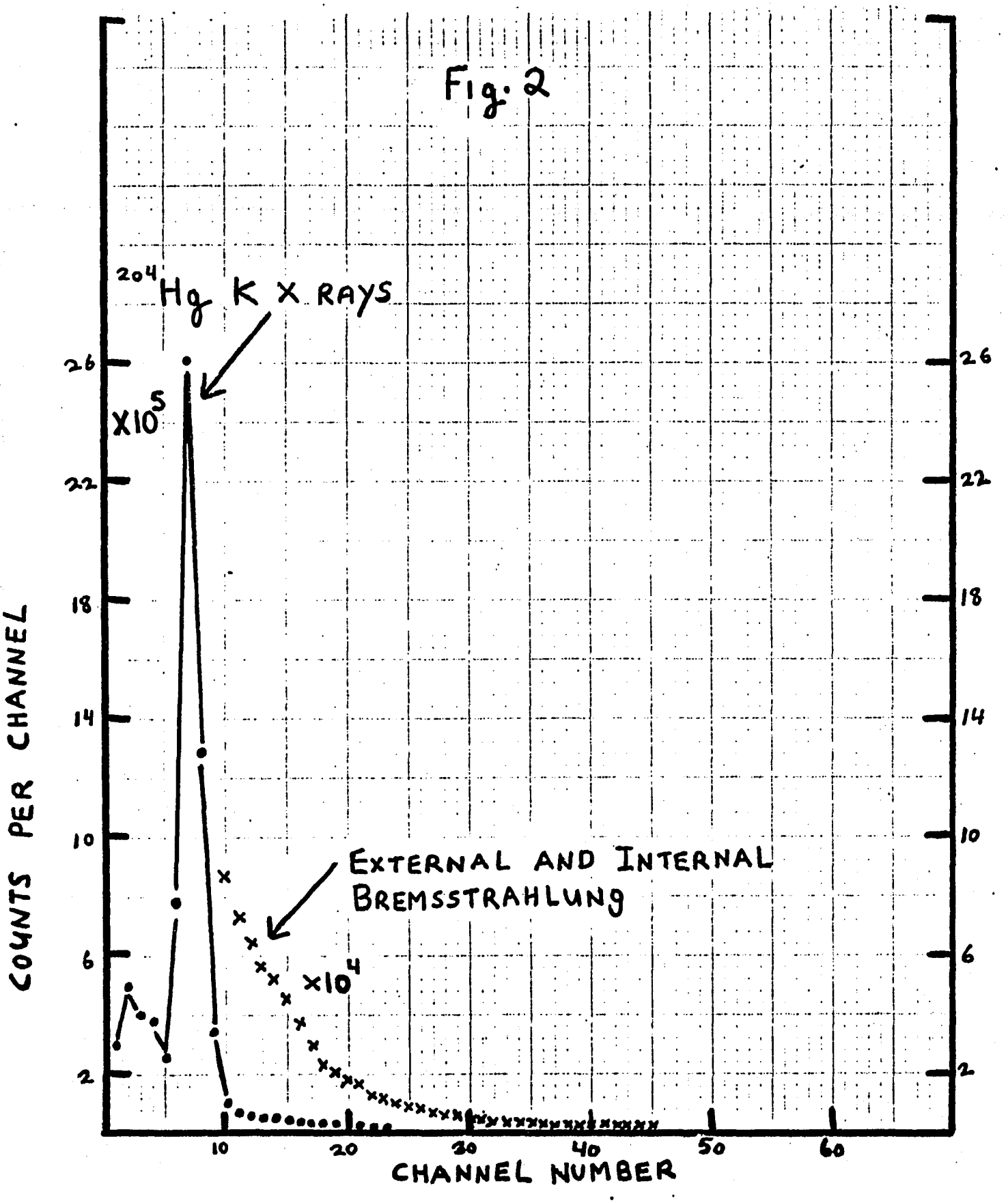

VIII. DECTECTOR CALIBRATIONS

I. NaI(Tl)

The sources used in the crystal calibration, and their corresponding energies, are presented in Table I.

The pulse-height distributions of the calibration sources are included in the section on the NaI(Tl) Detector Response Matrix. In the present discussion the half-width ($\Delta E_{\frac{1}{2}}$) values are used to analyze the errors in the calibration line, whereas in the determination of the response matrix they are used to obtain the empirical relation between $\Delta E_{\frac{1}{2}}$ and E. The mean photopoeak positions X_o and the peak half-widths $\Delta E_{\frac{1}{2}}$ of the califbration sources are presented in Table II.

The mean channels X_o of the calibration spectra were plotted against calibration energies (see Fig. 1), and as expected, the data behaved linearly in the energy range under consideration (15-600 keV). A least-squares routine was used to determine the equation of the line of best fit. On the basis of these results, the energy, and error in energy corresponding to each channel of the NaI(Tl) detector spectrum were determined.

For each pair of values E_i, X_{oi}, where X_{oi} = mean photopeak channel corresponding to an incident photon with energy E_i, the energy is very accurately known, while the channel position was weighted by W_i, where $W_i = 1/\sigma_i^2$ and σ_i is the standard error in channel X_{oi}. If we assume an equation of the form

$$X = ME + b$$

then according to the prescription of least squares, the values of the parameters M and b which best fit the data, where M = slope and b = channel corresponding to zero energy, are those which minimize the expression

$$\sum_i (X_i - ME_i - b)^2 W_i \ .$$

Now from counting statistics, for a gaussian probability distribution, the standard error in the mean of a sample, σ_{im}, is related to the standard error of the sample, σ_i, by $\sigma_{im}^2 = \sigma_i^2/N$, where N represents the population of the sample. Thus the standard error in the channel X_i, corresponding to the energy E_i, is the standard error in the mean channel position X_{oi}. Thus the standard error in the channel positions can be determined from the data of Table II. In the present study the assumption was made that N was equal, although arbitrary, for all calibration sources. This is a reasonable assumption and is equivalent to specifying that all photopeaks integrate to the same intensity. In the actual calculations, N cancels, and only the relative weighting of each channel (σ_i^{-2}) survives. Thus for reference one may refer to Table II for the errors in the channel positions, bearing in mind that these are relative, not absolute, values.

The result of the least squares procedure yields the following expressions for M and b:

$$M = \frac{(\sum W_i E_i \sum W_i x_i) - (\sum W_i E_i x_i \sum W_i)}{(\sum W_i E_i)^2 - (\sum W_i E_i \sum W_i)}$$

$$= 0.108$$

$$b = \frac{(\sum W_i E_i x_i \sum W_i E_i) - (\sum W_i E_i^2 \sum W_i x_i)}{(\sum W_i E_i)^2 - (\sum W_i E_i^2 \sum W_i)}$$

$$= -0.587$$

Setting $M' = \frac{1}{M}$ and $b' = -\frac{b}{M}$, we obtain

$$E = M' x + b' = 9.26 x + 5.43$$

In the next step we determine the effect that errors in the measurements of the pulse heights of the calibration sources have on M' and b'. From the theory of errors we can use the following relation to predict the standard deviation in M and b:

$$\sigma_M^2 = \sum \left(\frac{\partial M}{\partial x_i}\right)^2 \sigma_{x_i}^2 ,$$

where

$$\sigma_{x_i}^2 = \sigma_i^2 / N , \quad W_i = 1/\sigma_{x_i}^2$$

and

$$\frac{\partial M}{\partial x_i} = \frac{W_j (\sum W_i E_i) - W_j E_j (\sum W_i)}{(\sum W_i E_i)^2 - (\sum W_i E_i^2 \sum W_i)}$$

and

$$\sigma_M^2 = \sum \left\{ \frac{(\sum E_i \sigma_i^{-2})^2 - (\sum \sigma_i^{-2}) E_j}{(\sum E_i \sigma_i^{-2})^2 - (\sum E_i^2 \sigma_i^{-2} \sum \sigma_i^{-2})} \right\}^2$$

where terms involving N cancel. Using the values for E_i, σ_i from Table I and Table II, we get

$$\sigma_M = 3.77 \times 10^{-3}$$

But

$$\sigma_{M'}^2 = \sigma_M^2 / M^4 \qquad \text{and so} \quad \sigma_{M'} = 0.035$$

Thus there is an uncertainty of $\approx$ 0.4% in the slope.

A similar calculation on b' yields

$$\sigma_b = 0.640$$

But

$$\sigma_{b'}^2 = \sigma_b^2 / M^2 + (b/M^2)^2 \sigma_M^2$$

$$\sigma_{b'} = 5.9 \text{ keV}.$$

Combining these results we obtain the following expression for the uncertainty in E:

$$\sigma_E^2 = (E - 5.43)^2 (.000142) + 35.036$$

$$\approx 42$$

$$\sigma_E \approx 6.5 \text{ keV}.$$

Thus for energies less than 700 keV, the error in E is primarily due to the error in energy for zero pulse height.

These results are based on statistical arguments and do not include the possibility of systematic errors, such as zero level drift, gain change, fluctuations in channel widths, and other electronics instabilities. Most of these time-dependent effects averaged out in the course of data collection. The detectors were calibrated twice during the experiment, with no change found. In addition to this, both before

and after each period of taking coincidence data (almost every 24 hours) a ^{207}Bi source was used to check for changes in gain and zero level. Data was rejected if peak positions changed by more than one channel (about a 2% change).

II. Ge(Li) DETECTOR

The calibration of the Ge(Li) detector was carried out analogously to the NaI(Tl) detector. The K_{α_1} and K_{α_2} x rays of lead and mercury from ^{207}Bi and ^{204}Tl sources have discrete energies, whereas the K_{β_1}, K_{β_2} x rays represent weighted electronic transitions and are less accurately known, thus only the $K_{\alpha_1}, K_{\alpha_2}$ x rays were used as reference energies in the measurement. The energies of these lines in mercury and lead are as follows:[1]

	Hg	Pb
K_{α_1} –	70.82 keV	74.97
K_{α_2} –	68.89	72.80

The pulses of interest from the Ge(Li) spectrometer represented a very narrow band out of the total available from the detector, and thus a linear relation was assumed in the calibration calculation. Deviations from non-linearity were determined by a least-squares calculation. Since the Ge(Li) spectrometer gave good resolution in the range of the Hg-Pb K x rays, the positions of the x-ray peaks were very accurately known, and thus the calibration calculations were greatly simplified in comparison to those on the NaI(Tl) detector. In addition, since the variation in resolution

of the Ge(Li) spectrometer was negligible over the energy range of the Ge(Li) spectrum (65-86 keV), the x-ray lines all had the same values of FWHM (approximately 1.12 keV with biased amplifier in system), and thus these lines were weighted equally in the calculations. The results of this analysis gave:

$$E_{GeLi} = .328\,X_{GeLi} + 64.94 \pm 0.02$$

where E_{GeLi} is the energy in keV corresponding to channel X_{GeLi}. The standard deviation ($\pm$ 0.02) is small, an indication of the overall linearity of the system including detector, pre and main amplifier, and biased amplifier.

Although the Ge(Li) spectrometer calibration was based on the x-ray lines appearing in the lower half of the spectrum, this was sufficient since only the K_α x-ray peaks were used in the analysis of the coincidence data. As a check on the calibration, the energies of the Hg K_{β_1} and Hg K_{β_2} x rays were compared to the values predicted by the calibration relation, and the results obtained were in agreement with the reported values to within an experimental accuracy of one standard deviation.

REFERENCES - DETECTOR CALIBRATIONS

1. J. A. Bearden and A. F. Burr, in Handbook of Chemistry and Physics (CRC Press Inc., Cleveland, Ohio), 54th edition, 1973-1974, pp. E181-E192.

CALIBRATION OF NaI(Tl) DETECTOR

Fig.1

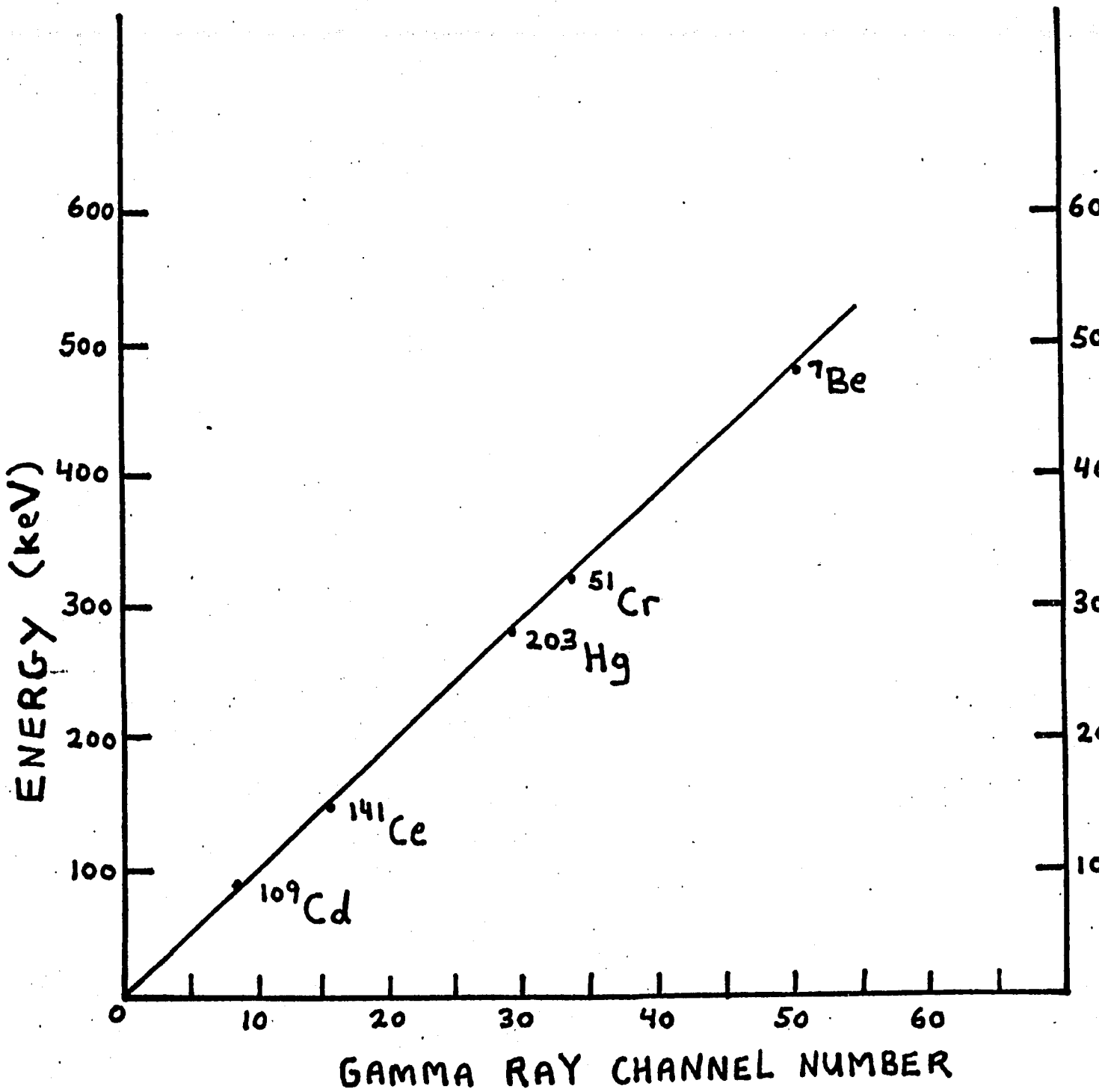

SOURCES AND ENERGIES USED FOR CRYSTAL CALIBRATION

ISOTOPE	ENERGY (keV)
^{109}Cd	87.7
^{141}Ce	145.4
^{203}Hg	279.1
^{51}Cr	319.8
^{7}Be	477.4

TABLE I

MEAN CHANNELS X_o AND WIDTHS $\Delta E_{\frac{1}{2}}$ AT HALF-MAXIMUM OF PHOTOPEAKS, AND RELATIVE ERRORS δ_i[(a)], IN CHANNEL UNITS

ISOTOPE	X_o	$\Delta E_{\frac{1}{2}}$	δ_i
^{109}Cd	8.66	1.06	0.45
^{141}Ce	15.86	1.75	0.74
^{203}Hg	29.60	3.08	1.31
^{51}Cr	33.68	3.44	1.46
^{7}Be	50.44	4.66	1.98

TABLE II

(a) δ_i are the relative errors in the values of X_o — see text for discussion

IX. ANALYSIS AND CONCLUSIONS

In order to compare the theoretical spectra to the experimental data, the theoretical differential spectra were multiplied by the response matrix of the Na(ITl) detector. The resulting pulse-height spectra were then normalized to the intensity of the experimental spectrum.

Let T represent the theoretical differential IB spectra for K-capture, and T_j represent the intensity per second in channel j. The T spectra are included in the discussion on theory; various T spectra corresponding to different endpoint energies are included in Tables II and III of that section. Let B represent the theoretically predicted pulse-height spectra, and B_i the IB intensity per second in channel i. Then B is related to T by the following expression.

$$B_i = \left(\sum P_{ji} T_j\right) \epsilon_{GeLi}^{Hg K\alpha} \epsilon_{coin} \omega_K I_{HgK} \left(\frac{\alpha_{K\alpha}}{\alpha_K}\right) (\Delta T) C$$

where ΔT is the experimental running time in seconds, and C represents the corrections for transmission through various absorbers. Now if we define E_i to be the intensity of the (measured) experimental spectrum in channel i, then the ratio of the total intensities of the measured and theoretically predicted spectra is

$$\frac{\sum E_i}{\sum B_i} .$$

These ratios were used to multiply the various predicted pulse height spectra in order to normalize them to the experi-

mental spectrum. The resulting spectra were then compared to the fifteen data points of the experimental spectrum by a χ^2 analysis. In this way, the best fitting theoretical spectrum was determined. The χ^2 were calculated for fourteen degrees of freedom, where

$$\chi^2 = \sum_i \left(\frac{E_i - P_i}{\sigma_i} \right)^2$$

Here P_i is the number of counts in channel i of the normalized pulse-height spectra, and σ_i is the standard deviation in channel i of the experimental data. The P_i and resulting χ^2 values for each spectra are included in Table I, where the spectra are arranged in vertical columns according to their end-point energies. In Figure 1 we plot the various χ^2 values obtained for the different values of k_m, the end-point energies of the spectra.

On the basis of the calculated values of χ^2, it is clear that χ^2 passes through a minimum in the vicinity of 300 keV. In order to determine the theoretical spectrum which best fits the experimental data, it was necessary to find this minimum value. By fitting the χ^2 values to a second degree polynomial using a least-squares curve fitting routine, it was possible to calculate the coefficients of the polynomial expansion, and consequently the end-point energy for the best-fitting theoretical spectrum. This method is not as sensitive a probe of the minimum energy as testing the variation in χ^2 for arbitrarily small changes in the energy in the region of the minimum. However, from an estimate of the quality of fit one can determine the error to be expected

in the determination of the position of the minimum value of χ^2. This error proved to be considerably smaller than other contributions to the error in end-point energy. The uncertainty in energy determination resulting from the calibration procedure was approximately $\pm$ 13.0 keV (two standard deviations), whereas the present procedure results in an error of approximately $\pm$ 1.9 keV in the location of the minimum.

The fitting procedure gives

$$\chi^2(E) = .005733E^2 - 3.520E + 553.08$$

and $\chi^2_{Min} = 12.81$ at $E_{Min} = 307.0 \pm 14$ keV.

A plot of this relation for $\chi^2(E)$ is included in Figure 1. It can be seen that in the region of the minimum, the parabolic shape gives a satisfactory fit to the data points.

As a check of this procedure, the theoretical spectrum corresponding to an end-point energy of E=307.0 keV was determined, and converted into a pulse height spectrum. This spectrum was compared to the experimental spectrum, and gave a χ^2 of 12.79, which was in excellent agreement with the value of 12.81 obtained from the above equation. The IB pulse height distribution corresponding to this value is shown with the experimental data points in Figure 5. The normalization condition resulted in a ratio of 4.31 for the theoretical to experimental intensity.

Since IB photons with energies corresponding to channel 10 (98 keV) contribute pulses to channel 11 of the IB pulse height distribution as a result of the broadening of the photo-

peak, the integration of the IB spectrum began at channel 10. Thus the "best fitting" theoretical spectrum gave a total intensity of 9.36×10^{-5} photons per K-capture event per second, over the energy range 98--307 keV, as compared to the experimental value of $(2.17 \pm 0.26) \times 10^{-5}$. The experimental error was obtained from the root-mean-square errors of the various terms used in the normalization procedure. This included a 7% error in the measured spectrum, which was primarily from counting statistics; a 5% error in the source intensity; a 6% error in the efficiency of the Ge(Li) spectrometer; a 4% error in the response matrix which was primarily due to the error in the NaI(Tl) total detector efficiency and the experimentally determined peak-to-total ratios; and finally a 3% error in the system coincidence efficiency. The total experimental error amounted to about 12%.

Additional spectra are included to show the behavior of the pulse height spectra for various end-point energies (figures 3,4). The broken curves represent the spectra which were obtained from using only the photopeak elements of the response maxtrix. It can be seen that the experimental geometry has a significant influence at the lower range of the spectra.

The procedure described above was also used to compare the experimental data to a Coulomb-free treatment of the Zon and Rapoport theory, obtained by setting $Z=0$ in the expression for the spectral distribution of the IB photons.

Table II contains the information analogous to Table I, where now the pulse-height spectra are obtained from the Cou-

lomb-free version of the theory. This theory predicts a lower end-point energy for the IB spectrum, and thus a lower energy range is used. The χ^2 values from this table and the curve from the fitting procedure are presented in Figure 2. This curve has coefficients A=0.0118339, B=6.4464, and C=9.3249, with a minimum χ^2 of 9.325 at an energy of 272.4 keV. The theoretical spectrum corresponding to this value was calculated and compared to the experimental spectrum yielding a χ^2 of 9.496, which was in good agreement with the curve's value. From the normalization procedure, the ratio of the theoretical to experimental intensity was 0.749. The intensity of IB for the best-fitting theoretical spectrum over the energy range 98.0--272.4 keV was 1.62×10^{-5} photons per K-capture per second, while the intensity of the experimental spectrum determined from the normalization procedure was $2.16 \pm 0.25 \times 10^{-5}$. The "best fitting" spectrum is plotted in Figure 6. Using the end-point energy of this spectrum, and taking into account the various experimental errors, a transition energy of 357.4 ± 14 keV is obtained. For sake of comparison, the best-fitting spectra corresponding to the two treatments of the theory are re-plotted in Figure 7.

The χ^2 value obtained for the Coulomb-free theory (9.496) is somewhat lower than the value obtained from the full theory (12.79). For fourteen degrees of freedom ($\nu=14$), the χ^2 at the $\alpha=.05$ level of significance is $\chi^2_{.95} = 23.685$. Thus we conclude that the fits of the data for both spectra are good. In addition, since $\chi^2_{.05} = 6.571$, it follows

that the value 9.494 is not too good as to be considered unbelievable. An examination of Figure 7 shows that the Coulomb-free spectrum lies closer to the experimental data points than the full theoretical spectrum over most of the energy range. Thus the lower χ^2 value obtained with the Coulomb-free spectrum is not due to atypical point(s) but to a better overall agreement of the shape of this spectrum with the experimental data.

The two treatments of the theory predict significant differences in K capture transition energy. In the full treatment of the Zon and Rapoport theory, a transition energy of 392 ± 14 keV is obtained. This value is in agreement with the values 376 ± 20, 393 ± 10, and 385 ± 20 obtained by Jung and Pool[1], Biavati, Nassiff, and Wu[2], and Lancman and Bond[3], respectively. In these measurements the Martin and Glauber theoretical spectrum for allowed transitions with the relativistic correction factor R_{IS} taken to be constant was used to obtain the end-point energies. Thus the apparent agreement of these results might be due to the similarity of technique used.

In the analysis of the Coulomb-free spectra, the value 357.4 ± 14 keV was obtained, which is in satisfactory agreement with value 344 ± 8 keV obtained from the mass table of Wapstra and Gove.[4]

The two versions of the theory disagree sharply on the magnitude of the effect--the intensity of the spectrum for the full Zon theory is almost six times the intensity of the spectrum for the Coulomb-free theory. This is surprising, since the

effect of the charge on the nucleus should add corrections proportional to αZ. Part of the reason for this discrepancy is due to the fact that the two theories yield different end-point energies, and thus different spectral intensities. However, although intensities of the Coulomb-free theoretical spectra show a marked dependence on end-point energy, (see Figure 2 in section on "Theory") the differences in intensities in the spectra with k_m in the range 250-300 keV are not enough to account for this discrepancy. In addition, as can be seen from Figure 1 of that section, the intensities of the spectra based on the full Zon theory show very little change with changes in k_m.

In order to have better confidence in the results of these comparisons, the values of $R_{1S}^{(1)}$ and $\tilde{R}_{1S}^{(2)}$ calculated by Zon (see Table I - "Theory"), which were used to determine W_{1S}/W_K, have been checked by Professor Robert Intemann by computer calculations.[5] He obtains excellent agreement with Zon's values.

It is possible that the lack of satisfactory agreement between the intensities of the experimental and theoreitcal spectra (especially for the full theory) might be affected by the presence of detour transitions,[6,7,8] which is an important consideration in forbidden decays. These are transitions through virtual intermediate excited nuclear states, and could compete with a direct transition which is highly forbidden. Such a transition could occur in EC decay of ^{204}Tl, e.g., through an excited 2^+ level in ^{204}Hg. The detour transition

could be represented by the following diagram,

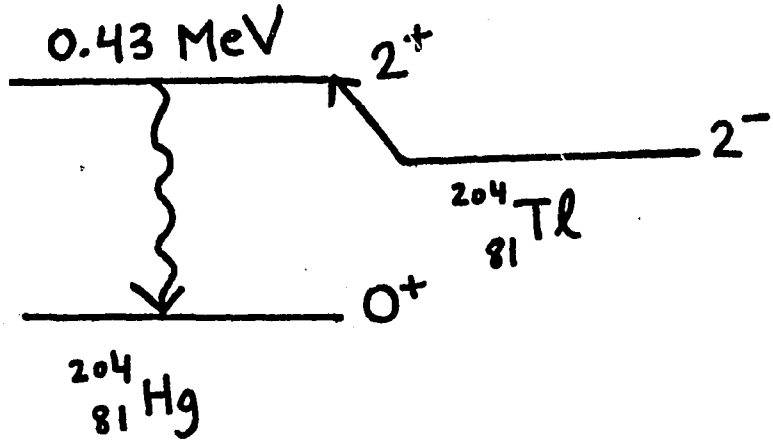

where the ^{204}Tl decay proceeds first to the intermediate 2^+ excited nuclear state, via a transition which may be expected to be faster than the direct transition to the 0^+ ground state, and then decays by the emission of E2 gamma radiation to the ground state. Transitions through intermediate 1^- states located at a higher energy could also contribute. These would constitute a cascade of an allowed EC transition followed by an E1 transition. The gamma rays in detour transitions have a continuous spectrum since energy is not conserved in the intermediate state, and thus contribute to the IB spectrum.

Since the detour transition leads to the same final state as the direct transition, there will be interference between the two branches, and thus the detour transition can be observed by the distortion of the IB spectrum produced by the direct transition alone. Rose[9] has shown that in cases where the excited daughter level is close to the parent level, the virtual transition is expected to be greatly enhanced in comparison to the direct transition for gamma ray energies approaching

the end-point energy of the IB spectrum. Thus under these circumstances one might expect a high energy distortion of the bremsstrahlung spectrum from the form to be expected when the nuclear electron capture gamma transition is not taken into account. No such distortion has been observed in the present spectrum. Also, the effect of detour transitions on the IB accompanying beta decay has been considered,[10] and it has been predicted to increase the intensity of the Coulomb-corrected spectra by an average of 20%. It is unlikely that these corrections would be substantially different in the case of electron capture. Thus it is doubtful that detour transitions could explain the observed discrepancies between theory and experiment in the present measurement.

The experimental intensity obtained by Lancman and Bond in the energy range 103 to 300 keV is $(3.2 \pm .5) \times 10^{-5}$ IB photons per K capture. The higher value than the one obtained in the present work is due to the fact that in the experiment of Lancman and Bond the two effects that contribute to the bremsstrahlung spectrum, K-capture and autoionization, could not be resolved.

It is also of interest to compare the shapes of the spectra. As in the case of beta ray spectra, a shape factor S can be introduced into the simple theory to determine the degree of deviation of various spectra from this theory. By comparing the Morrison and Schiff expression to the experimental and theoretical spectra, the shape factors for these spectra can be determined. Thus we take:

$$\frac{W_{1s}\,dk}{W_k} = \frac{\alpha}{\pi} k \left(1 - \frac{k}{k_m}\right)^2 S\,dk$$

The shape factor depends in general on k and k_m and a combination of nuclear matrix elements. For a unique first-forbidden decay, only a single matrix element is involved, which is cancelled in the ratio of the radiative to non-radiative capture probability. Thus only an energy dependent shape factor remains.

Using the above expressions and the theoretical expression of Zon and Rapoport for a unique first-forbidden decay, the shape factors corresponding to the full and Coulomb-free versions of the theory were determined. In the latter case this determines the effect of the forbidden character of the decay on the simple theory, while in the former case it also includes the effect of the nuclear charge on the simple theory. For the full theory this becomes:

$$S_{FULL} = \left\{ \left(1 - \frac{k}{k_m}\right)^2 R^{(1)}_{1s}(k) + \left(\frac{k}{k_m}\right)^2 \tilde{R}^{(2)}_{1s}(k) \right\}$$

whereas the Coulomb-free theory gives

$$S_{C\text{-}F} = \left\{ \left(1 - \frac{k}{k_m}\right)^2 + \left(\frac{k}{k_m}\right)^2 \right\} .$$

Both of these expressions are plotted in Figure 8. The

end-point energies used were the values obtained from the least-squares fitting procedure. These are exact shape factors, according to definition, without normalization to an arbitrary point.

In order to determine the experimental shape factors, the Morrison and Schiff spectra for the two end-point energies were determined. These spectra were multiplied by the response matrix, and normalized to the experimental running time. The shape factors were then obtained by comparing the resulting spectra to the experimental spectrum. Because of the large errors incurred in a channel by channel analysis of these factors, they were calculated for a few values of the spectrum, where each value represents an average over several channels of the spectrum. These points are shown in Figure 8. The values for the spectrum with k_m=307 keV have been shifted to the right of the values for the spectrum with k_m=287.4 keV, in order to distinguish the two sets of values. It is seen that the values at the end of the spectra contain large errors, which is to be expected due to the large relative errors in the experimental spectrum in this region.

The plot shows better agreement between the shapes of the experimental and Coulomb-free spectra, corresponding to a k_m = 287.4 keV, than between the shapes of the experimental and full Zon theory, corresponding to a k_m = 307 keV. The former shape factors are fairly flat for energies up to about 175 keV, and then begin to bend upward for higher energies. For k_m = 307 keV, the experimental shape factor is fairly flat until about 200 keV, where it begins to bend downward,

whereas the theoretical shape factor is steadily decreasing over the whole energy range. This graph shows again that the high intensity predicted by the full Zon and Rapoport theory is too high. The curves also show that the shape factor for the Coulomb-free theory is essentially an allowed shape factor in the plotted energy range, but is lower in magnitude than the allowed shape factor. The theoretical shape factors tend to converge on the allowed shape factors at energies approaching the end-points of the spectra. The experimental shape factors diverge at the high energy sides of the spectra. This is partly due to the fact that they were determined for different values of k_{max}. The extent of this disagreement is uncertain due to the large error bars in the shape factors at the ends of the spectra.

Assuming the Morrison and Schiff spectrum with k_m = 307 keV, it is clear from the diagram that the end of this spectrum must be reduced in intensity in order to bring it into better agreement with the experimental spectrum, whereas the theoretical spectrum with k_m = 287.4 keV must be increased at its end to obtain better agreement with the experiment. The Morrison and Schiff theory thus predicts an end-point energy in the range 287.4 to 307 keV. This plot shows that the values of the experimental shape factors at the ends of the spectra are very sensitive to the values of k_m used.

It is of interest to compare these results to the shape factor predicted by the Martin and Glauber theory. This theory differs from Morrison and Schiff by the relativistic correc-

tion term R_{1S} , which is the same as the term $R_{1S}^{(1)}$ used by Zon and Rapoport. According to Martin and Glauber

$$\frac{W_{IB}(k)\,dk}{W_K} = \frac{\alpha}{\pi m^2} R_{1S} \frac{(k-k_m)^2}{k^2} k\,dk .$$

The shape factor R_{1S} decreases from 0.31 at 110 keV to 0.25 at 300 keV[12]. Therefore this theory predicts a lower intensity for the IB than the present experimental data, and a shape factor which is in best agreement with the experimental $k_m =$ 307 keV value.

The shape factor for the IB in the first-forbidden unique capture transition in ^{41}Ca was measured by B. Myslek, et al.[11] A comparison with their results is somewhat restricted, since they studied a nucleus of lower atomic number (Z = 20), and a different transition energy (Q_{EC}= 421.2 keV). They conclude that there is strong disagreement between the experimental shape factor and the Coulomb-free theory, which they refer to as the (k^2+q^2) approximation. This conclusion is based on differences between the experimental and theoretical shape factors for both the lower and upper halfs of their spectrum. In the lower half of their spectrum, they obtain two different experimental shape factors, corresponding to "close" and "distant" geometries. In the upper half of their spectrum, these experimental shape factors agree, and fit fairly well with the Glauber and Martin theory, but disagree with Zon's and the Coulomb-free theory. In addition, in the lower half of their spectrum, they cite errors in the experimental shape factors, but do not indicate the size of these

errors. Thus in this region of the spectrum, it is difficult to determine which theory gives the best agreement with the experimental data.

On the basis of the foregoing conclusions, it appears that a re-derivation of the Zon and Rapoport theory is in order, especially before it is used in a detailed analysis of the IB spectra for higher degrees of forbiddeness.

REFERENCES - ANALYSIS AND CONCLUSIONS

1. R. G. Jung and M. L. Pool, Bull. Am. Phys. Soc. 1, 172, (1956).

2. M. H. Biavati, S. J. Nassiff, and C. S. Wu, Phys. Rev. 125, 1364 (1962).

3. H. Lancman and A. Bond, Phys. Rev. C7, 2600 (1973).

4. A. H. Wapstra and N. G. Gove, Nucl. Data A9, 265 (1971).

5. We are grateful to Professor Robert Intemann of Temple University for providing us with these calculations.

6. C. Longmire, Phys. Rev. 75, 15 (1949).

7. J. Horowitz, J. Phys. Rad. 13, 429 (1952).

8. G. W. Ford and C. F. Martin, Nucl. Phys. A134, 457 (1969).

9. M. E. Rose, R. Perrin, and L. L. Foldy, Phys. Rev., 128, 1776 (1962).

10. R. Prasad Babu, K. Narasimha Murty, and V. A. Narasimha Murty, Phys. Rev. C13, 1267, (1976).

11. B. Myslek, Z. Sukjowski, and J. Zylicz, Nucl. Phys., A215, 79 (1973).

12. H. Lancman and A. Bond, Phys. Rev. C7, 2600 (1973).

TABLE I

COMPARISON OF EXPERIMENTAL AND THEORETICALLY PREDICTED PULSE HEIGHT SPECTRA

CH. NO.	EXP. DATA	THEORETICAL SPECTRA MAXIMUM PHOTON ENERGY (keV)					
		260	279	297	316	334	353
11.5	472	618	569	527	490	456.5	431
13.5	374	481	456	434	410	391.4	379.5
15.5	356	344	339	330	320.7	315	306
17.5	256	243	242	247	243.2	242.5	238.3
19.5	232	152.7	163.7	176	182.3	183	182
21.5	141	77.8	101	121	129.7	135.6	143.2
23.5	97	33.3	55	73	86.7	97.5	103.2
25.5	14	10	25.7	38	52.8	64.6	74
27.5	19	2.3	8	15.4	28	39.2	49
29.5	-27	.1	1.7	8.3	12.5	21.6	29
31.5	34	0	.1	2.5	5	10.3	16
33.5	-6	0	0	.5	1	3.6	7.8
35.5	-5	0	0	0	.1	1.0	2.8
37.5	-1	0	0	0	0	.1	0.6
39.5	6	0	0	0	0	0	0
$\chi^2 \rightarrow$		27.16	17.77	13.34	13.21	16.63	23.30

TABLE II

COMPARISON OF EXPERIMENTAL AND COULOMB-FREE PULSE HEIGHT SPECTRA

CH. NO.	EXP. DATA	THEORETICAL SPECTRA MAXIMUM PHOTON ENERGY (keV) 223	242	260	279	297	316
11.5	472	640.7	565	505.2	462	426.9	396.8
13.5	374	514.7	469.3	431.4	400	376.3	353.4
15.5	356	371.3	355.5	348	329.4	315.6	300.9
17.5	256	246.5	257.6	264.5	261.8	255.6	246.1
19.5	232	133.9	173.2	191.2	201	201.6	200.5
21.5	141	48	102.9	125.3	145.2	154.5	159.3
23.5	97	6.7	33.5	67.2	92.7	109.8	121.9
25.5	14	0.2	4.9	24.4	49.1	70.7	87.2
27.5	19	0	.2	3.9	17.8	36.5	55
29.5	-27	0	0	.2	2.9	12.8	28.8
31.5	34	0	0	0	.2	1.8	10.6
33.5	-6	0	0	0	0	0	1.5
35.5	-5	0	0	0	0	0	0
37.5	-1	0	0	0	0	0	0
39.5	6	0	0	0	0	0	0
$\chi^2 \rightarrow$		43.04	20.32	10.77	10.04	16.12	26.2

χ^2 VALUES OBTAINED FROM COMPARISON OF EXPERIMENTAL AND THEORETICAL SPECTRA FOR VARIOUS ENDPOINT ENERGIES

FIG 1

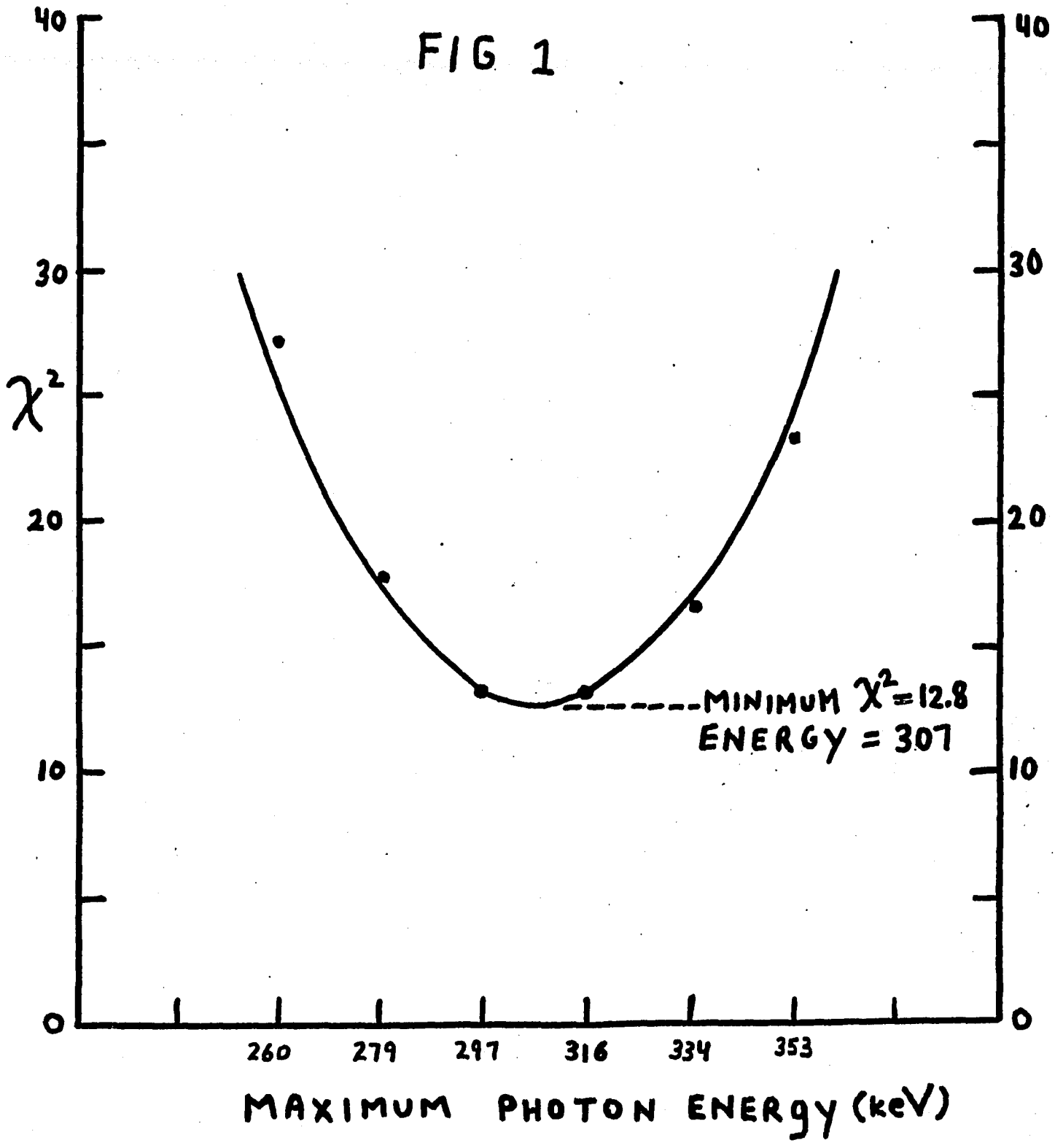

χ^2 VALUES FROM COMPARISON OF EXPERIMENTAL AND COULOMB-FREE THEORETICAL SPECTRA

FIG 2

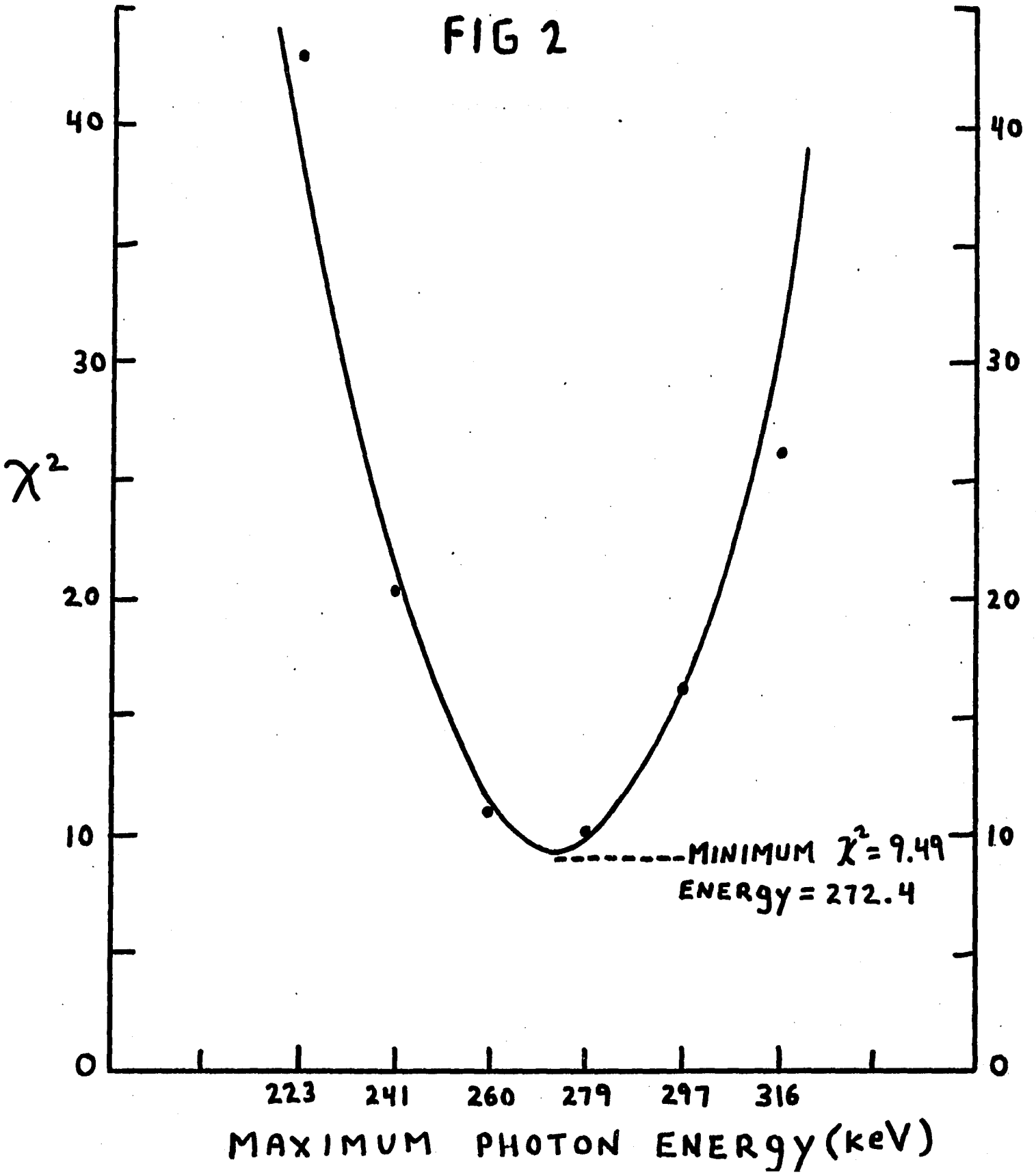

IB PULSE HEIGHT SPECTRUM OBTAINED FROM ZON AND RAPOPORT THEORETICAL SPECTRUM WITH $K_{max} = 278.6$ keV

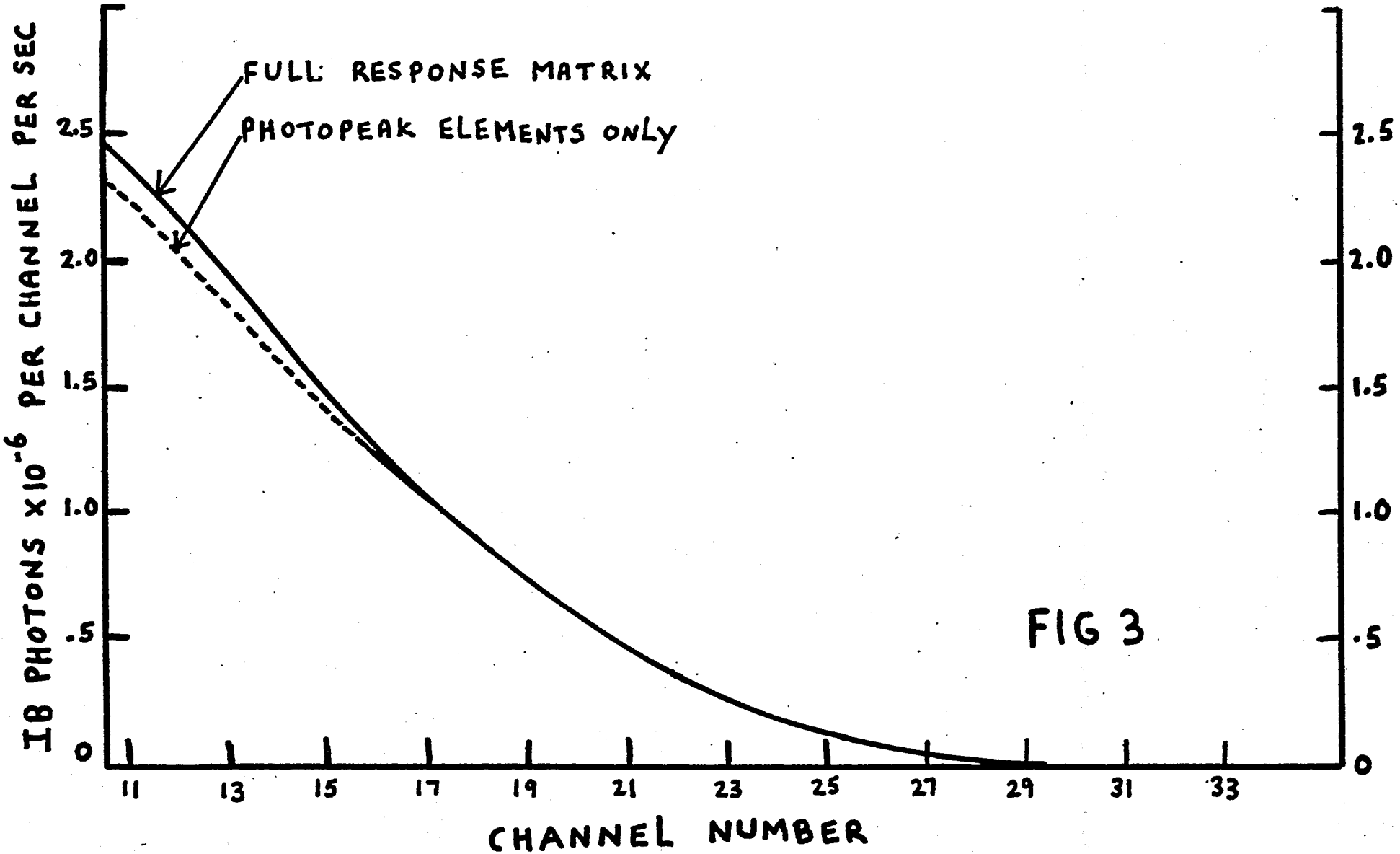

FIG 3

IB PULSE HEIGHT SPECTRUM OBTAINED FROM ZON AND RAPOPORT THEORETICAL SPECTRUM WITH $K_{MAX} = 334$ keV

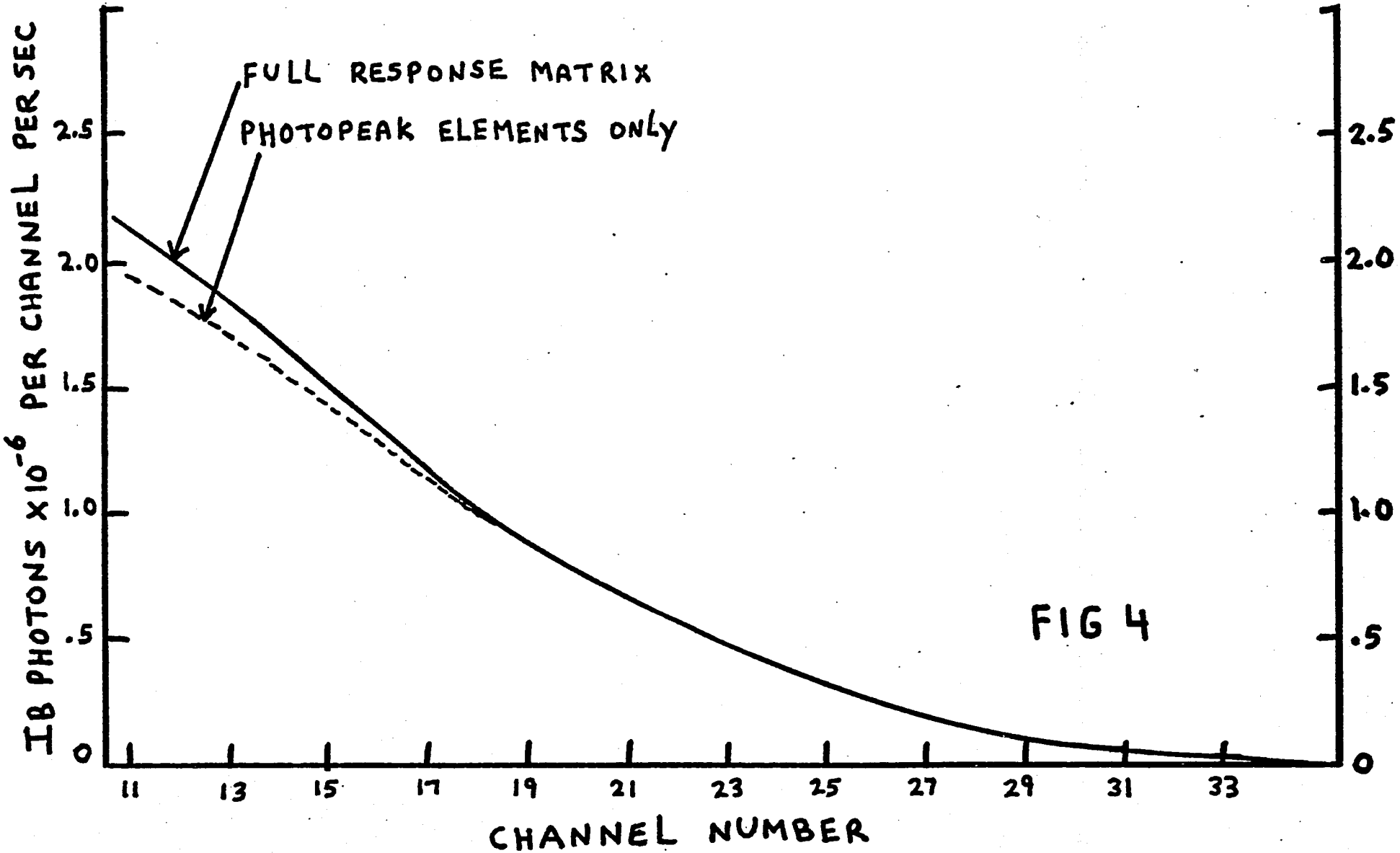

FIG 4

EXPERIMENTAL RESULTS AND "BEST FITTING" SPECTRUM OF ZON AND RAPOPORT

FIG 5

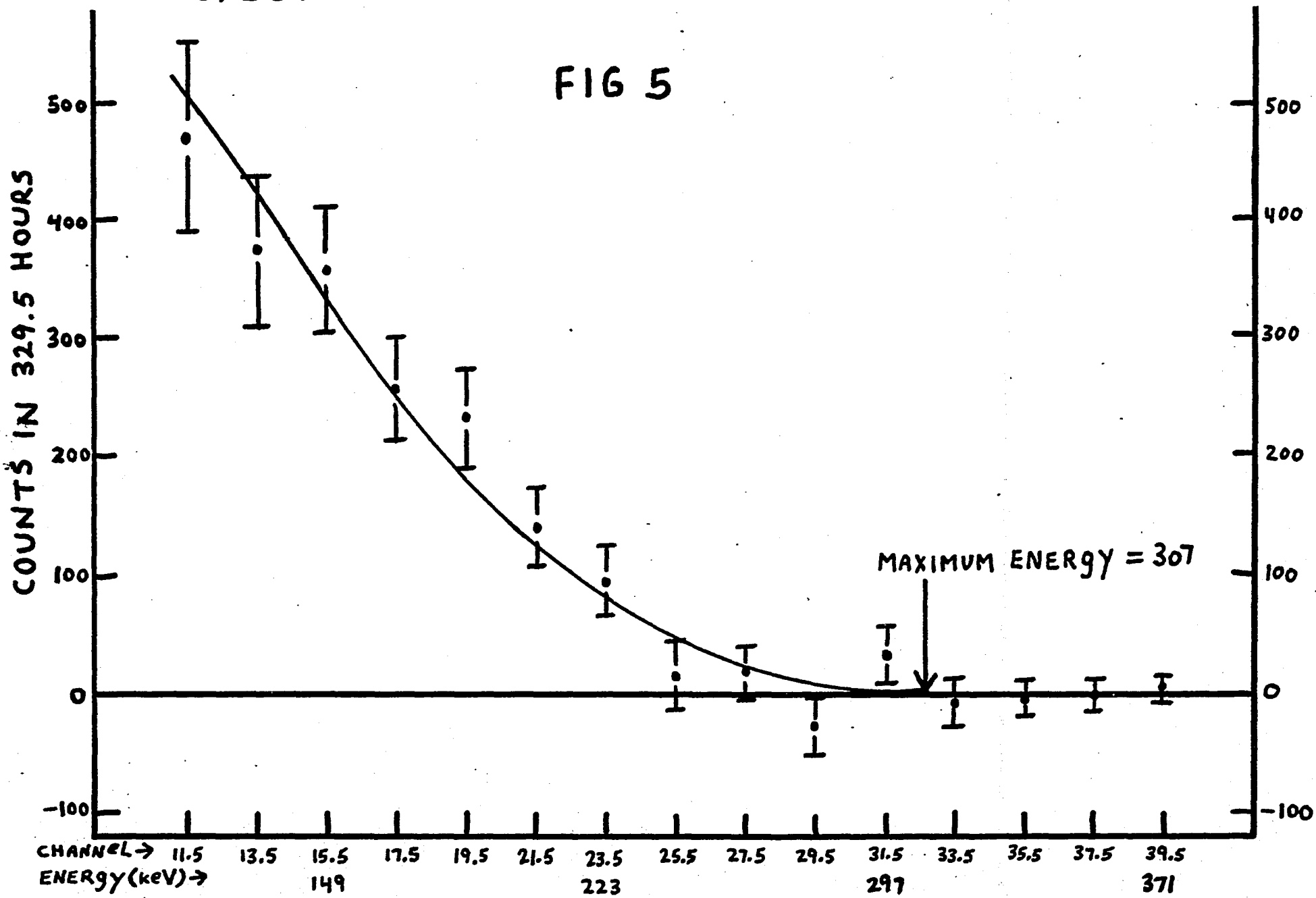

EXPERIMENTAL RESULTS AND "BEST FITTING" COULOMB-FREE SPECTRUM

FIG 6

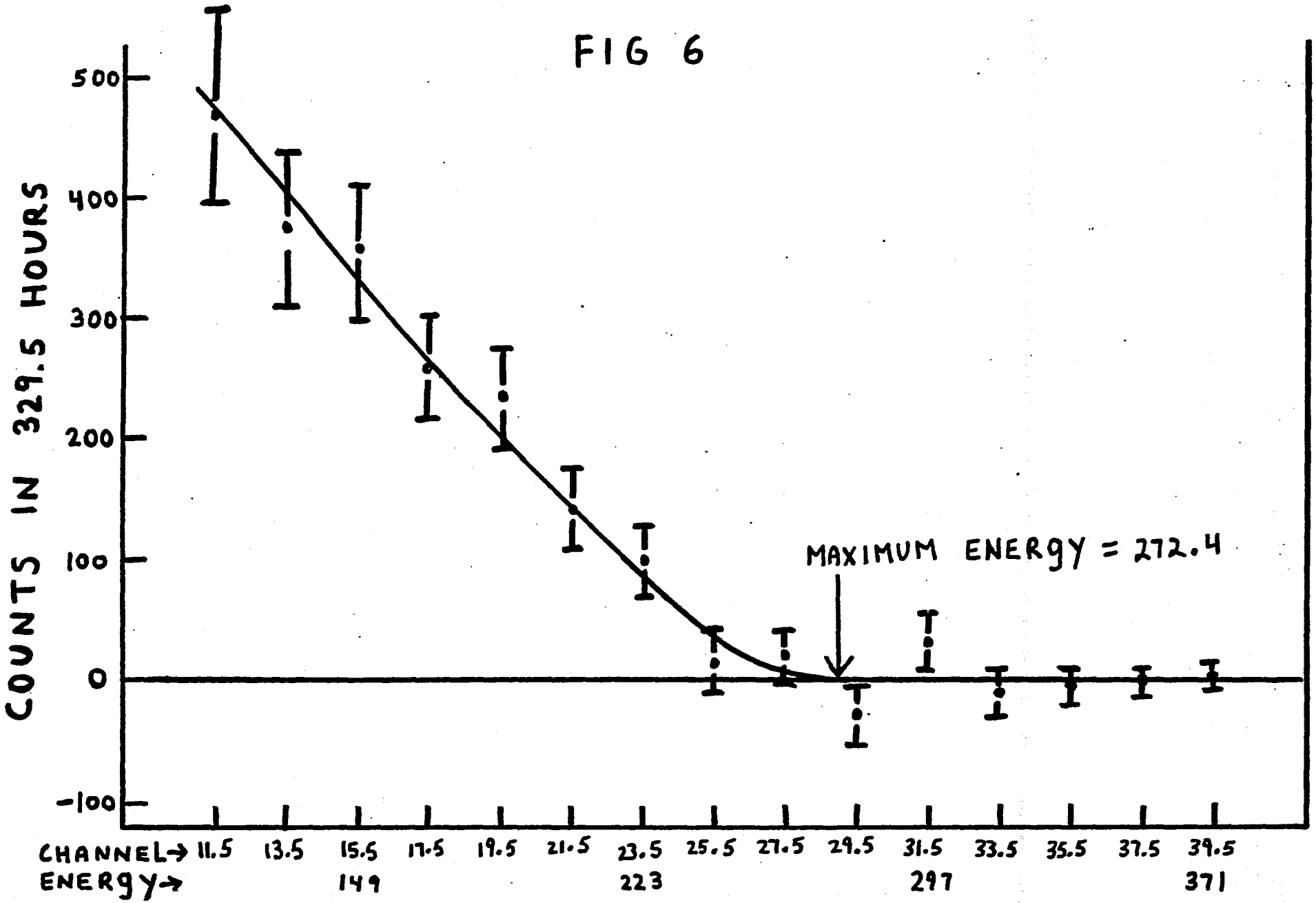

EXPERIMENTAL RESULTS AND "BEST FITTING" SPECTRA OF ZON AND RAPOPORT

FIG 7

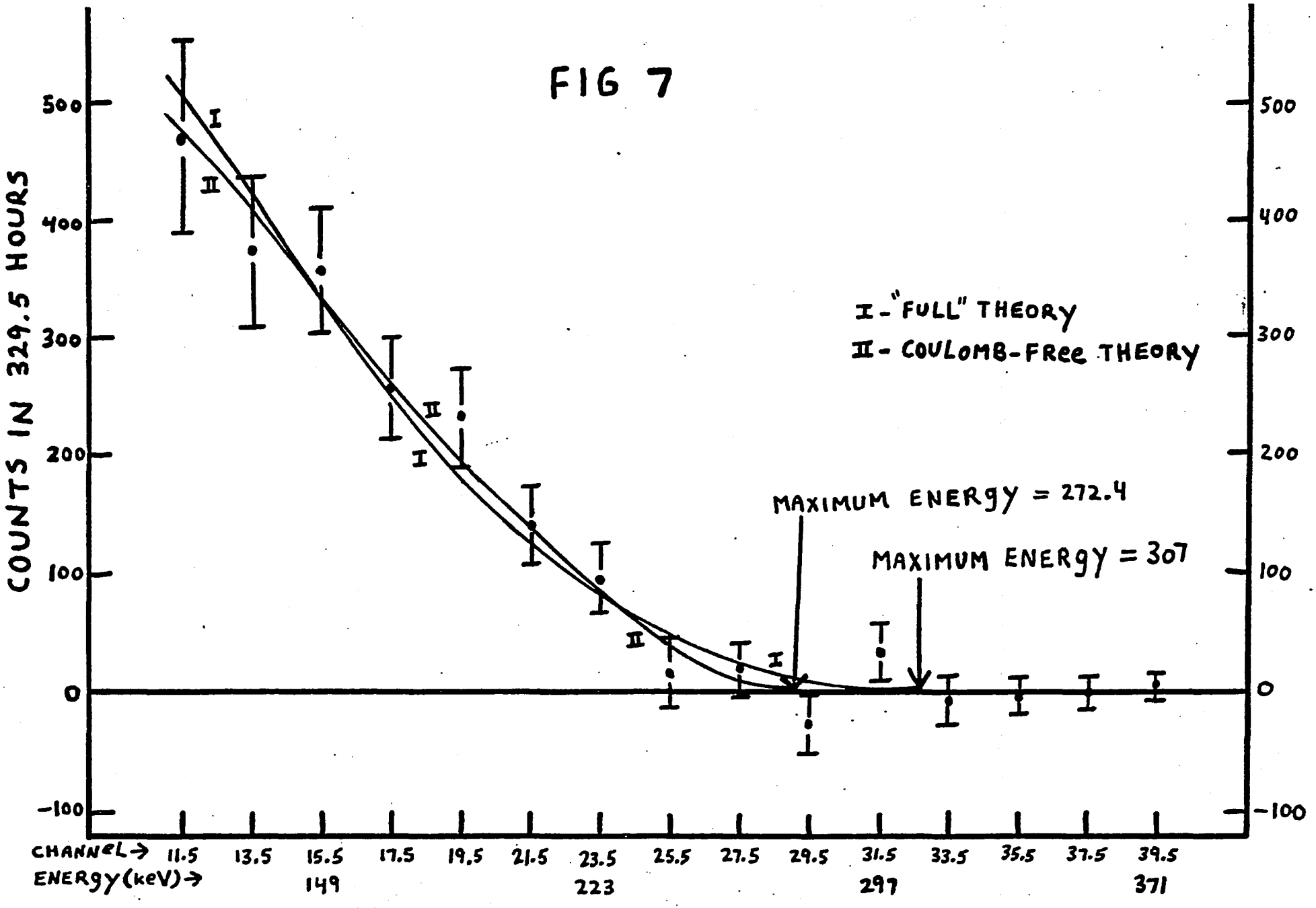

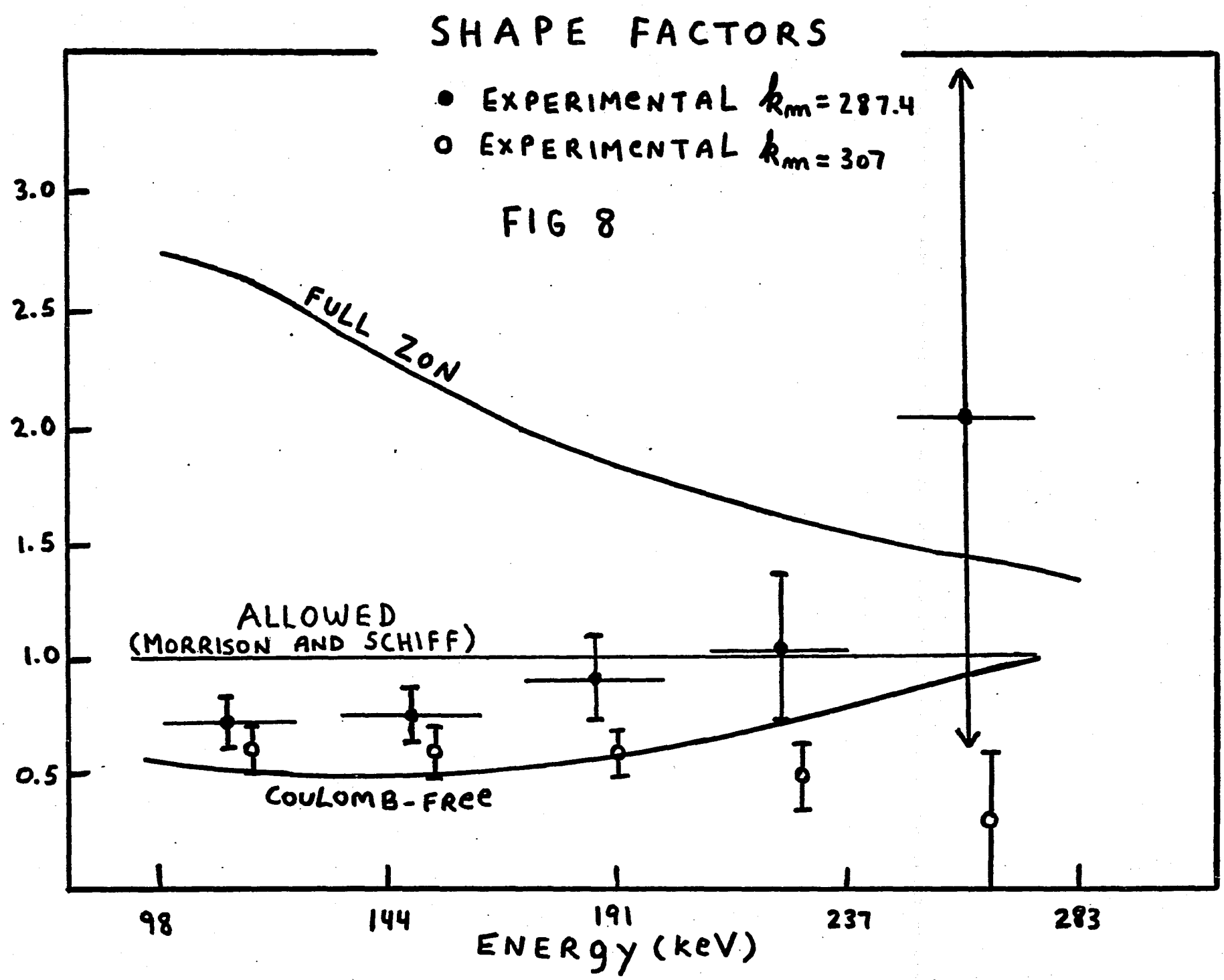
SHAPE FACTORS
● EXPERIMENTAL $k_m = 287.4$
○ EXPERIMENTAL $k_m = 307$
FIG 8
3.0
2.5
2.0
1.5
1.0
0.5
FULL ZON
ALLOWED
(MORRISON AND SCHIFF)
COULOMB-FREE
98
144
191
237
283
ENERGY (keV)